5-2016

Spin Flipper, Neutron Polarimetry, and Simulation, for the n3He Experiment

Christopher Bradshaw Hayes
University of Tennessee - Knoxville, chayes25@vols.utk.edu

To the Graduate Council:

I am submitting herewith a dissertation written by Christopher Bradshaw Hayes entitled "Spin Flipper, Neutron Polarimetry, and Simulation, for the n3He Experiment." I have examined the final electronic copy of this dissertation for form and content and recommend that it be accepted in partial fulfillment of the requirements for the degree of Doctor of Philosophy, with a major in Physics.

Geoffrey Greene, Major Professor

We have read this dissertation and recommend its acceptance:

Robert Gryzwacz, Thomas Papenbrock, Erik Iverson, Nadia Fomin

Accepted for the Council:
Dixie L. Thompson

Vice Provost and Dean of the Graduate School

(Original signatures are on file with official student records.)

Spin Flipper, Neutron Polarimetry, and Simulation, for the n3He Experiment

A Dissertation Presented for the

Doctor of Philosophy

Degree

The University of Tennessee, Knoxville

Christopher Bradshaw Hayes

May 2016

This document is dedicated to the memory of

Dr. David R. Hayes

July 14th, 1937 – April 10th, 2011.

Far better is it to dare mighty things, to win glorious triumphs, even though checkered by failure... than to rank with those poor spirits who neither enjoy nor suffer much, because they live in a gray twilight that knows not victory nor defeat.

Abstract

The n3He experiment constructed on FnPB [Fundamental neutron Physics Beamline-13] probes the PV [parity violating] nuclear force by measuring the statistical distribution of decay protons which result from the interaction of helium-3 nuclei with a beam of cold neutrons. Pulses of neutrons at 60 Hz are generated by the SNS [Spallation Neutron Source] from a 1 GeV proton beam colliding with a liquid Mercury target. Spalled neutrons are then focused into an intense cold neutron beam through the use of a liquid hydrogen moderator and a neutron guide making the beam an effective tool as a low energy probe of the nuclear force. An essential instrument for the experiment is the high efficiency spin flipper. This is a state-of-the-art device based on the theory of double cosine-theta coils, and specifically constructed to prevent interference with other instrumentation in the experiment. Details of spin flipper design and integration are reported along with polarimetry and polarimetry measurements of spin flipper efficiency and beam polarization. A target yield analysis is also performed which precludes the construction of a yield profile simulation.

Table of Contents

List of Tables

List of Figures

Chapter 1

Theoretical Background

A broad understanding of the n^{3}He experiment requires essential background material on the Hadronic Weak Interaction (HWI) and its specific application to the interaction of a neutron with a ^{3}He nucleus given by

$$\vec{n} + {}^3He = {}^3H + p + 764\,\mathrm{keV} \tag{1.1}$$

In addition, the theory of Nuclear Magnetic Resonance is essential to the understanding of neutron polarimetry and the operation of the spin flipper.

1.1 Theory of the Hadronic Weak Interaction

The theory of the nuclear force describes the interaction of neutrons and protons. It is a complicated non-central force having tensor components with a dependence on relative spin directions of the nucleons. The nuclear force is known to be highly attractive in the range of about 1 fm, but becomes repulsive for distances $\lesssim 0.7$ fm. Unlike gravitational and electromagnetic forces, it is also a short-range force having a reach of about 2 fm. This value can be easily estimated using the energy-time uncertainty principle where ΔE is the mass-energy of a pion.

At low energies the theory of the nuclear force is constructed using non-strange ($\Delta S = 0$) light virtual mesons π, ρ, and ω as mediators. Charged and neutral pions are spinless mesons but the ρ and ω are vector particles which can transmit the spin-dependence of the force. Emission amplitudes for these particles are well established for the nuclear force along with values of the strong coupling constants g_π, g_ρ, and g_ω.

A reaction like equation (1.1) is well characterized as a predominantly nuclear interaction which conserves parity. However, it also is possible to measure small deviations in the distribution of the decay particles which violate parity and are therefore attributed to the presence of the weak force acting between the nucleons. The effect is small and leads to a modified Hamiltonian

$$\mathscr{H}_{total} = \mathscr{H}_{pc} + \mathscr{H}_{pv} \tag{1.2}$$

This Hamiltonian characterizes the parity violating nuclear force and leads to a theory of the Hadronic Weak Interaction (HWI) [1, 2, 3] which takes into account both strong and weak couplings simultaneously.

The first theory of the HWI, called the *Meson Exchange Model*, was introduced by Desplanques, Donoghue, and Holstein [4] in 1980. In this model, the strong interaction between hadrons is still mediated by light virtual mesons π, ρ, and ω, but figure 1.1 shows how a weak component is introduced by requiring one vertex to couple weakly. This vertex can be viewed either as an emitter or an absorber of a weak boson. By conservation of charge the neutral Z^0 can only couple to a virtual ρ^0 or ω^0 meson while the $W^\pm$ couples to $\pi^\pm$ and $\rho^\pm$ mesons. A matrix element associated with a Feynman diagram such as figure 1.1 can be written

$$\langle MN|\mathscr{H}_{pv}|N\rangle \tag{1.3}$$

where M is short for 'meson'. Coupling both vertices with a purely charged or neutral weak current is not realistically possible here in view of the short range of the weak bosons ($< 10^{-3}$fm) compared with the average separation between individual nucleons—approximately three orders of magnitude larger. While the

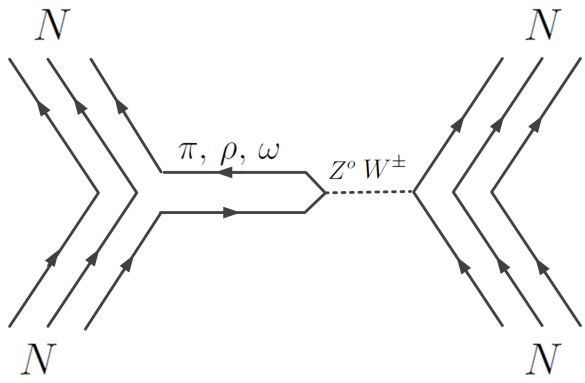

Figure 1.1: The range of $W^{\pm}$ and Z^0 bosons are too short for a direct interaction between nucleons.

weak component represented by this diagram is 10^{-7} times smaller than its strong counterpart, it is detectable experimentally as a result of the parity violation (PV) property of the weak force.

The meson exchange model (DDH model) works best for few nucleon systems. In general, observables are constructed from linear combinations of 6 unknown coupling constants $h_\pi^1, h_\rho^0, h_\rho^1, h_\rho^2, h_\omega^0, h_\omega^1$ which must be determined from experiment. The factors multiplying each of these couplings are numbers calculated from a Yukawa-like parity violating potential and are specific to a given observable for an interaction like (1.1). Values for these factors can be labelled $a_\pi^1, a_\rho^0, a_\rho^1, a_\rho^2, a_\omega^0, a_\omega^1$ so that the most general equation for an observable A will be given by

$$A = a_\pi^1 \cdot h_\pi^1 + a_\rho^0 \cdot h_\rho^0 + a_\rho^1 \cdot h_\rho^1 + a_\rho^2 \cdot h_\rho^2 + a_\omega^0 \cdot h_\omega^0 + a_\omega^1 \cdot h_\omega^1 \tag{1.4}$$

where the superscript indicates the isospin carried by the mediator.

The observable for the n^{3}He experiment is the PV asymmetry A_p of the outgoing proton. All terms in (1.4) contribute to the interaction but only the first term along with the two isospin-0 terms are significant. An approximation for A_p simplified from the general expression given in [3] is

$$A_p = -0.1821 \cdot h_\pi^1 - 0.1447 \cdot h_\rho^0 - 0.1269 \cdot h_\omega^0 \tag{1.5}$$

A precise value of the coupling constant h_π^1 will be determined by the recently completed NPDGamma experiment. The overall goal of n^{3}He is therefore an assessment of the zero isospin couplings h_ρ^0, and h_ω^0 of the DDH Model. Feynman diagrams associated with all couplings in (1.5) are indicated by figures 1.2 and 1.3 for reference.

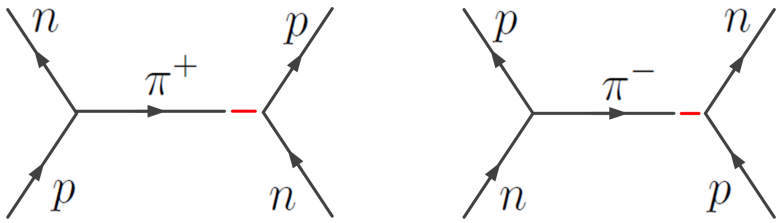

Figure 1.2: The weak vertex on the right side of each diagram is associated with the meson coupling constant h_π^1. The exchange of a π_o is not possible here since neutral spinless mesons do not contribute to parity violation.

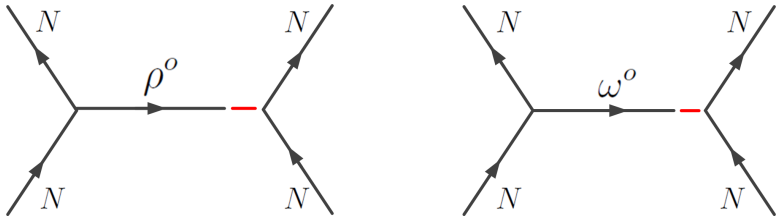

Figure 1.3: The ρ^o and ω^o are both vector particles. They carry no isospin and no charge so both nucleons N connected to each vertex are the same.

1.1.1 Determination of Asymmetries

The nuclear theory of the reaction (1.1) requires both PV and PC asymmetries associated with the statistical distribution of protons. While the primary goal of the n^{3}He experiment is a determination of the PV (up-down) proton asymmetry, the PC (left-right) asymmetry cannot be ignored since it is roughly the same order of magnitude 10^{-7} and can destroy the PV measurement without proper alignment of the experiment. Leading terms of the differential cross section inclusive of both asymmetries can be written

$$\frac{d\sigma}{d\Omega} = \frac{1}{4\pi}\left[1 + \varepsilon_{pc} + \varepsilon_{pv} + \cdots\right] \tag{1.6}$$

where the PV and PC asymmetries are given by

$$\varepsilon_{pv} = \alpha_{pv}\langle\boldsymbol{\sigma}\rangle \cdot \boldsymbol{k}_p \qquad\qquad \varepsilon_{pc} = \alpha_{pc}\langle\boldsymbol{\sigma}\rangle \cdot (\boldsymbol{k}_n \times \boldsymbol{k}_p) \tag{1.7}$$

and $(\alpha_{pv}, \alpha_{pc})$ are constants. The parity of each of these terms is easily demonstrated. For both terms the spin angular momentum $\langle\boldsymbol{\sigma}\rangle$ is a pseudovector which is even under a parity transformation. However, both linear momentum vectors are polar vectors which are odd under parity and this requires ε_{pv} to be parity odd while ε_{pc} is parity even.

There are several ways to ensure that the asymmetries remain experimentally separated. One possibility is to use longitudinally polarized neutrons. In this case, under proper alignment, the parity conserving contribution vanishes for all neutrons in the interaction region of the experiment. Unfortunately, variations in neutron beam intensity have indicated that it is not practical to use longitudinally polarized neutrons, so to avoid interference from the parity conserving term requires the neutron spin to be orthogonal to the neutron direction to a high degree of precision. This is possible from the observation that neutron spins will align adiabatically with the magnetic guide field provided for the experiment. The goal is therefore the alignment

of the guide field perpendicular to the beam direction. For motion in the z-direction one writes the neutron direction

$$\boldsymbol{k}_n = (\epsilon_x, \epsilon_y, 1)k_n \tag{1.8}$$

and then estimate tolerances for ϵ_x and ϵ_y which yield a value of the proton asymmetry to within the required accuracy.

Parity Violating Asymmetry: In terms of the cross-section formula (1.6) the value of A_p follows by choosing an appropriate coordinate system for which

$$\varepsilon_{pv} = A_p \cos\theta \tag{1.9}$$

Possible values for A_p may be determined from DDH table VII which gives best values and reasonable ranges for the coupling constants using Weinberg–Salaam model parameters. Values in the table are given as fractions of the strong coupling constant

Table 1.1: Best values and reasonable ranges from the DDH paper

Coupling Constant	Best Value	Reasonable Range
h^1_π	12	$0 \to 30$
h^0_ρ	-30	$-81 \to 30$
h^0_ω	-5	$-27 \to 15$

$g_\pi = 3.8 \times 10^{-8}$ and gives an estimate of the value of the proton asymmetry

$$A_p = 1.060 \times 10^{-7} \tag{1.10}$$

with maximum and minimum values from the reasonable range estimates

$$-4.449 \times 10^{-7} \leq A_p \leq 5.756 \times 10^{-7} \tag{1.11}$$

Parity Conserving Asymmetry: Production data for the PC asymmetry was taken in March and December 2015 by rotating the ion chamber 90 degrees in a clockwise manner looking upstream with respect to the beam. Aproximately 1000 data runs were taken (at 7 minutes per run) in both cases which required about 120 hours of run time. The PC asymmetry is different than the PV asymmetry and is a function of the neutron momentum $\boldsymbol{k}_n$. This means that the magnitude of the asymmetry will depend on the neutron energy. This is important for the n^{3}He experiment which uses a distribution of cold neutron energies.

1.2 Nuclear Spins and Kinematics

The absorption and emission of radiation by nuclides in the presence of a typically constant externally applied magnetic field is referred to as Nuclear Magnetic Resonance (NMR). In general, a nucleus has an intrinsic angular momentum $\boldsymbol{S}$ along with an associated nuclear magnetic moment $\boldsymbol{\mu}$ related to $\boldsymbol{S}$ by the simple relation

$$\boldsymbol{\mu} = \gamma \boldsymbol{S} \tag{1.12}$$

where γ is the gyromagnetic ratio. However, isotopes with even numbers of protons and neutrons will not respond to nuclear magnetic resonance since pairs of nucleons align in anti-parallel spin configurations leaving a total nuclear spin of zero.

For those nuclides with a non-zero spin, the energy of the nuclear magnetic moment in an external field $\boldsymbol{B}_o$ can be written

$$E = -\boldsymbol{\mu} \cdot \boldsymbol{B}_o \tag{1.13}$$

A given nucleus with quantum number S has $2S + 1$ possible energy states and a transition between these states can be accomplished with an appropriately chosen photon energy. The simplest example of NMR is for an isotope having a nuclear

spin $S = 1/2$. There are only two possible energy states with an energy difference quantized along the z-axis given by

$$\Delta E = \gamma \hbar B_o \tag{1.14}$$

Excitations from the ground state energy can be induced through interaction with an incoming resonant photon having a frequency ω_L equal to the Larmor frequency of the nuclide

$$\omega_L = \gamma B_o \tag{1.15}$$

Two examples of two-state NMR isotopes are ^{3}He and ^{3}H which also have similar spin properties since they are both composed of three spin-1/2 fermions—two of which are identical. The Pauli exclusion principle rules both nuclei by requiring the spins of the identical nucleons to align anti-parallel in a spin-0 configuration. The total nuclear spin will then be determined solely by the odd fermion which is $S = 1/2$ qualifying both nuclei as two-state NMR emitters and absobers.

The gyromagnetic ratio for ^{3}H is not important for the n^{3}He experiment but a fairly precise value for ^{3}He can be determined from [5] and a knowledge of the proton gyromagnetic ratio:

$$\gamma_{[He3]} = -2.038024 \times 10^8 \, \mathrm{s}^{-1}\mathrm{T}^{-1} \tag{1.16}$$

An intrinsic magnetic moment can also be calculated for a free neutron and a free proton which are both $S = 1/2$ fermions. Typically, these magnetic moments are given in terms of the nuclear magneton and the spin g-factor:

$$\mu = \mathrm{g}\mu_N \qquad \text{where} \qquad \mu_N = 5.05078353(11) \times 10^{-27} \, \mathrm{J/T} \tag{1.17}$$

Once again, the magnetic moment of the proton is not important for the n^{3}He experiment but a precise value for the neutron determined by Greene and Ramsey [6]

is

$$\mu_n = -1.91304211(88)\mu_N \tag{1.18}$$

A simple calculation then determines the neutron gyromagnetic ratio

$$\gamma_n = -1.83247165 \times 10^8\,\mathrm{s^{-1}T^{-1}} \tag{1.19}$$

1.2.1 Kinematics

The binding energy of the ^{3}He nucleus is smaller then the ^{3}H nucleus due to the mutual electromagnetic repulsion of its two protons. Using M_T for the mass of the triton, formulas for the binding energy of both nuclei are

$$E_b[T] = (M_p + 2M_n - M_T)c^2 \tag{1.20}$$

$$E_b[He3] = (M_n + 2M_p - M_{He3})c^2 \tag{1.21}$$

The energy liberated by the reaction in equation (1.1) is easily determined by calculating the difference in the two binding energies which is the same as the difference in mass-energy of the particles on both sides of the reaction equation

$$K = (M_{He3} + M_n - M_T - M_p)c^2 = 764\,\mathrm{keV} \tag{1.22}$$

This excess energy is kinetic energy shared by the outgoing triton and proton. The portion of the kinetic energy shared by each particle follows by simple consideration of energy and momentum conservation assuming the initial neutron and helium nucleus are at rest:

$$K_T = \frac{M_p K}{M_p + M_T} = 191.3\,\mathrm{keV} \qquad K_p = \frac{M_T K}{M_p + M_T} = 572.7\,\mathrm{keV} \tag{1.23}$$

Practically speaking, the energy and momentum of the outgoing proton is 3 times that of the triton.

Chapter 2

Overview of Experiment

This chapter contains information regarding the production of neutrons by the SNS and the configuration of the chopped beam used by the n^{3}He experiment. A discussion of the overall design of the experiment emphasizes individual components—mainly the spin flipper, the ion chamber, the collimator, and the guide field.

2.1 Neutrons provided by the SNS

The Spallation Neutron Source (SNS) is designed to provide high intensity 60 Hz pulses of neutrons. The source is a low duty factor proton beam at 1 GeV providing an average proton current of approximately 1 mA which collides with a liquid Mercury target. This translates into an incident proton power of about 1 MW.

Moderators: Each colliding proton can produce 20-30 neutrons having a range of energies up to the incident energy of a proton. Most of these neutrons are far too energetic to be used by FnPB and must be slowed by the presence of a moderator [7, 8]. Of the several moderators provided by the SNS, the source of FnPB cold neutrons is a cryogenic H_2 moderator at 20 K—capable of producing a well defined neutron flux emerging from its front face with a range of energies less than about 10 meV.

Neutron Guide: The emerging flux consists of 2×10^{11} neutrons per second travelling one meter to the entrance of a 14 m long neutron guide [9] with a rectangular cross section measuring 12 cm high by 10 cm wide. The guide is a rather complex structure having both straight and curved sections—all with various interior supermirror coatings. It resides inside a vacuum tube and transports individual neutron pulses through internal reflections on the supermirror walls. The high reflectivity of the supermirror qualifies the guide as lossless. Figure 2.1 shows the

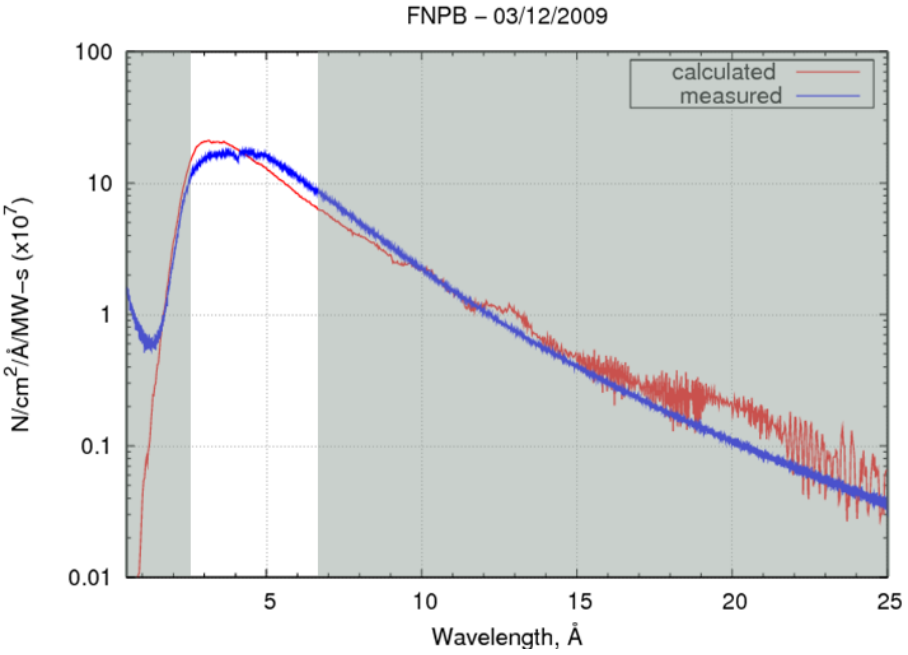

Figure 2.1: Plot showing measured and simulated neutron flux near the end of the neutron guide. Figure is courtesy of the NPDGamma collaboration

wavelength spectrum of the unchopped neutron beam emerging from the end of the guide. The shaded portions of the plot indicate those neutrons absorbed by two frame definition choppers placed along the guide. The main purpose of the choppers is to prevent frame overlap between two successive pulses of neutrons. The choppers rotate in opposite directions and only transmit wavelengths in the range 2.5–6.5 Å through pie-shaped openings. Absorption of the unwanted wavelengths is maximized with a layer of ^{10}B applied to the chopper surface facing the oncoming beam.

M1 Beam Monitor: A measure of the chopped neutron beam is available from the 'M1' beam monitor installed near the end of the guide. The M1 monitor is filled with ^{4}He and N_2 gases and a small partial pressure of ^{3}He which interacts with beam as in equation (1.1). The interaction generates an electrical current proportional to the beam intensity which can be amplified and viewed on the Data Acquistion (DAQ) electronics. The amount of ^{3}He in the monitor is deliberately chosen to be small for minimal attenuation of the beam. Details are available in [10].

Figure 2.2 shows the signal on the M1 monitor versus time for a few neutron pulses. Since the SNS is a pulsed source the intensity of neutrons in a pulse at time t is proportional to the neutron wavelength with the shortest wavelengths occuring at the front of each pulse. The complete M1 signal is recorded over the length of each

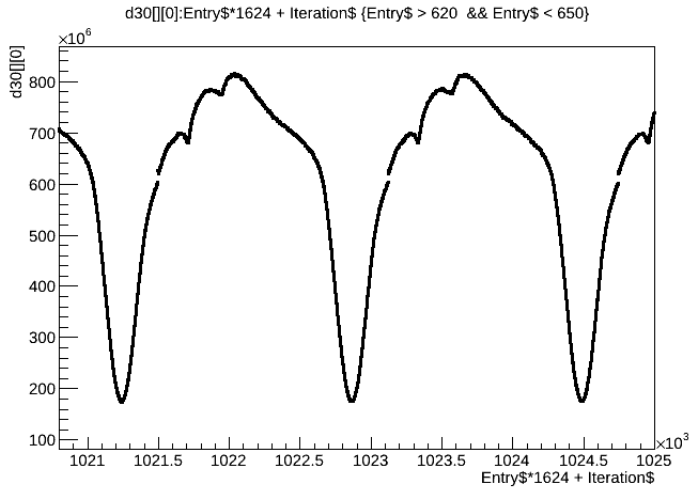

Figure 2.2: Neutron pulses measured by the M1 beam monitor and displayed by the DAQ electronics as a function of time.

data run produced by the experiment. Cuts on the M1 monitor are an essential part of data analysis to eliminate portions of data for any number of reasons including any pulses with undesirable characteristics, or data runs taken with no beam present. The M1 monitor also provides oversight of the SNS proton beam power since variability of proton beam power is directly proportional to the recorded neutron beam intensity.

Supermirror Polarizer: The neutron beam is polarized by a supermirror polarizer (SMP) [11] inserted just before the end of the neutron guide. The polarizer is 40 cm long and composed of 45 channels of glass panes coated with alternating layers of nickel and silicon. The device operates as a spin filter by transmitting one neutron polarization state through quasi-Bragg reflections from the Si, Ni multi-layer while absorbing those neutrons of the opposite spin state.

The filtering property of the polarizer is facilitated by a large magnetic field of 350 Gauss produced by an array of permanent dipole magnets arranged in close proximity to the glass panes. The field magnetizes the ferromagnetic nickel-coated layers introducing a spin-dependent term to its index of refraction

$$n = \sqrt{\frac{E - V_{[Ni]} \pm \boldsymbol{\mu} \cdot \boldsymbol{B}}{E}} \quad \text{where} \quad E = \frac{h^2}{2m\lambda^2} \tag{2.1}$$

while having no effect on the silicon which is nonmagnetic. This means that one neutron spin state will see a lattice of alternating index of refraction allowing it to reflect and continue towards the FnPB beamline while the opposite spin state will see a relatively homogenous index of refraction allowing for transmission and absorption into the glass substrate. Ultimately, the beam receives a polarization of about 93% with a small dependence on wavelength at the expense of a reduction in neutron flux by a factor of three. This includes the inevitable loss of a factor of two due to spin selection.

State Vector for the Neutron Beam: The spins of the neutrons travelling along the neutron guide from the moderator may be considered to be randomly polarized. If they are incident on an ideal supermirror polarizer, it will act as perfect filter—absorbing exactly one-half of the neutrons and transmitting the remaining half with polarization $P_n = \pm 1$. In this case the neutron beam is a pure ensemble meaning that every neutron in the beam can be described by the same state vector. For neutron

spins filtered in the +y-direction, the state vector is

$$|\psi\rangle_{beam} = |S_y+\rangle \tag{2.2}$$

Unfortunately, the limits of the supermirror polarizer require an accurate description of the neutron beam to be written in terms of a mixed ensemble [12]. Specifically, for a given wavelength, it is known that the fractional population of spins filtered by the polarizer in the +y direction is $P_n(\lambda)$ but the remaining fractional population is still randomly polarized and can be analyzed in any arbitrary direction. If this portion of the beam is analyzed along the x-direction then the neutron beam is correctly characterized by the density operator

$$\rho = P_n|S_y+\rangle\langle S_y+| \ + \ \frac{1-P_n}{2}|S_x+\rangle\langle S_x+| \ + \ \frac{1-P_n}{2}|S_x-\rangle\langle S_x-| \tag{2.3}$$

Expectation values for the spin angular momentum of the neutron beam in all three directions are then determined by

$$\langle S_x\rangle = Tr[\rho S_x] = 0 \qquad \langle S_y\rangle = Tr[\rho S_y] = \frac{\hbar}{2}P_n \qquad \langle S_z\rangle = Tr[\rho S_z] = 0 \tag{2.4}$$

At 95% beam polarization, treating the beam as a pure ensemble is a reasonable approximation; but it is important to clarify the true nature of the state vector for any instance where it might be relevant.

2.2 Instrumentation

The overall design of the n^{3}He experiment is illustrated in figure 2.3. Pulses of neutrons emerging from the supermirror polarizer are spin aligned transverse to the direction of motion. Individual pulses enter the spin flipper which is synchronized to the arrival of each pulse and becomes energized to flip the spins of alternating pulses with an efficiency approaching 100 percent. Neutrons emerging from the spin flipper

interact with ^{3}He in the ion chamber producing protons and tritons in accordance with (1.1). The value of A_p can be extracted from measurements of electrical currents induced in wire planes within the ion chamber.

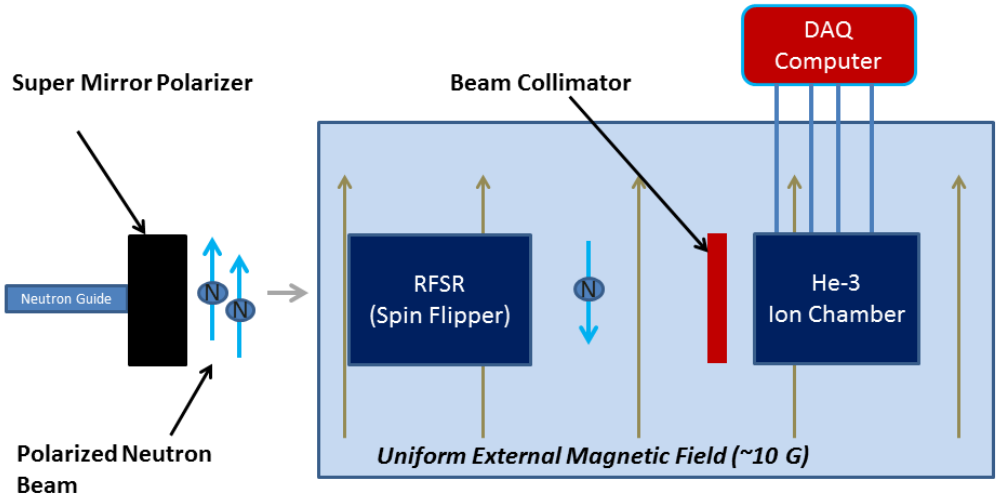

Figure 2.3: Overall design of the n^{3}He experiment. Complex data acquisition electronics attached to the ion chamber are not shown here.

The success of this measurment hinges on the successful elimination of false asymmetries to at least an order of magnitude less than δA_p which can be achieved through a precision alignment of the ion chamber with the transverse holding field. Even with precise alignment however the success of the experiment relies on high efficiency operation of the spin flipper and sound data acquisition electronics.

2.2.1 Spin Flipper

The spin flipper operates at radio frequency and is capable of flipping both longitudinal and transverse neutron spin states using the physics of Spin Magnetic Resonance (SMR). Pictures of the completed spin flipper are displayed in figure 2.4.

The interior of the device is composed of two semi-circular outer wire coils which fit snugly around a central inner wire coil. The wires in each coil fit precisely into complex groove patterns designed in accordance with the theory of double cosine theta coils [13], and serve the purpose of producing a uniform transverse magnetic field in the region inside the inner coil—with no external field. Each of the three coils is independently wound and then all three coils are connected in series with the inner cylinder in the middle. The series connection accommodates about 870 feet of 18 AWG solid aluminum wire. Aluminm wire is preferred over copper which is difficult to form around the coils and can also be activated by the neutron beam.

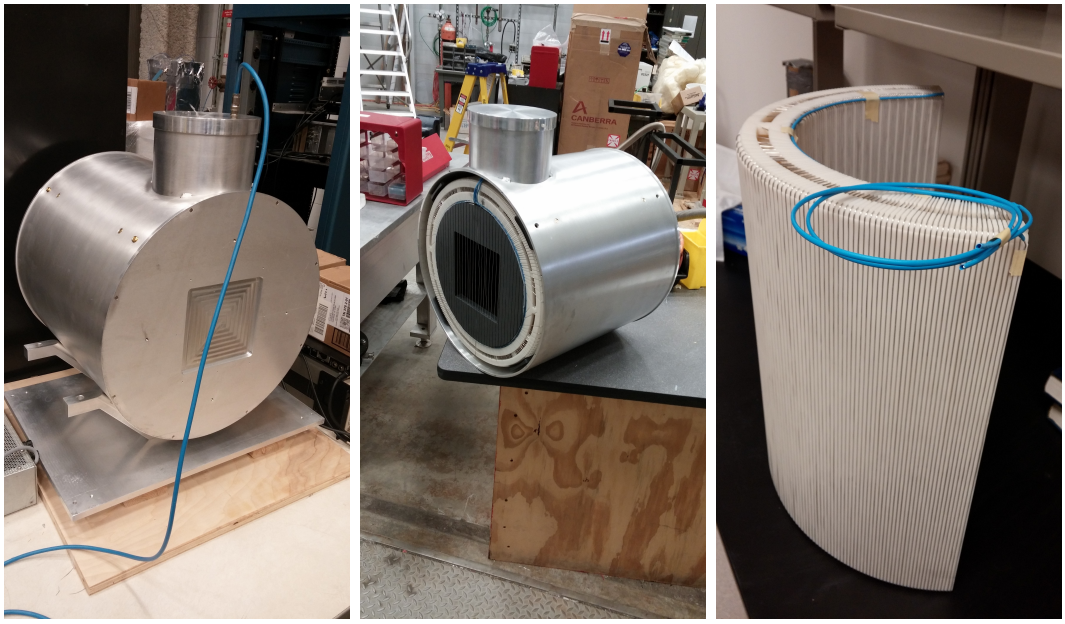

Figure 2.4: Pictures of the n^3He spin flipper. The inner cylinder is made from 12.5 inch PVC pipe and was machined by the UT machine shop. The outer return coils are ABS plastic and were extruded using an SLA (Stereolithographic) 3D print technology.

The coils are enclosed by a 1/4 inch thick cylindrical aluminum shell and two 1/4 inch thick end plates with square insets machined to 0.040 inches to provide thin windows for the neutron beam. The end plates are sealed to the cylinder with RTV Silicon so that the device can be filled with ^{4}He gas to prevent scattering of internal neutrons during use. The housing on top of the shell accommodates a parallel connection of two capacitors with a total capacitance of $C = 17.7\,\mathrm{nF}$—chosen to match the natural frequency of the circuit with the Larmor frequency of neutrons in the guide field. Both are Cornell Dubilier high voltage mica capacitors with individual capacitances of 15.0 nF and 2.7 nF. The neccessity for more than one capacitor arises from matters of cost and availability.

The space between the outer coils and the inner cylinder is filled with thin layers of neoprene and polyethylene sheet and the entire coil system is wrapped under pressure with heavy duty glass tape. The coil system is held in place inside the aluminum shell with four padded coil support bars evenly spaced inside the perimeter of the aluminum shell. Brass set screws are inserted from outside the aluminum shell and can be turned with a hex wrench to apply pressure on the bars and the coil system.

A primary requirement for the spin flipper is to avoid the possibility of any electromagnetic interference with DAQ electronics and the ion chamber. By design, the interior RF magnetic field produced by the coils is self-contained with an added layer of shielding provided by the thick aluminum shell. This is sufficient to ensure that field lines do not leak outside the device. However, electrical isolation of the spin flippers' 120 Hz power source can also be established by a few precautionary steps; for example, wrapping its aluminum mount with electrical tape before setting the spin flipper on the mount.

2.2.2 Four Jaw Collimator

A critical piece of instrumentation for the n^{3}He experiment is the four-jaw collimator designed by the author and built by the UT-physics machine shop. The device is

nothing more than two vertical and two horizontal doors which slide on rails and can

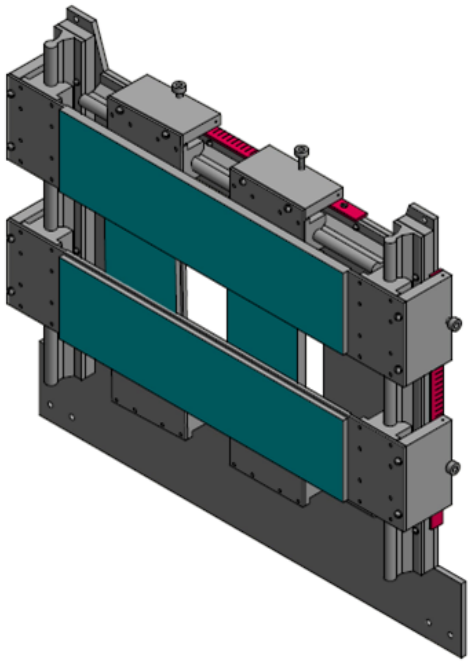

Figure 2.5: CAD drawing of the four-jaw collimator. Torquoise covering on the doors is ^{6}Li neutron shield. Red strips are straightedge rulers with 1 mm rule markings.

be set to any chosen position by tightening thumb screws. Each door is also covered with two layers of ^{6}Li along with a thin protruding Cadmium edge* which effectively absorbs 100% of the beam except in the rectangular space between the doors.

The position of the doors is determined by rules on the side and on the top of the device and can be set relative to the beam centroid to within about 0.1 mm. Settings on the doors were unchanged throughout the course of the experiment, except for polarimetry measurements which required closing the doors to a 3.5×3.5 cm square to absorb beam outside the radius of the analyzer cell. Following polarimetry the doors could then be reset to their original positions.

* A cadmium edge protrudes slightly from the inside of each door to define a 'sharp' door edge with respect to the neutron beam.

2.2.3 Ion chamber

The ion chamber [14] serves as the beam target, the detector, and the beam monitor during polarimetry measurements. A CAD drawing of the aluminum exterior is shown on the left in figure 2.6 and a picture of the interior frame stack is shown on the right. The frame stack is composed of Macor ceramic spacers designed to hold an array

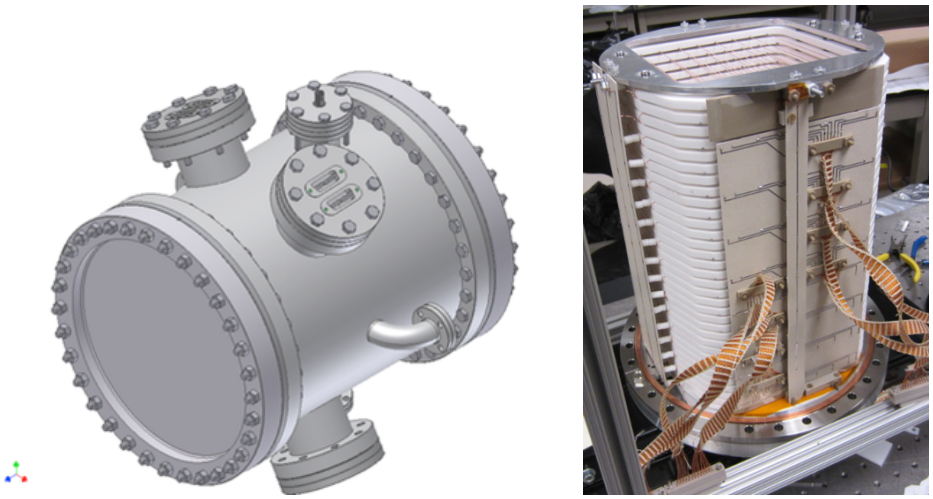

Figure 2.6: Computer Aided Design drawing of the ion chamber and picture of the interior Macor frame stack.

of 16 vertical signal wire planes of 9 wires each, which are sandwiched between 17 vertical High Voltage (HV) wire planes of 8 wires each. The high voltage is set at 350 volts and is maintained on all HV wire planes by two wires routed through high voltage feedthroughs. A graphic showing the placement of all wires is illustrated by figure 5.3 in chapter 5.

The 144 signal wires are grouped into four separate bundles of 36 wires each and routed to the vacuum side of four signal wire feedthroughs. The air side of the feedthroughs connect to pre-amplifier circuit boards which reside inside square enclosures attached to ion chamber. The square enclosures can be seen in figure 2.7 resting around the perimeter of the ion chamber. Each enclosure receives a steady flux of nitrogen gas serving as a coolant for the pre-amplifier circuit boards when they

are in operation. The analog signals from the pre-amplifiers are sent to analog-to-digital (ADC) converters allowing the resulting digital signal to be recieved by the data acquisition computer.

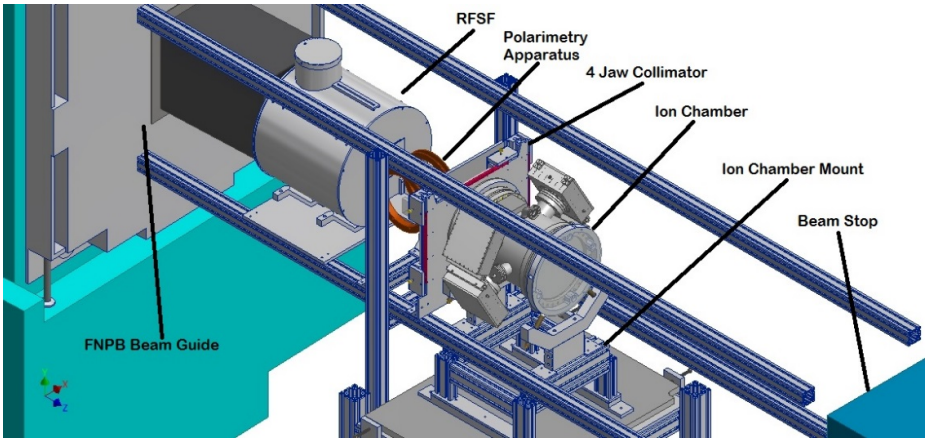

Figure 2.7: Computer Aided Design drawing of the n^{3}He experiment: Courtesy Eric Plemons.

The chamber also contains two gas feedthrough valves allowing it to be evacuated and then filled with ^{3}He before data production begins. The density ρ of ^{3}He gas in the ion chamber is important for several reasons. First, the rate of neutrons interacting with the gas will be proportional to ρ for densities which are not too large. However, ρ is also important because it determines the mean free path of both the proton and the triton emitted from the decaying nucleus. In addition, ρ also dictates the maximum value of the high voltage potential which can be applied to the ion chamber since higher densities can induce arcing between the wires.

For the n^{3}He experiment important measurements on the ion chamber after filling were the pressure and temperature of the gas:

$$P = 7.0 \text{ psi} \qquad T = 21.33 \text{ deg C} \tag{2.5}$$

Using these data points it is not necessary to know the volume of the ion chamber to determines the density of the gas inside. Its value can be determined from a variation

of the ideal gas law in the form

$$P = \frac{R}{M}\rho T \tag{2.6}$$

where R is the universal gas constant and M is the molar mass of the isotope. For ^{3}He—which is the only gas in the ion chamber—this value is determined from tables to be $M = 3.01603$ grams per mole. Substituting values then determines the density

$$\rho = 5.945 \times 10^{-5} \text{ grams/cm}^3 \tag{2.7}$$

Based on approximate dimensions of the ion chamber, one estimate indicates a total mass of ^{3}He in the ion chamber to be about 1 gram.

The operation of the ion chamber during data production is not complicated. The polarized beam of neutrons interacts with ^{3}He in the chamber producing decay protons and tritons with ranges of about 1-10 cm. The decay particles are both charged and can ionize other helium atoms in the chamber at the expense of their own kinetic energy. The free electrons then generate small currents in the signal wires which are amplified, digitized, and forwarded to the DAQ electronics.

2.2.4 Guide Field

The n^{3}He experiment did not require the design and construction of a system of wire coils to produce the guide field since a guide field from the previous experiment (NPDGamma) was already installed and operational [15, 16]. A photograph of the wire coils is shown in figure 2.8. The total interior magnetic field derives from 4 main horizontal racetrack coils with a set of four compensation coils placed around the perimeter on the structural suppports. The two central ractrack coils are 18.25 inches apart and contain 18 wire windings each. Outer racetrack coils are placed 30.75 above and below adjacent inner coils and contains 39 wire windings each. All four coils are connected in series to the main power supply. In addition, each of the four coils also contain 12 wire windings connected in series to a separate auxiliary

Figure 2.8: Guide field is generated from four main horizontal coils. The red lines indicate the location of the beam right and back shim coils.

power supply. Finally, four individual compensation coils are connected to their own power supplies and can be adjusted independently.

Table 2.1: Settings for all guide field powers supplies.

Power Supply	**Coil**	**Current (amps)**
Danfysik 896	Main	21.98
BK Precision	Auxiliary	3.2
Agilent E3648A	Left Shim	0.252
Agilent E3648A	Right Shim	0.542
Agilent E3648A	Back Shim	0.068
Agilent E3648A	Front Shim	0.068

During data production all power supplies were run in current mode at the current settings[†] shown in table 2.1. However, the auxiliary power supply recieved minor adjustments during polarimetry to maximize spin flipper efficiency. The only other exception was a time period between mid-March and Mid-April when the main power

[†]These settings were pre-determined by an alignment procedure ensuring that the resulting field was perpendicular to gravity at the center of the ion chamber, see [17].

supply (Danfysik 896) was set just over 22 amps to account for an abrupt drop in the field of about 40 mG.

A set of two magnetometers installed just above the spin flipper are configured to relay three axis magnetic field data every 12 second to the DAQ electronics. Plots showing the trend of this field during the course of the experiment have been included in figure A.1 of the appendix. The high current setting on the Danfysik in the March/April time frame can be seen in the top plot and was corrected during April polarimetry.

Chapter 3

Spin Flipper

The spin flipper [18, 19] is a major component of the n^{3}He experiment with a design based on the theory of double cosine theta coils [13]. Two impressive properties of the spin flipper are its highly uniform interior field, and its ability to flip either transverse or longitudinally polarized neutrons. This chapter covers all the design features of the spin flipper as well as integation of spin flipper electronics with other parts of the experiment.

3.1 Fields of a Cosine-Theta Coil

A ***cosine-theta coil*** is a long hollow cylindrical coil of radius R_{in} having a spatially uniform magnetic field in its interior transverse to the symmetry axis of the coil. For the static problem, the field is determined by an applied surface current density

$$\boldsymbol{k}(\phi) = k \sin\phi \, \hat{\boldsymbol{z}} \tag{3.1}$$

which is the continuum limit of a large number of wires. The resulting field is most easily determined using the theory of a magnetic scalar potential. In regions of zero

current density the magnetic field adheres to the curl equation

$$\boldsymbol{\nabla} \times \boldsymbol{H} = 0 \tag{3.2}$$

implying a scalar potential from the relation $\boldsymbol{H} = -\boldsymbol{\nabla} U$.

For reference, transformation equations for the unit vectors in cartesian and polar coordinates are:

$$\hat{\boldsymbol{r}} = \cos\phi\,\hat{\boldsymbol{x}} + \sin\phi\,\hat{\boldsymbol{y}} \qquad \hat{\boldsymbol{x}} = \cos\phi\,\hat{\boldsymbol{r}} - \sin\phi\,\hat{\boldsymbol{\phi}}$$
$$\hat{\boldsymbol{\phi}} = -\sin\phi\,\hat{\boldsymbol{x}} + \cos\phi\,\hat{\boldsymbol{y}} \qquad \hat{\boldsymbol{y}} = \sin\phi\,\hat{\boldsymbol{r}} + \cos\phi\,\hat{\boldsymbol{\phi}}$$

Potentials and fields associated with the coil can be divided into two regions: $r \leq R_{in}$ and $r > R_{in}$. Since $\boldsymbol{\nabla} \cdot \boldsymbol{H}$=0, the general form of the scalar potential in either region will be a solution to Laplace's equation $\boldsymbol{\nabla}^2 U = 0$ and is of the general form

$$U(r,\phi) = a_o + b_o \ln r + \sum_{n=0}^{\infty} (a_n r^n + b_n r^{-n})(c_n \cos n\phi + d_n \sin n\phi) \tag{3.3}$$

A unique solution is available through the application of the boundary condition connecting the inside of the cylinder to the outside of the cylinder.

$$(\boldsymbol{H}_{in} - \boldsymbol{H}_{out}) \times \hat{\boldsymbol{r}} = \boldsymbol{k} \qquad r = R_{in} \tag{3.4}$$

One finds interior and exterior solutions

$$U_{in} = -\frac{kr}{2}\cos\phi \qquad U_{out} = \frac{kR_{in}^2}{2r}\cos\phi \tag{3.5}$$

and leading to magnetic fields given by

$$\boldsymbol{H}_{in} = \frac{k}{2}[cos\phi\,\hat{\boldsymbol{r}} - \sin\phi\,\hat{\boldsymbol{\phi}}] \qquad \boldsymbol{H}_{out} = \frac{kR_{in}^2}{2r^2}[\cos\phi\,\hat{\boldsymbol{r}} + \sin\phi\,\hat{\boldsymbol{\phi}}] \tag{3.6}$$

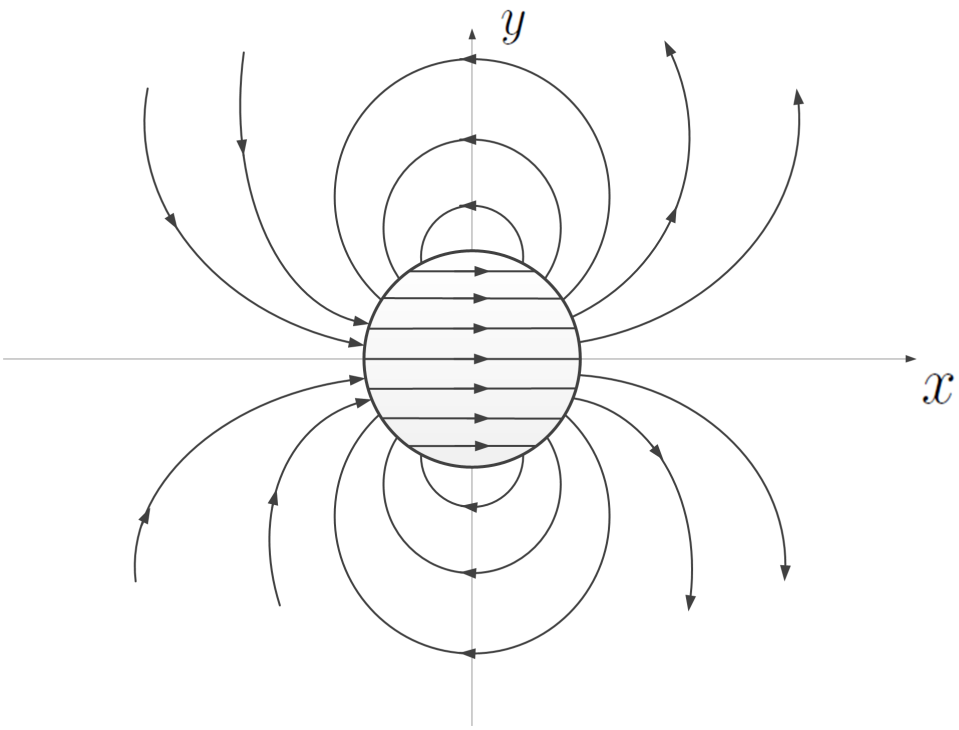

Figure 3.1: Diagram showing magnetic field lines inside and outside the radius R_{in} of the cosine-theta coil.

A graphical depiction of the magnetic fields is shown in figure 3.1.

The interior solution is the required constant magnetic field $\boldsymbol{H}_{in} = H_x\hat{\boldsymbol{x}}$. The exterior field might be referred to as a dipole field per unit length of z-axis and falling off as r^{-2}. It is a simple matter to verify that both fields have zero divergence and also satisfy equation (3.4).

A real cosine-theta coil will be characterized by an integer N equal to the total number of wires routed along the surface of the coil. The separation Δx between adjacent wires around the perimeter is constant and has a value

$$\Delta x = \frac{4R_{in}}{N} \tag{3.7}$$

The magnetic field in the interior region follows by summing the contribution to the field from each of the N wires. At the center of the cylinder the magnitude of the

field can be written

$$H_x = \frac{I}{2\pi R_{in}^2} \sum_{i=1}^{N} \|y_i\| \tag{3.8}$$

where $\|y_i\|$ is the vertical distance of each wire from the x-axis. Now consider the quantity

$$H_x \cdot \Delta x = \frac{I}{2\pi R_{in}^2} \left[\sum_{i=1}^{N/2} 2\|y_i\| \cdot \Delta x \right] \tag{3.9}$$

But if N is large, the term in parenthesis is a good approximation to the area of the circle, or πR_{in}^2. Inserting equation (3.7) derives an approximate formula for H_x in terms of the number N. More generally, the fundamental relation

$$4kR_{in} = NI \tag{3.10}$$

implies that the fields of a cosine theta coil composed of N wires around its circumference ($N/2$ current loops) are

$$\boldsymbol{H}_{in} = \frac{NI}{8R_{in}}[cos\phi\,\hat{\boldsymbol{r}} - \sin\phi\,\hat{\boldsymbol{\phi}}] \qquad \boldsymbol{H}_{out} = \frac{NIR_{in}}{8r^2}[\cos\phi\,\hat{\boldsymbol{r}} + \sin\phi\,\hat{\boldsymbol{\phi}}] \tag{3.11}$$

3.2 Fields of a Double Cosine-theta Coil

A theory of a ***double cosine-theta coil*** follows from the introduction of a second cosine-theta coil— concentric with the first coil and having a radius R_{out}. The fields of this design are illustrated in figure 3.2 and show the primary purpose of ensuring that the field external to both coils is zero. The neccessity of a vanishing external field has already been alluded to in section 2.2.1. With this requirement the current densities $\boldsymbol{k}_{in}(\phi)$ and $\boldsymbol{k}_{out}(\phi)$ will necessarily point in opposite directions along the z-axis so that scalar potentials associated with each coil are:

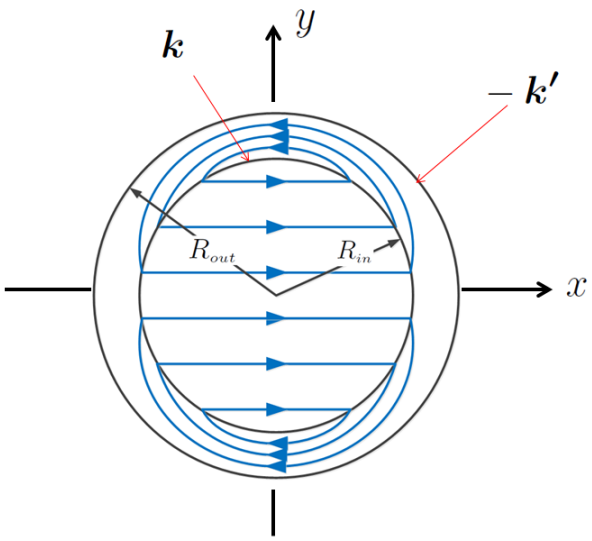

Figure 3.2: External field lines of a double cosine-theta coil with the requirement of no external field. Field lines from the inner coil get squeezed in between R_{in} and R_{out}.

$$U_{1in} = -\frac{k_{in} r}{2}\cos\phi \qquad r \leq R_{in} \qquad U_{1out} = \frac{k_{in} R_{in}^2}{2r}\cos\phi \qquad r > R_{in} \tag{3.12}$$

$$U_{2in} = \frac{k_{out} r}{2}\cos\phi \qquad r \leq R_{out} \qquad U_{2out} = -\frac{k_{out} R_{out}^2}{2r}\cos\phi \qquad r > R_{out} \tag{3.13}$$

Cancellation of the field in the region $r > R_{out}$ requires that current densities and individual radii are connected by the formula

$$k_{in} R_{in}^2 = k_{out} R_{out}^2 \tag{3.14}$$

In addition to this, the magnitude of the interior field will be

$$H_{rf} \equiv \frac{1}{2}(k_{in} - k_{out}) > 0 \tag{3.15}$$

Both of the two previous equations can be written in terms of coils composed of N_{in} and N_{out} wires. Specifically,

$$N_{in}R_{in} = N_{out}R_{out} \qquad\qquad H_{rf} \equiv \frac{I}{8}\left[\frac{N_{in}}{R_{in}} - \frac{N_{out}}{R_{out}}\right] \tag{3.16}$$

Potentials for the coil in the two non-zero regions can now be written

$$\begin{aligned} U_{in}(r,\phi) &= -H_{rf} r\cos\phi & r &\le R_{in} \\ U_{out}(r,\phi) &= \left[\frac{R_{in}^2}{R_{out}^2 - R_{in}^2}\right] H_{rf} \left[r + \frac{R_{out}^2}{r}\right]\cos\phi & R_{in} &< r < R_{out} \end{aligned}$$

As before, the auxillary field follows from $\boldsymbol{H} = -\boldsymbol{\nabla}U$. Inside the inner cylinder the field is constant and transverse to the axis of the cylinder so that $\boldsymbol{H}_{in} = H_{rf}\hat{\boldsymbol{x}}$. In the outer region the field is more complicated and given by

$$\boldsymbol{H}_{out}(r,\phi) = \frac{R_{in}^2}{R_{out}^2 - R_{in}^2} H_{rf}\left[-\left(1 - \frac{R_{out}^2}{r^2}\right)\cos\phi\,\hat{\boldsymbol{r}} + \left(1 + \frac{R_{out}^2}{r^2}\right)\sin\phi\,\hat{\boldsymbol{\phi}}\right] \tag{3.17}$$

It is a simple matter to show that $\boldsymbol{\nabla}\cdot\boldsymbol{H} = 0$ in both regions. Current densities can also be derived from equations similar to (3.4).

3.3 Surface Currents on a Finite Coil

The theory of a double cosine-theta coil presented so far assumes translational invariance in the z-direction. However, a functioning coil will have a length of 1-2 feet so it will be necessary to modify the design for some length z_o without significantly changing the fields—especially in the region $r \le R_{in}$. Realistically, this can be done by an astute choice of electrical currents running along two cross-sections separated by length z_o.

Calculation of Surface Currents: The fields inside of the infinite double cosine-theta coil can be used to determine surface current densities along two cross-sections of

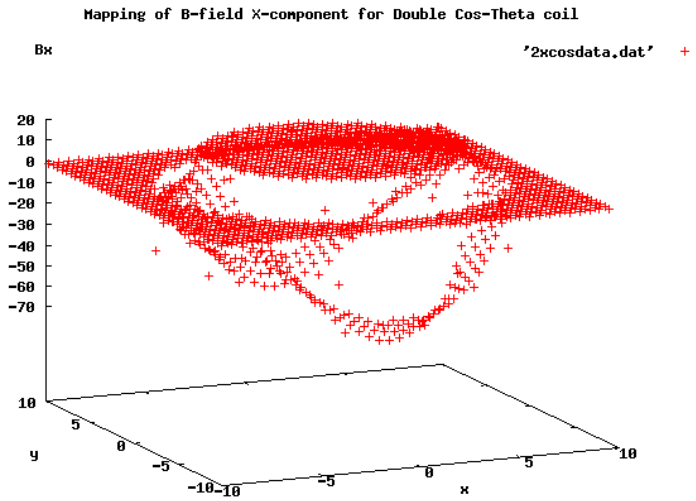

Figure 3.3: Computer simulation of the x-component of $\boldsymbol{H}$ for the double cosine-theta coil. The field is complicated between the coils but is constant in the interior and zero for all points outside the coil.

the finite length coil. Before mapping these current densities it is useful to implement equation (3.4) to calculate z-directed surface currents moving along R_{in} and R_{out}. These currents are easily shown to be

$$\boldsymbol{\mathcal{K}}_{in} = (\boldsymbol{H}_{in} - \boldsymbol{H}_{out}) \times \hat{\boldsymbol{r}}\,|_{r=R_{in}} = k_{in} \sin\phi\, \hat{\boldsymbol{z}} \tag{3.18a}$$

$$\boldsymbol{\mathcal{K}}_{out} = \quad - \boldsymbol{H}_{out} \times \hat{\boldsymbol{r}}\,|_{r=R_{out}} = -k_{out} \sin\phi\, \hat{\boldsymbol{z}} \tag{3.18b}$$

where the two surface currents are given by

$$k_{in} = \frac{2R_{out}^2}{R_{out}^2 - R_{in}^2} H_{rf} \qquad\qquad k_{out} = \frac{2R_{in}^2}{R_{out}^2 - R_{in}^2} H_{rf} \tag{3.19}$$

These two formulas can also be derived by inverting equations (3.14) and (3.15).

Equations for current densities moving along a given cross-section of a finite coil can be derived by forming the cross-product of a unit surface vector with appropriate

magnetic field vectors. For the region $r \leq R_{in}$ write

$$\boldsymbol{\mathcal{K}}_{<} = \boldsymbol{H}_{in} \times \hat{\boldsymbol{z}} = -H_{rf}\,\hat{\boldsymbol{y}} \tag{3.20}$$

Calculation of the current density between R_{in} and R_{out} follows in a similar manner by crossing $\hat{\boldsymbol{z}}$ into equation (3.17):

$$\boldsymbol{\mathcal{K}}_{>} = \frac{R_{in}^2}{R_{out}^2 - R_{in}^2} H_{rf} \left[1 + \frac{R_{out}^2}{r^2}\right] \sin\phi\,\hat{\boldsymbol{r}} + \frac{R_{in}^2}{R_{out}^2 - R_{in}^2} H_{rf} \left[1 - \frac{R_{out}^2}{r^2}\right] \cos\phi\,\hat{\boldsymbol{\phi}} \tag{3.21}$$

Evaluating this current density at R_{out} shows that the component along the direction $\hat{\boldsymbol{\phi}}$ vanishes. Meanwhile the magnitude of the component along $\hat{\boldsymbol{r}}$ becomes identical to $\boldsymbol{\mathcal{K}}_{out}$. For convenience figure 3.4 shows a schematic of the surface currents moving along a cross-section. To evaluate Current densities at the opposing face it is only

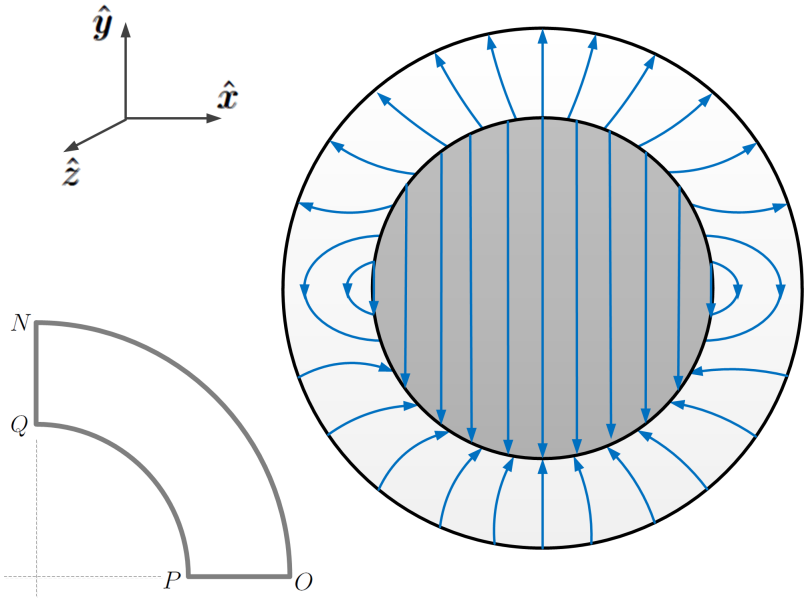

Figure 3.4: Blue arrows indicate the flow of current along an endface of a double cosine-theta coil. Black circles define the radii R_{in} and R_{out}.

required to reverse the direciton of the unit surface vector which changes the sign of $\boldsymbol{\mathcal{K}}_{<}$ and $\boldsymbol{\mathcal{K}}_{>}$. All the blue arrows in figure 3.4 are then reversed.

Total Currents in the Coil: Kirchoff's laws and conservation of current throughout the double cosine-theta coil can be verified by integrating current densities over selected boundaries at an endface. The entire solution to the problem can be reduced to calculations over a single quadrant of the coil so the schematic at the bottom left in figure 3.4 has been included for the purpose of displaying integration boundaries. In general, for any given boundary, the total current follows by integrating over a line perpendicular to the direction of the current using the formula

$$I = \int \boldsymbol{\mathcal{K}} \cdot d\boldsymbol{l}_{\perp} \tag{3.22}$$

First define total currents running prallel to the z-axis along R_{in} and R_{out}:

$$I_{in} \equiv \text{Current flowing into endface at } \overline{QP} \tag{3.23}$$

$$I_{out} \equiv \text{Current flowing out of endface at } \overline{NO} \tag{3.24}$$

These quantities can be determined using the current densities $\boldsymbol{\mathcal{K}}_{in}$ and $\boldsymbol{\mathcal{K}}_{out}$ along with the differential line element $d\boldsymbol{l}_{\perp} = Rd\phi\,\hat{\boldsymbol{z}}$. The elementary integrals are:

$$I_{in} = \frac{2R_{out}^2 R_{in}}{R_{out}^2 - R_{in}^2} H_{rf} \qquad\qquad I_{out} = \frac{2R_{in}^2 R_{out}}{R_{out}^2 - R_{in}^2} H_{rf} \tag{3.25}$$

The current I_{in} arriving at $\overline{QP}$ divides into a current which flows down the endface for all $r < R_{in}$ and a current flowing across $\overline{QP}$. Define

$$I_{DN} \equiv \text{Current flowing down endface from } \overline{QP} \tag{3.26}$$

$$I_{QP} \equiv \text{Current flowing across } \overline{QP} \tag{3.27}$$

which can be determined using current densities $\boldsymbol{\mathcal{K}}_{<}$ and $\boldsymbol{\mathcal{K}}_{>}$ producing the results

$$I_{DN} = H_{rf} R_{in} \qquad\qquad I_{QP} = \frac{R_{in}^3}{R_{out}^2 - R_{in}^2}\left[1 + \frac{R_{out}^2}{R_{in}^2}\right] H_{rf} \tag{3.28}$$

The first Kirchoff equation is easily verified to be

$$I_{in} = I_{QP} + I_{DN} \tag{3.29}$$

The second Kirchoff equation can be derived by showing the current flowing across $\overline{QP}$ into the interior region of the closed curve is equal to the current flowing out across the boundariy $\overline{NO}$ plus whatever current is flowing across $\overline{PO}$. No calculation is necessary for $\overline{QN}$ since current is everywhere parallel to this boundary. Define

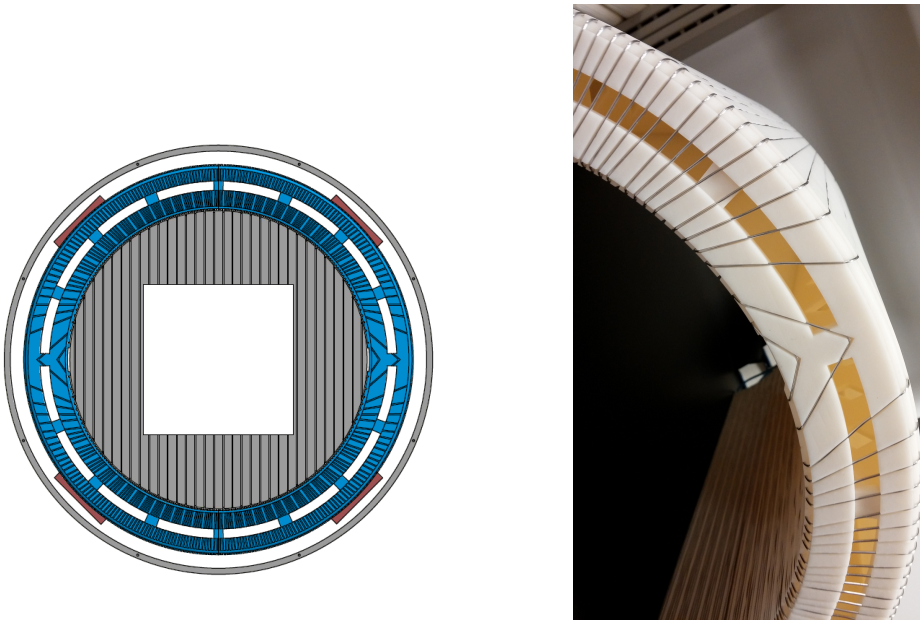

Figure 3.5: Picture and Schematic showing grooves for wire placement on a double cosine-theta coil

$$I_{NO} \equiv \text{Current flowing out through } \overline{NO} \tag{3.30}$$

$$I_{PO} \equiv \text{Current flowing out through } \overline{PO} \tag{3.31}$$

Both results here follow by integrations over $\boldsymbol{\mathcal{K}}_{>}$ using appropriate integration limits. Results are

$$I_{NO} = \frac{2R_{in}^2 R_{out}}{R_{out}^2 - R_{in}^2} H_{rf} \qquad I_{PO} = \frac{R_{in} H_{rf}}{R_{out}^2 - R_{in}^2} \left[R_{out}^2 - 2R_{out}R_{in} + R_{in}^2 \right] \tag{3.32}$$

and the second Kirchoff equation is

$$I_{QP} = I_{out} + I_{PO} \tag{3.33}$$

Surface Currents on the n^{3}He Spin Flipper: The spin flipper for the n^{3}He experiment is constructed with $N_{in} = 320$ parallel wires around its circumference at $r = R_{in}$. The current I_{in} is determined from 80 wires of which 16 are routed downward along the inner cylinder implying

$$I_{QP} = 4 \cdot I_{DN} \tag{3.34}$$

This information determines all other currents in the coil by constraining the inner and outer radius through the relation

$$R_{out} = \sqrt{\frac{5}{3}} R_{in} \tag{3.35}$$

Relative values of the individual currents are shown in Table 3.1. Unfortunately the second Kirchoff relation in (3.33) cannot be satisfied exactly because I_{NO} and I_{PO} are required to share 64 wires. The best result allocates 2 wires for I_{PO} and shows that

$$I_{NO} = 24.217\, H_{rf} \qquad \text{and} \qquad I_{PO} = 0.781\, H_{rf} \tag{3.36}$$

Percent differences with ideal values give

$$\Delta_{NO} = 0.046\,\% \qquad \text{and} \qquad \Delta_{PO} = 1.64\,\% \tag{3.37}$$

Table 3.1: Surface currents on a double cosine-theta coil. The last column is determined from the initial value $R_{in} = 6.320$ inches.

No.	Current	Value 1	Value 2
1	I_{out}	$3R_{out}H_{rf}$	$24.447H_{rf}$
2	I_{in}	$5R_{in}H_{rf}$	$31.600\,H_{rf}$
3	I_{QP}	$4R_{in}H_{rf}$	$25.280\,H_{rf}$
4	I_{NO}	$3R_{out}H_{rf}$	$24.447H_{rf}$
5	I_{PO}	$0.127R_{in}H_{rf}$	$0.803\,H_{rf}$
6	I_{DN}	$R_{in}H_{rf}$	$6.320\,H_{rf}$

Since the two wires composing I_{PO} are routed back to the R_{in} this means that the outer coil is a cosine-theta coil designed for 62 wires per quadrant.

3.4 Inductance of Cosine-Theta Coils

Calculations of the fields produced by cosine-theta coils presented thus far assume input currents and current densities which do not change with time. However, the spin flipper will be driven at an RF frequency transforming its interior coils into and LR circuit, and this motivates the need for an understanding of coil inductance. For the theoretical infinite length coils, the meaningful quantity to calculate is the inductance per unit length; but a more realistic problem of a coil with length z_o provides only minor additional complications in the calculation.

Indutance of a Cosine-Theta Coil: For a coil composed of N wires there are $N/2$ current loops and the total flux through the coil is given by

$$\Phi = \sum_{i=1}^{N/2} \Phi_i = LI \tag{3.38}$$

The flux through each current loop is given by the surface integral

$$\Phi_i = \int_s \mathbf{B} \cdot d\mathbf{S}_i \tag{3.39}$$

but the magnetic field in the interior region is constant and points in the same direction as $d\mathbf{S}$, so

$$\Phi_i = B_x \cdot S_i = \mu_o H_x \cdot S_i \tag{3.40}$$

where S_i is the area enclosed by each loop. The total inductance is therefore

$$\Phi = \mu_o H_x \sum_{i=1}^{N/2} S_i \tag{3.41}$$

and is proportional to the total area enclosed by the individual wire loops. Consider instead the quantity

$$\Phi \cdot \Delta x = LI \cdot \Delta x = \mu_o H_x z_o \left[\sum_{i=1}^{N/2} 2\|y_i\| \cdot \Delta x \right] \tag{3.42}$$

which can be compared to equation (3.9). Again, the value in parentheses approximates the area of the circle of radius R_{in}. Employing equation (3.7) the inductance of the cosine-theta coil is

$$\boxed{L = \frac{\mu_o \pi z_o}{32} N^2} \tag{3.43}$$

This same result also follows from a determination of the total energy stored in the magnetic field. The energy inside the coil follows immediately as

$$E_{in} = \frac{\mu_o \pi z_o}{2} \left[\frac{NI}{8} \right]^2 \tag{3.44}$$

The stored energy outside the coil gives the same result. Now write

$$E_{total} = 2E_{in} = \frac{1}{2}LI^2 \tag{3.45}$$

and solve for the inductance.

Inductance of a Double Cosine-Theta Coil: The inductance of a double cosine-theta coil is a more difficult problem to address then a cosine-theta coil. For definiteness it will be assumed here that a double cosine-theta coil is defined by the requirement of a zero external field everywhere. This is an important constraint on the radii and the number of wires, and simplifies the calculation.

The total magnetic field energy in the coil in each of two regions is given by

$$E = \frac{\mu_o}{2}\int |\boldsymbol{H}|^2 dv \tag{3.46}$$

In the region $r \leq R_{in}$ the answer is almost trivial since the field is constant. One finds

$$E_{in} = \frac{\mu_o}{2}H_{rf}^2 \pi R_{in}^2 z_o \tag{3.47}$$

In the region $R_{in} < r < R_{out}$ the integral is somewhat more complicated with the result

$$E_{out} = \frac{\mu_o \pi H_{rf}^2 z_o}{2}\left[\frac{R_{in}^2}{R_{out}^2 - R_{in}^2}\right]^2 \cdot \left[\frac{R_{out}^4}{R_{in}^2} - R_{in}^2\right] \tag{3.48}$$

Now use

$$E_{in} + E_{out} = \frac{1}{2}LI^2 \tag{3.49}$$

and solve the for the inductance.

$$L = \mu_o \pi R_{in}^2 z_o \cdot \frac{H_{rf}^2}{I^2}\left[\frac{2R_{out}^2}{R_{out}^2 - R_{in}^2}\right] \tag{3.50}$$

To complete the calculation it is necessary to insert both equations in (3.16) so that L appears in terms of geometric quantities only. A symmetric form of the final result

is

$$\boxed{L = \frac{\mu_o \pi z_o}{32} N_{in} N_{out} \left[\frac{R_{out}}{R_{in}} - \frac{R_{in}}{R_{out}} \right]} \tag{3.51}$$

Inductance of the n^{3}He Double Cosine-Theta Coil: The overall design initiative for the n^{3}He double cosine-theta coil is to have every 5th wire routed along the perimeter at R_{in} to be routed along the end faces of the inner cylinder. This condition locks in the ratio of the two radii and the two numbers N_{in} and N_{out} through the relation

$$\frac{R_{out}}{R_{in}} = \sqrt{\frac{5}{3}} = \frac{N_{in}}{N_{out}} \tag{3.52}$$

Actual values for these quantities along with the coil length are given in table 3.2. Inserting values into equation (3.51), gives an inductance of

$$L = 2.01265 \text{ mH} \tag{3.53}$$

This value is in excellent agreement with experimentally measured values obtained from resonance curves using a known capacitance.

Table 3.2: Specifications for the n^{3}He double cosine-theta coil

No.	Length
$N_{in} = 320$	$R_{in} = 6.320\,\text{in.}$
$N_{out} = 248$	$R_{out} = 8.159\,\text{in.}$
	$z_o = 15.60\,\text{in.}$

Independent Evaluation of L: Inductance of the double cosine-theta coil using specifications in Table 3.2 can also be deterimined from a good understanding of the derivation for the cosine-theta coil given previously. The total flux through the inner cylinder is

$$\Phi = \mu_o H_{rf} \sum_{i=1}^{N/2} S_i \tag{3.54}$$

which is identical to equation (3.41) except that H_x has been replaced by H_{rf}. Solving for the quantity L_{in} in the same manner gives

$$L_{in} = \frac{\mu_o H_{rf} \pi R_{in}^2 z_o}{I \cdot \Delta x} \tag{3.55}$$

But equation (3.52) can be inserted into equation (3.16) to show that

$$\frac{H_{rf}}{I} = \frac{1}{\Delta x} = \frac{N}{4R_{in}} \tag{3.56}$$

where $N = 64$ for the inner cylinder. The final result is

$$L_{in} = \frac{\mu_o \pi z_o N^2}{16} \tag{3.57}$$

which is double the result for a cosine-theta coil. To determine the contribution from outer cylinder loops it is only necessary to note that the total flux through the top half of the inner cylinder runs entirely through the top half of the outer cylinder. The only difference is that this flux traverses four times as many wire loops. This means that $L_{out} = 4 \cdot L_{in}$. The total inductance for the n^{3}He coil is therefore

$$\boxed{L = \frac{5}{16} \mu_o \pi z_o N^2} \tag{3.58}$$

This is a useful formula for L given exclusively in terms of the number of wires routed along the inner cylinder.

3.5 Spin Flipper and Spin Magnetic Resonance

The rotation of neutron spins inside the spin flipper is easily described by the classic two-state problem of Spin Magnetic Resonance [12]. Spins emerging from the supermirror polarizer are initially polarized along the direction of the guide field $\boldsymbol{B}_o$. Figure 3.6 shows these vectors along with the transverse field $\mathbf{B}_{rf}$ produced by the

spin flipper. When the spin flipper is off the initial quantum mechanical Hamiltonian

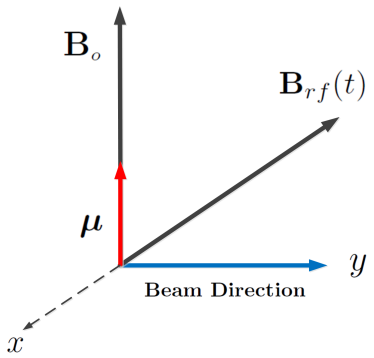

Figure 3.6: Vectors for the SMR problem with $\mathbf{B}_{rf}$ oscillating in the horizontal plane. The direction of the beam should be along the $+z$ axis but is the direction of B_o for the purpose of solving the SMR problem.

for the neutrons interacting with the guide field is approximately represented by the two-state matrix

$$H = \begin{bmatrix} \frac{\hbar\omega_L}{2} & 0 \\ 0 & -\frac{\hbar\omega_L}{2} \end{bmatrix} \qquad \text{where} \qquad \omega_L = \gamma_n B_o \tag{3.59}$$

For neutrons inside an energized spin flipper, the magnetic moment μ_n interacts with the total field producing a small change to the original Hamiltonian ΔH. This total field is

$$\boldsymbol{B} = B_o\hat{\boldsymbol{z}} + B_{rf}\cos\omega t\hat{\boldsymbol{x}} \tag{3.60}$$

but to apply the RF portion for an SMR calculation requires that it be written as the sum of two fields which rotate in opposite directions [20]

$$\boldsymbol{B}_{rf} = \frac{B_{rf}}{2}(\cos\omega t\hat{\boldsymbol{x}} + \sin\omega t\hat{\boldsymbol{y}}) + \frac{B_{rf}}{2}(\cos\omega t\hat{\boldsymbol{x}} - \sin\omega t\hat{\boldsymbol{y}}) \tag{3.61}$$

The clockwise component can be associated with a positive frequency ω while the counter-clockwise component follows from the replacement $\omega \to -\omega$. This component is highly supressed by the SMR calculation and can be ignored. The contributing

component then allows ΔH to be written

$$\Delta H = \gamma_n \mathbf{S} \cdot \boldsymbol{B}_{rf} = \begin{bmatrix} 0 & \hbar\omega_F e^{i\omega t} \\ \hbar\omega_F e^{-i\omega t} & 0 \end{bmatrix} \qquad \text{where} \qquad \omega_F \equiv \frac{\gamma_n B_{rf}}{4} \tag{3.62}$$

The perturbed two-state Hamiltonian inside the spin flipper is then

$$H + \Delta H = \frac{\hbar}{2} \begin{bmatrix} \omega_L & 2\omega_F e^{i\omega t} \\ 2\omega_F e^{-i\omega t} & -\omega_L \end{bmatrix} \tag{3.63}$$

The solution follows provided that $\omega_F/\omega_L << 1$. Its value is about 1/40 for n^3He experiment since the amplitude of the RF field is near 1 G. If the initial quantum wave function is a pure eigenstate of the unperturbed Hamiltonian then the probability of finding neutrons in a given state derives from the Rabi formula

$$P(t) = \frac{4\omega_F^2}{4\omega_F^2 + (\omega_L - \omega_{rf})^2} \sin^2 \left[\sqrt{\omega_F^2 + \frac{(\omega_L - \omega_{rf})^2}{4}}\, t \right] \tag{3.64}$$

To rotate neutron spins by 180 degres with a probability approaching 1, it is necessary to drive the spin flipper at resonance. At this frequency, the Rabi formula simplifies to

$$P(\omega_{rf} \to \omega_L) = \sin^2 \omega_F t \tag{3.65}$$

For neutrons of specific energy E, this means we choose ω_F based on the total time δt these neutrons are exposed to the RF field. The angular frequency must be

$$\omega_F = \pi/2\delta t \tag{3.66}$$

to ensure $P \to 1$ and an appropriate equation for the RF field will be

$$B_{rf}(t) = \frac{4\omega_F}{\gamma_n} \cdot e^{i\omega_L t} \tag{3.67}$$

Table 3.3: Selected times δt for neutrons in the spin flipper.

No.	λ	velocity(v_n)	δt
1	6.5Å	608.620 m/s	0.6510 ms
2	5.0Å	791.205 m/s	0.5008 ms
3	3.5Å	1,130.294 m/s	0.3505 ms
4	2.5Å	1,582.411 m/s	0.2504 ms

SMR for a Wavelength Spectrum: The flux of neutrons through the spin flipper is actually composed of a distribution of de Broglie wavelengths in the approximate range $2.5A \leq \lambda \leq 6.5A$. For reference, Table 3.3 gives an indication of selected neutron velocities in this range along with the total time spent inside the spin flipper. The length of the spin flipper is $z_o = 39.62$ cm and this means that ω_F will depend on the wavelength of the neutron according to

$$\omega_F = \frac{\pi h}{2mz_o\lambda} \tag{3.68}$$

For a given pulse of neutrons, the amplitude of the RF field inside the spin flipper will therefore be required to decrease with a $1/t$ dependence over a time interval Δt and having the general form

$$B_{rf}(t) = \left[\frac{B_{max}}{1+\alpha t}\right] e^{i\omega_L t} \tag{3.69}$$

where α is a constant. An illustration of the RF field envelope provided by the spin flipper is shown in Figure 3.7. The spin flipper energizes at time t_i simultaneous with the arrival of the front of the pulse and then de-energizes at a time t_f later. The SNS provides pulses of neutrons at 60 Hz implying that the width of a pulse is

$$\Delta T = t_f - t_i = 16.667\,\text{ms} \tag{3.70}$$

The fastest neutrons will be located at the front of the pulse and receive that portion of the RF field with the largest amplitude. In contrast, the slowest neutrons are at

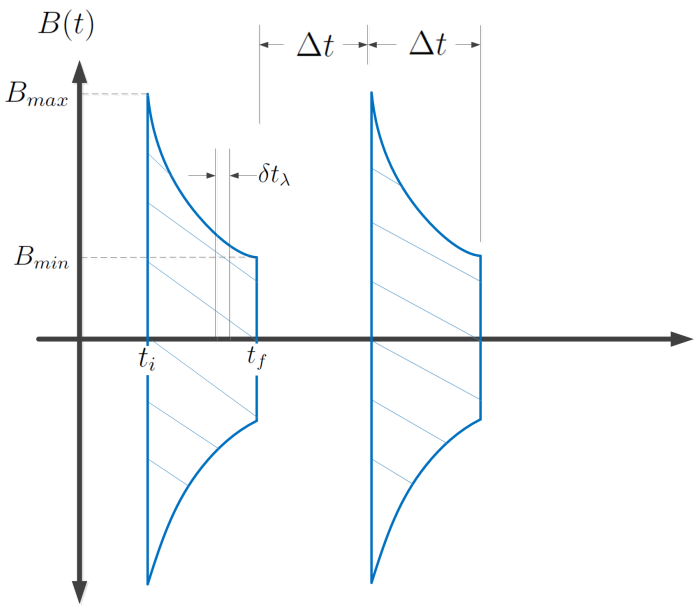

Figure 3.7: Magnetic field envelope provided to the spin flipper. The region of zero field between the pulses transmits neutrons without flipped spins.

the back of the pulse and receive the smallest field amplitude. The total time spent by any neutron in the spin flipper is δt_λ which is much smaller than the width of the pulse.

3.6 Spin Flipper as an RCL Circuit

The double cosine-theta coil inside the spin flipper has an inductance L determined by the coil geometry, and resistance R determined by the total length of wire in the coil. With a negligible capacitance it will behave as an LR circuit when driven at the neutron Larmor frequency. Since an LR circuit behaves as a low-pass filter this implies that an exceedingly large voltage will be required to produce currents necessary to flip the neutron spins. To minimize voltage requirements it will be sensible to include an external capacitance so that the coil circuit resonates near the Larmor frequency as an RCL circuit. A schematic of this circuit is shown in figure 3.8. While the

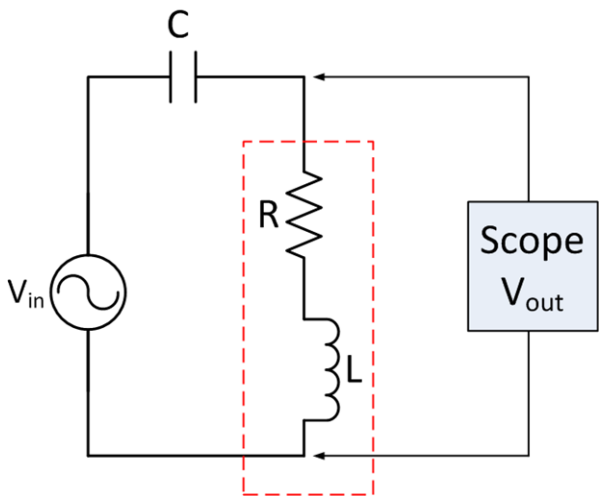

Figure 3.8: Circuit Diagram for the spin flipper coils with external capacitor and sinusoidal input.

capacitor is an independent circuit element, the red dashed line indicates that neither the resistance nor the inductance can be removed independently of each other.

Values for Resistance, Capacitance, and Inductance: In actual fact, the value chosen for the capacitance dictates not only the resonant frequency of the RCL circuit, but also the magnitude of the guide field B_o which is proportional to the Larmor frequency of the neutrons. Furthermore, any value of capacitance can be selected in a reasonable range to determine a guide field of approximately 8-12 Gauss. The value chosen for the n^{3}He experiment is $C = 17.70$ nF leading to

$$\omega_L = \frac{1}{\sqrt{LC}} \sim 1.68 \times 10^5\, s^{-1} \qquad B_o = \frac{\omega_L}{\gamma_n} \sim 9.15\,\mathrm{G} \tag{3.71}$$

The capacitance is determined by the manufacturer and is not an experimentally determined quantity. However, the resonant frequency of the circuit is measured quite accurately in equation (3.73) so that an experimental value of the coil inductance is possible:

$$L = 1/\omega_L^2 C = 2.014\mathrm{mH} \tag{3.72}$$

This differs from the theoretical value predicted by equation (3.58) by about 0.6 percent suggesting that the value of the capacitance is also quite accurate. The only other information needed is the resistance R of the coils which can either be determined by the 870 feet of wire used to make the coils and the resistivity of aluminum, or by a simple measurement using an ohm-meter. For reference, values for all circuit elements are summarized in Table 3.4.

Table 3.4: Values of spin flipper resistance, inductance, capacitance. Resistnce is determined with an ohm-meter.

R	C	L
9.11 Ω	17.70 nF	2.01 mH

Resonance Curve: A precise measurement of the spin flipper resonant frequency comes from the resonance curve shown in figure 3.9. Individual points on this curve

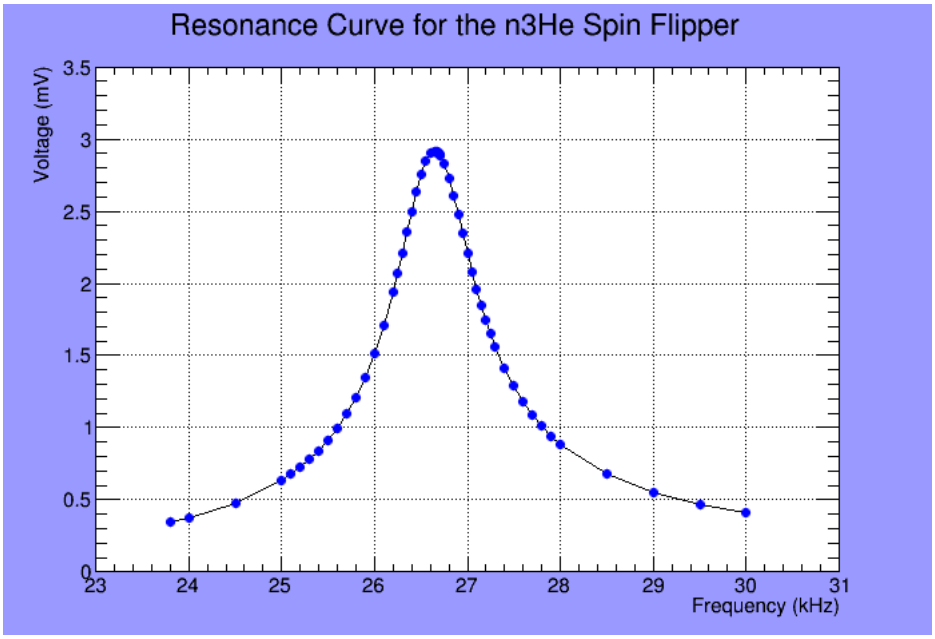

Figure 3.9: Resonance curve for the spin flipper

are made available using a small wire coil (probe) rigidly placed near the center of the spin flipper and connected to an SR860 lock-in amplifier [21]. When the frequency on

the lock-in amplifier is matched with a driving frequency applied to the spin flipper a voltage is produced by the probe indicative of magnetic flux enclosed by the probe. This voltage is the vertical axis in figure 3.9 and the curve V(f) has characteristics

$$V_{max} = 2.916\,\text{mV} \;@\; f = 26.655 \pm 0.005\text{kHz} \qquad \text{FWHM} \approx 1.4\text{kHz} \tag{3.73}$$

The Q-value is an important indicator for an RCL circuit determined by the resonace curve from the quantity $f/\Delta f$ where Δf is half of the FWHM. This value also follows from the definition

$$Q = \omega_L \cdot \frac{\text{Total stored energy}}{\text{Average power supplied at resonance}} \tag{3.74}$$

For the spin flipper:

$$Q = \frac{\omega_L L}{R} \approx 37.2 \tag{3.75}$$

Since $Q \gg 1$ this qualifies the spin flipper as an underdamped oscillator.

Steady State Power Formula: With an applied external voltage $V(t) = V_o e^{i\omega t}$, the steady state differential equation for the spin flipper circuit can be written in terms of the charge $q(t)$ on the capacitor:

$$L\frac{d^2q}{dt^2} + R\frac{dq}{dt} + \frac{q}{C} = V_o e^{i\omega t} \tag{3.76}$$

The real part of this solution and its first time derivative can be written

$$q(t) = \frac{V_o}{\omega\left[R^2 + (\omega L - \frac{1}{\omega C})^2\right]^{1/2}} \cdot \cos(\omega t + \phi) \tag{3.77}$$

$$I(t) = -\frac{V_o}{\left[R^2 + (\omega L - \frac{1}{\omega C})^2\right]^{1/2}} \cdot \sin(\omega t + \phi) \tag{3.78}$$

where the phase is given by

$$\phi = \arctan\left[\frac{R}{\omega L - \frac{1}{\omega C}}\right] \tag{3.79}$$

At resonance, the phase angle is $\pi/2$ so that the charge and the current are both out of phase with the driving voltage. The voltage across each circuit element can also be calculated at resonance:

$$V_C = -\frac{V_o}{R\omega C}\sin\omega t \qquad V_R = -V_o\cos\omega t \qquad V_L = \frac{\omega V_o L}{R}\sin\omega t \tag{3.80}$$

As an example, a 5Å neutron will require about 5 volts and with this value the signal amplitude across the capacitor and inductor are $V_C = -V_L = 185$ volts.

The average power supplied to the circuit evaluated over one cycle is given by

$$P_{avg} = \frac{V_o^2 R/2}{R^2 + (\omega L - \frac{1}{\omega C})^2} \tag{3.81}$$

This can also be evaluated at resonance simplifying to

$$P_{avg} = \frac{V_o^2}{2R} \tag{3.82}$$

This formula applies only to sinusoidal input voltages.

Power Requirements for the n^{3}He experiment: A more meaningful calculation for the n^{3}He experiment is a determination of the supplied power over a single pulse interval having a voltage (or current) envelope as in figure 3.7. The RF magnetic field amplitude can be determined as a function of wavelength from equation (3.67) and the current amplitude is related to the magnetic field amplitude by equation (3.16) or

$$B_{rf} = 99.59 \cdot \mu_o I \qquad \text{(units of Tesla)} \tag{3.83}$$

Using a wavelength spectrum $2.8 \leq I \leq 6.5$ Å and $T = 16.667$ ms, an accurate formula for the current amplitude in Amps is

$$I(t) = \frac{12.352}{12.605 + t} \qquad \text{where} \qquad 0 \leq t \leq T \tag{3.84}$$

The power delivered for a single pulse is then

$$P_{avg} = \frac{R}{2T} \int_0^T I^2(t) dt \tag{3.85}$$

This is easily integrated producing the result $P_{avg} \approx 1.88$ Watts.

3.7 Field Measurements inside the Spin Flipper

The double cosine-theta coil is specifically designed to have a uniform field in the interior region of the inner cylinder. Before installation of the spin flipper it is mandatory to perform at least some measurements of the field in this region to verify that the coil has been properly designed and wrapped.

Field measurements are possible by first energizing the spin flipper with the resonant frequency RF signal. The field can then be measured by inserting a probe attached to a lock-in amplifier. The probe is made with a thin wire wrapped at the end as a 10 times, 1 cm diameter coil. Tuning the lock-in amplifier to the RF signal then produces a voltage reading. This reading can be maximized by rotating the probe so that the axis of the 1 cm coil points along the direction of the magnetic field. Voltages are plotted in figure 3.10 from two randomly chosen entry points into the inner cylinder. The signal ramps by a factor of 100 over a distance of about 2 cm outside the coil, and then quickly levels off to its constant value near $V = 0.22$ volts inside the coil. This voltage can be converted to the amplitude B_{rf} of the oscillating magnetic field using Faraday's law:

$$B_{rf} = \frac{V}{N\omega\pi r^2} \tag{3.86}$$

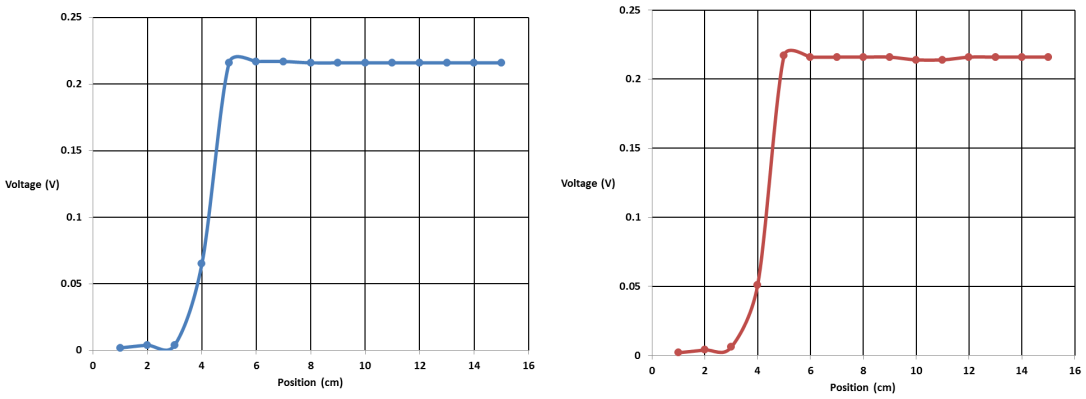

Figure 3.10: Field measurements inside the spin flipper

Here ω is the frequency of the input resonant signal, $N = 10$, and r is the probe radius. For reference, values of data points are included in the Appendix, tables A.1 and A.2.

3.8 Integration with DAQ Electronics

Following installation of the spin flipper and proper alignment with the neutron beam, it will be necessary to provide necessary electronics for generation of the appropriate waveform similar to the illustration in figure 3.7. In addition, a copy of the waveform must be routed to the data acquisition computer as a continous indicator that the spin flipper is operational during data production.

3.8.1 Circuit Diagram

A circuit diagram for the spin flipper electronics is shown in figure 3.11. The source waveform is generated by a Tektronix AWG-3022B function generator [22]. A cable routing the waveform to a Crown D-75 audio amplifier [23] features a coaxial connector at the output of the function generator connecting to an XLR/phone input connector at the audio amplifier. The power output capabilities of the amplifier far outweigh the requirements of the spin flipper so only one of its two channels is needed to

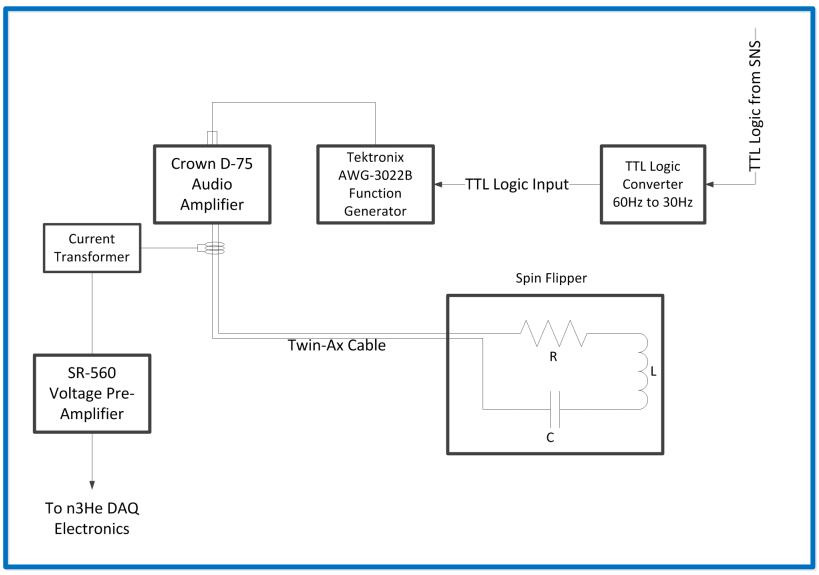

Figure 3.11: Diagram showing integration of spin flipper circuit with DAQ Electronics.

energize the spin flipper. During operation its voltage output is about 10-15 times the input voltage from the function generator. For consistency, the volume knob on the amplifier is set to a default maximum value and this allows the strength of the waveform sent to the spin flipper to be controlled exclusively and precisely by the function generator which can increment its output voltage by 1 millivolt or less.

Both the function generator and the DAQ electronics receive a trigger from the SNS 60 Hz TTL logic signal synchronized to the production of individual pulses of neutrons. Since the spin flipper is only energized for alternating pulses of neutrons, it is necessary to transform the 60 Hz signal allowing the function generator to trigger at only 30 Hz.

A wide band current transformer connected to the output of the amplifier relays a replica of the amplifier output waveform to the DAQ. The transformer is rated to generate a voltage of 0.1 volt per Ampere but the actual signal is less than this based on the high frequency of the amplifier output waveform at 26.65 kHz. For this reason the transformer signal receives a 10 times voltage gain from an SR-560 pre-amplifier [24] before being received on DAQ channel 30. The waveform is recorded by the

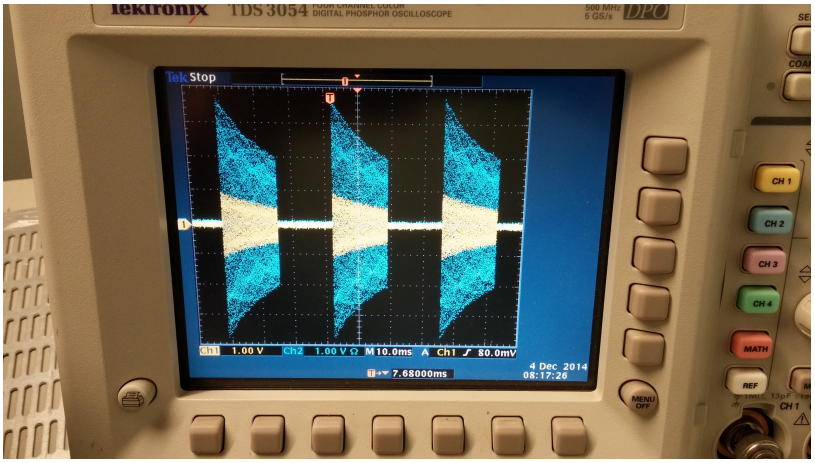

Figure 3.12: Magnetic field envelope for the spin flipper shown on an oscilliscope. The yellow signal on ch:1 is from the waveform generator. The blue signal on ch:2 has been amplified by the audio amplifier.

DAQ for each data run for confirmation that the spin flipper is operational during the course of data production.

3.8.2 Programmed Signal for the Function Generator

ArbExpress Ver3.1 is an arbitrary waveform editing tool from Tektronix. The software package is used to program a digital sinusoidal waveform with an amplitude that decreases as $1/t$. The programmed signal features $N = 444.25$ oscillations covering the time interval $\Delta T = 16.6667$ ms giving a frequency $N/\Delta T$ very close to the required Larmor frequency of neutrons in the guide field. The digital waveform is constructed using 65,000 equally spaced voltage points of a possible 2^{16} points allowed by the function generator. This means each sinusoidal oscillation is composed of approximately 146 discrete voltage points separated by about 0.25 μs. The completed waveform (shown on the oscilloscope in figure 3.12) is uploaded to the AFG-3022B using the USB port and routed to the audio amplifier by the TTL logic signal at 30 Hz.

Maximizing Spin Flipper Efficiency: An outstanding issue is the ratio of the signal amplitudes a and b at the beginning and the end of the pulse outputed by the function generator. The audio amplifier will amplify both ends of the input pulse by the same amount leaving the ratio a/b unchanged. However, the programmed value of a/b determines the amplitude ratio B_{max}/B_{min} inside the spin flipper and should be chosen to maxmimize the efficiency of the spin flipper. The optimal value for a/b

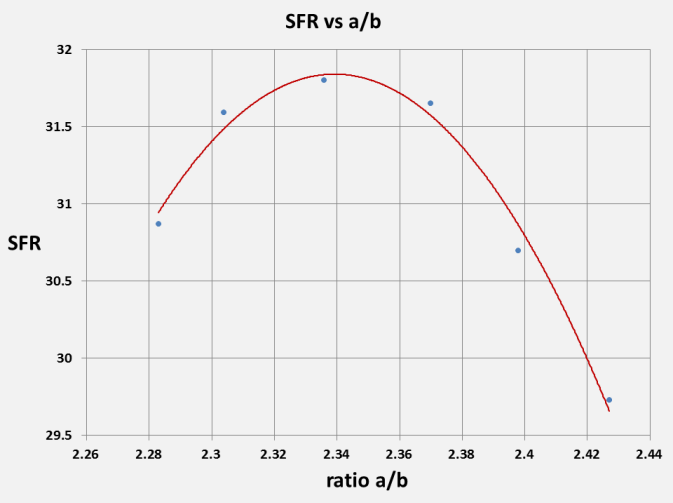

Figure 3.13: Plots associated with changes in the ratio a/b.

can be determined by preparing programmed wave forms using ArbExrpess software with slightly differing values of a/b. Figure 3.13 shows the calculated Spin Flip Ratio (SFR) from polarimetry measurements plotted against a/b for six different uploaded waveforms using an output function generator voltage of $V_a = 486$ mV. Maximizing spin flipper efficiency entails acquiring data at different voltages V_a for each chosen ratio. This generates a 2D max/min problem which can simultaneously locate an optimal V_a and a/b. Unfortunately, this technique was not used to maxmimize efficiency since $V_a = 486$ mV and $a/b = 2.370$ were initially chosen which provided satisfactory results. Any changes to initial settings were thought to be possibly problematic.

Spin Flipper Current Signal Read by the DAQ: The voltage rise time for the spin flipper circuit is on the order of a few μs. The waveform sent by the current transformer to the DAQ is determined by the current flowing in the signal wires sent to the spin flipper. The shape of this curve recorded by the DAQ is shown in 3.14 for two consecutive pulses. While the voltage rise times (slew rate) are very short, the current neccessarily lags the voltage and distorts the signal at both the beginning and the end of the pulse. The vertical line at the time 1624 occurs at 16.667 ms and

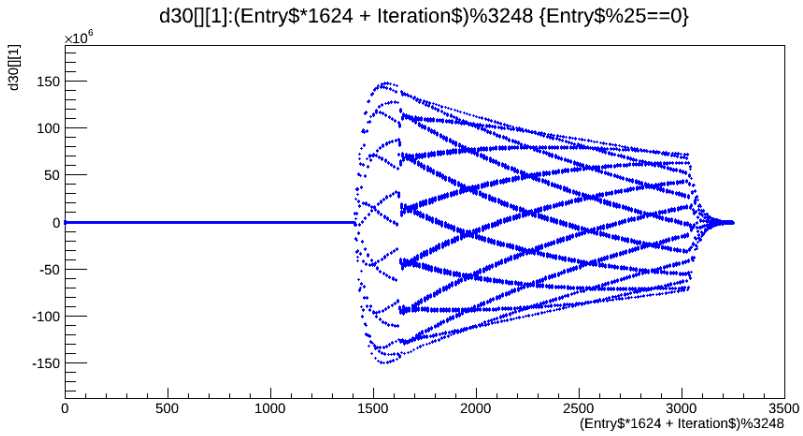

Figure 3.14: DAQ display of the current envelope sent to the spin flipper.

represents the end of a neutron pulse DAQ measurement followed by the beginning of the next measurement. Presence of the non-zero signal crossing into the region of the first pulse is based on ensuring that the rise time of the current does not interfere with the spin flipper signal required at the start of the second pulse.

Chapter 4

Neutron Polarimetry

Polarimetry measurements on the neutron beam are an essential part of the n^{3}He experiment for several reasons: The statistical evaluation of the physics asymmetry A_p depends on the average beam polarization $\langle P_n \rangle$, the average spin flipper efficiency $\langle \epsilon_{sf} \rangle$, and the observed asymmetry A_{obs} through the relation

$$A_p = \frac{A_{obs}}{\langle P_n \rangle \cdot \langle \epsilon_{sf} \rangle} \tag{4.1}$$

If A_p is to be measured with a precision of 10^{-8}, then the reasonable range estimates in equation (1.11) imply a statistical uncertainty in the neighborhood of 2%. This means that measurements of beam polarization and spin flipper efficiency should show a variability which is less than this.

Neutron polarimetry [25, 26, 27] was performed on a (roughly) monthly basis during data production. Calculated average values of beam polarization $\langle P_n(\lambda) \rangle$, Spin Flipper efficiency $\langle \epsilon_{sf}(\lambda) \rangle$, and the room background at each wavelength are given in Appendix A along with standard deviations. Averaging over all wavelengths leads to the results

$$\langle P_n \rangle = 0.936 \pm 0.0018 \qquad \langle \epsilon_{sf} \rangle = 0.9979 \pm .00091 \tag{4.2}$$

Errors in both quoted values are well within the range required by the experiment and the value $\langle \epsilon_{sf} \rangle$ can be removed from (4.1) since its value is so close to one.

4.1 Polarizing the Analyzer Cell

Techniques of NMR are vital for polarizing an analyzer cell for neutron polarimetry measurements during the n^{3}He experiment. An analyzer cell [28] can also be referred to as a spin filter or a Helium-3 cell. At room temperature the cell used for the n^{3}He experiment contains ^{3}He at about 1.3 atmospheres. It also contains a significant portion of Nitrogen gas (N_2) along with small amounts of the alkali metals Rubidium (Rb) and Potassim (K). This combination of elements allow the cell to be polarized using the technique of Spin Exchange Optical Pumping (SEOP).

To initiate optical pumping of the alkali metals, the cell is placed in a uniform magnetic field (holding field) of 10-12 Gauss and heated in a convection oven to 195 degrees celsius vaporizing both metals. Infra-red light from two high intensity lasers passes through 1/4-wave plates becoming circularly polarized before falling on the heated cell. The lasers emit a wide bandwith covering the D1 and D2 wavelengths of Rb and K given by

$$\begin{aligned} Rb \longrightarrow D1 : 795\,nm \qquad D2 : 780\,nm \\ K \longrightarrow D1 : 770\,nm \qquad D2 : 760\,nm \end{aligned}$$

and allowing for excitation of each alkali metals' valence electron. The energy level diagram in figure 4.1 borrowed from [28] shows the interaction of the polarized light with the alkali metals. The $S_{1/2}$ valence electrons contain $m_s = \pm 1/2$ substates at slightly different energies. The incident polarized light can only be absorbed by the $m_s = -1/2$ substate which briefly excites electrons into P-orbitals. This state can decay to either of the two $S_{1/2}$ substates but since the $m_s = -1/2$ state is being continuously pumped, the alkali vapor will have an excess of atoms characterized by

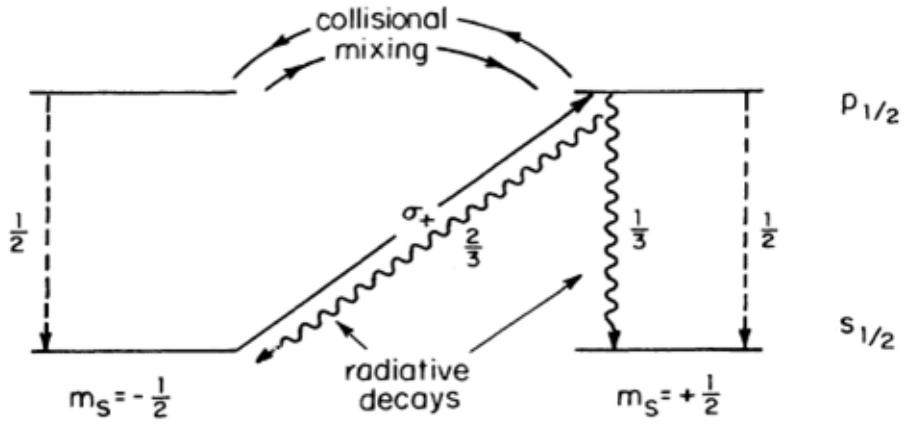

Figure 4.1: Schematic showing the polarization of an alkali metal (Rb or K) by optical pumping.

$m_s = 1/2$ and therefore a net polarization

$$P_A = \rho_A(+\tfrac{1}{2}) - \rho_A(-\tfrac{1}{2}) \tag{4.3}$$

where $\rho_A(\pm\frac{1}{2})$ are the occupation probabilities in each substate. Without N_2 gas in the cell the decay of the $P_{1/2}$ substate proceeds to each $S_{1/2}$ state with probabilities $(\frac{2}{3}, \frac{1}{3})$. On the other hand, a partial pressure of N_2 gas about one-tenth the partial pressure of ^{3}He will induce collisional mixing between the $P_{1/2}$ states leading to equal probability decays $(\frac{1}{2}, \frac{1}{2})$ to the $S_{1/2}$ states producing a higher alkali polarization.

The resulting polarized alkali vapor can then polarize the Helium gas during hyperfine spin exchange collisions between valence electrons and the ^{3}He nuclei. The spin exchange rate is given by γ_{SE} —a number proportional to the number density of the alkali vapor in the cell. It is a relatively small number which can be compared to the relaxation rate Γ of the polarized ^{3}He in the absence of optical pumping. When $\gamma_{SE} > \Gamma$, these two quantities determine the polarization P of the ^{3}He as function of

time

$$P(t) = \frac{\gamma_{SE} P_A}{\Gamma + \gamma_{SE}} \left[1 - e^{-(\Gamma+\gamma_{SE})t}\right] \tag{4.4}$$

In the special case of $\gamma_{SE} \gg \Gamma$ the maximum achievable polarization of the cell will be governed exclusively by the polarization of the alkali metal.

Free Induction Decay: Indirect measurements of cell polarization during optical pumping can be obtained using the NMR technique of Free Induction Decay (FID) [25, 26]. The technique uses a small coil of wire fastened to the top of the cell—and perpendicular to the direction of the holding field—which can receive a short duration input RF voltage at frequency ω_{in} displaced by approximately 100 Hz from the Larmor frequency of the ^{3}He nuclei. The Larmor frequency is easily calculated using the gyromagnetic ratio in equation (1.16) and an average holding field value of 12 gauss:

$$f_L = \gamma_{[3He]} B_o / 2\pi \sim 39\,\text{kHz} \tag{4.5}$$

The RF voltage on the coil gives a corresponding perturbing RF magnetic field B_{in} which causes the spins of the polarized ^{3}He nuclei to precess about the holding field at frequency

$$\omega_o = \omega_L - \omega_{in} \tag{4.6}$$

The FID signal returned on the coil is generated by the precessing magnetization induced in the cell from the original input signal and produces a measureable voltage in the coil given by

$$V(t) = V_o e^{-t/T_2} \cdot \sin\left(\omega_o t + \delta\right) \tag{4.7}$$

This is an underdamped oscillator having a decay time constant $T_2 \sim 55\,\text{ms}$ related to local variations of the magnetic holding field which tend to destroy the initial alignment of the precessing spins.

A pump rate graph from the pumping station is illustrated in figure 4.2 showing the initial amplitude of FID signals returned by the cell at two hour intervals over a time period of about 16 hours. The green curve shows clearly the trend to a saturation of the ^{3}He polarization over time. As a cautionary note the green curve should not be considered as a direct measurement of cell polarization since the technology is only marginally accurate.

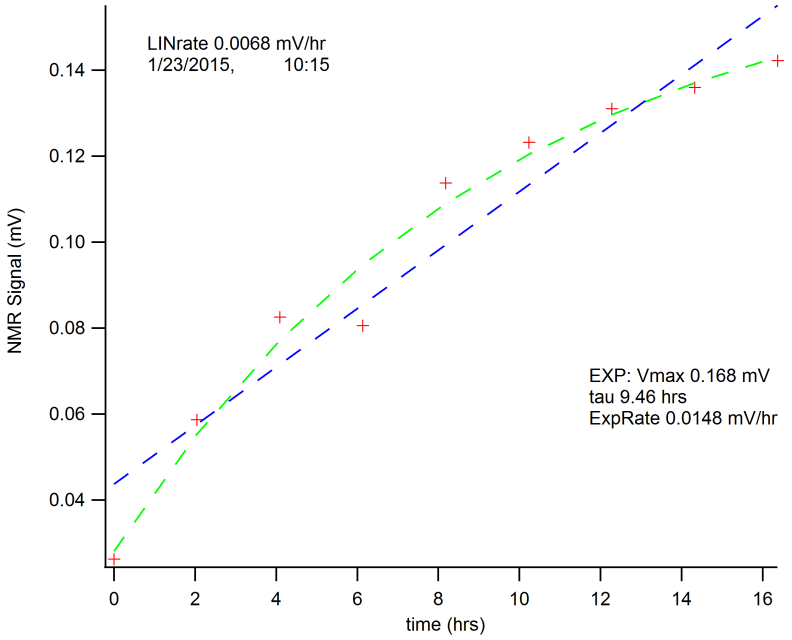

Figure 4.2: Curve fit by the Green dashed line indicative of polarization of the analyzer cell over a period of about 16 hours. Blue line is a linear fit provided by the FID software.

When saturation is reached the convection oven can be turned off allowing the cell to cool. If optical pumping is also terminatd the alkali metals in the analyzer cell will rapidly de-polarize causing a reduction in the ^{3}He polarization. For this reason it is important to continue optical pumping until the alkali vapor has re-condensed in the cell.

4.2 Properties of the Analyzer Cell

Following polarization of the cell a significant portion of the initial polarization can be maintained for a period of several days in a uniform holding field. This property, when coupled with the very strong spin-dependent capture cross section of the ^{3}He , make the analyzer cell ideal for performing polarimetry measurements on a beam of cold neutrons.

The capture cross-section for cold neutrons in the cell can be accurately modeled as a linear function of wavelength as long as the wavelengths are not too small:

$$\sigma(\lambda) \sim \frac{\sigma_o}{\lambda_o}\,\lambda \tag{4.8}$$

The ratio of the constants σ_o and λ_o represent an instrinsic property of the cell which determines its ability to capture neutrons. The cell used for the n^{3}He experiment may be referred to as 'Hedy Lamarr' which is discussed in [25, 26], and characterized by

$$\sigma_o = 5316\,\text{bn} \qquad\qquad \lambda_o = 1.798\,\text{Å} \tag{4.9}$$

Other important dimensions are its diameter $d = 7.5$ cm and its length $\ell = 10.3$ cm. The *Cell Thickness* is defined by the equation

$$\chi \equiv \frac{n\sigma_o\ell}{\lambda_o} \tag{4.10}$$

where n is the number density of atoms in the cell. Musgrave [26] determines the value $\chi = 1.004$ implying that Hedy Lamarr has a ^{3}He number density of $n \sim 3.396 \times 10^{25}$ atoms/m^3.

Transmission of Polarized Neutrons through an Analyzer Cell[19]: The initial neutron beam polarization $P_n(\lambda)$ is determined by the supermirror polarizer

and shows a slight dependence on wavelength. To determine the transmitted beam flux through the cell it us useful to construct the initial beam out of parallel and anti-parallel spin components. If the polarization of the cell is P, the transmission of each component through the cell is given by

$$T_{pa}(\lambda) = \tfrac{1}{2} T_o(\lambda) \left[1 + P_n\right] e^{-\chi\lambda(1-P)} \tag{4.11a}$$

$$T_{ap}(\lambda) = \tfrac{1}{2} T_o(\lambda) \left[1 - P_n\right] e^{-\chi\lambda(1+P)} \tag{4.11b}$$

and the total transmission through the cell can be written

$$T(\lambda) = T_{pa}(\lambda) + T_{ap}(\lambda) = T_o(\lambda) \cdot e^{-\chi\lambda} \left[\cosh(\chi\lambda P) + P_n \sinh(\chi\lambda P)\right] \tag{4.12}$$

The application of this formula is indicated in figure 4.3 for two consecutive SNS beam pulses. The first 49 time bins of the plot in blue show the transmission when P and $P_n(\lambda)$ are parallel giving a large transmission observed in the ion chamber. In contrast, the last 49 time bins show the transmitted beam after neutron spins have been flipped by the spin flipper. In this case $P_n(\lambda)$ in equation (4.12) inherits a minus sign. The plotted points in black show the transmission through the cell after it has been de-polarized. This corresponds to setting $P = 0$ in (4.12) leading to a simple expression for transmission through the unpolarized cell:

$$T(\lambda) = T_o(\lambda) \cdot e^{-\chi\lambda} \tag{4.13}$$

The transmission is now independent of the spin state of the beam which is clearly visible in the plot.

Since incident neutrons are arriving from a pulsed source, each time bin in the plot can also be associated with a neutron wavelength λ. This is a simple linear relationship which can be derived by noting that irregularities in the transmitted flux are caused by Bragg scattering in Aluminum at wavelengths $\lambda_1 = 4.05$ Å and $\lambda_2 = 4.68$ Å. The approximate formula determining wavelengths in Angstroms which

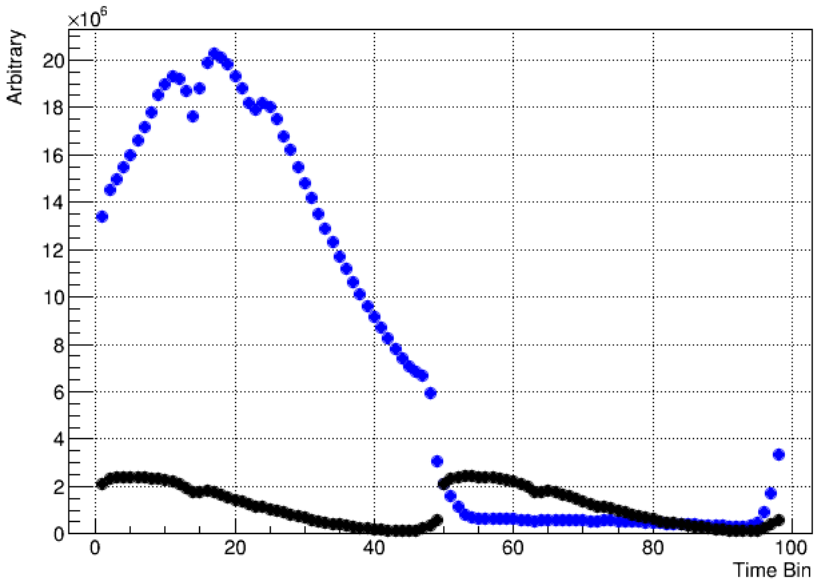

Figure 4.3: Transmission of two consecutive beam pulses through a ^{3}He cell. Blue plot corresponds to a cell polarization of 65%.

is used for all polarimetry measurements is given by

$$\lambda = \frac{h}{m_n d_o}\left[\frac{16.67}{49}t_b + t_o\right] \cdot 10^7 \tag{4.14}$$

where the time bin is labeled t_b in milli-seconds and where the two constants d_o and t_o must be inserted by hand. Values calculated from the Bragg edges are

$$d_o = 19.24\,\text{Å} \qquad t_o = 14.53\,\text{ms} \tag{4.15}$$

4.3 Polarimetry Apparatus and Setup

The apparatus used for polarimetry measurements [26] is shown in figure 4.4. The spin flipper sits to the left of the apparatus and will transmit both neutron spin states through the analyzer cell, which is mounted on a V-block at the beam centroid. A

set of Helmholtz coils is attached to the mount which serve to initiate AFP flips of the ^{3}He nuclei in the cell (See section 4.6).

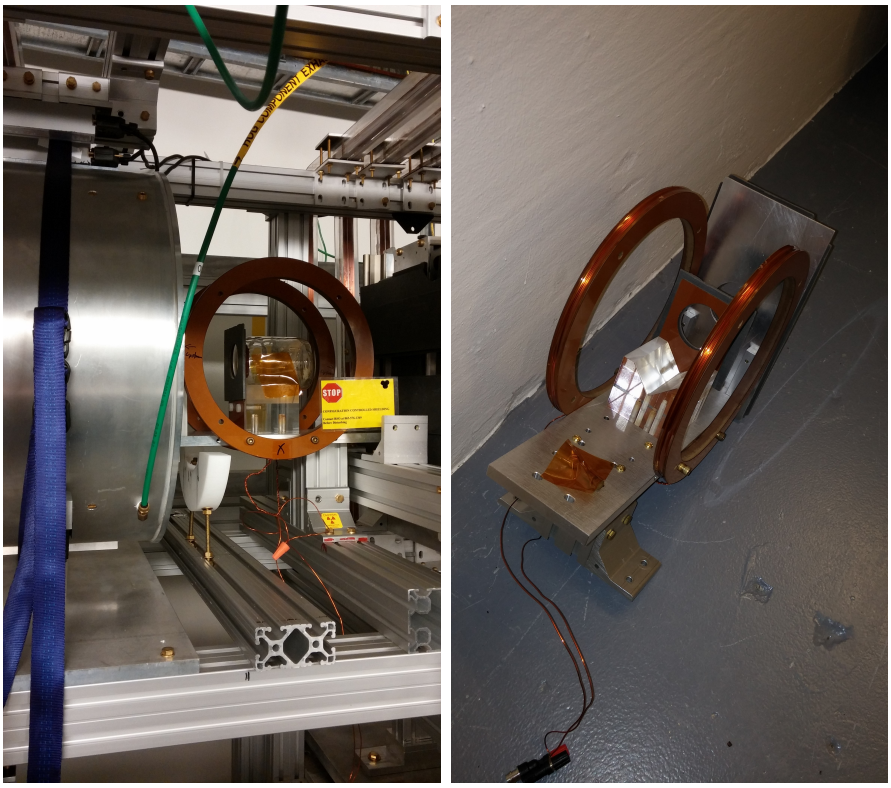

Figure 4.4: Polarimetry setup and AFP coils for polarimetry measurements on the beam and the spin flipper.

The four jaw collimator is visible in the first picture sitting downstream from the polarimetry apparatus and located directly in front of the ion chamber. During data production the collimator doors are set to transmit a beam 8.2 cm high and 10 cm wide. However, during polarimetry the doors must be reset to form a 3.5 cm $\times$ 3.5 cm square centered at the beam centroid along with the analyzer cell. This setting is necessary to ensure that the only neutrons entering the ion chamber are those which are transmitted through the analyzer cell. Neutrons outside the square are absorbed by the Li-6 on the collimator doors and would otherwise enter the ion chamber producing signal contamination.

The ion chamber (not shown in either picture but viewable in figure 2.7) sits downstream from the spin flipper, the analyzer cell, and the collimator and serves as the beam monitor during polarimetry. While the ion chamber contains 144 signal wires, it is only necessary to read signals on the DAQ computer from a single wire to perform necessary measurements required by polarimetry. The obvious choice is the central signal wire in the first wire plane labeled $(S, w) = (1, 5)$.

4.4 Optimizing Spin Flipper Efficiency

The efficiency of the spin flipper is determined by the solution to the two-state problem of Spin Magnetic Resonance (covered in chapter 3) which identifies the probability P at time t that a neutron beginning in a spin-up state transitions to a spin-down state. If the spin flipper is being driven at frequency ω_{rf} this probability is given by the Rabi formula

$$P(t) = \frac{4\omega_F^2}{4\omega_F^2 + (\omega_L - \omega_{rf})^2} \sin^2 \left[\sqrt{\omega_F^2 + \frac{(\omega_L - \omega_{rf})^2}{4}}\, t \right] \tag{4.16}$$

where ω_L is the Larmor frequency of the neutrons and the quantity ω_F is proportional to the amplitude of the driving RF field. For a given neutron wavelength, the value of t can be associated with the time spent by those neutrons in the spin flipper and $P(t)$ can be equated to the spin flipper efficiency ϵ_{sf}. Maximizing the efficiency is an essential requirement to be measured experimentally with neutron polarimetry.

An important quantity needed to measure spin flipper efficiency is the spin flip ratio $\mathcal{Q}(\lambda)$. The value of $\mathcal{Q}(\lambda)$ is the ratio of the transmitted signal through the analyzer cell from the polarized beam before and after the polarization of the beam is reversed by the spin flipper. Call these transmissions T_{off} and T_{on} which follow

from equation (4.12) as

$$T_{off} = T_o(\lambda) \cdot e^{-\chi\lambda} \left[\cosh(\chi\lambda P) + P_n(\lambda) \sinh(\chi\lambda P)\right] \tag{4.17a}$$

$$T_{on} = T_o(\lambda) \cdot e^{-\chi\lambda} \left[\cosh(\chi\lambda P) + \alpha P_n(\lambda) \sinh(\chi\lambda P)\right] \tag{4.17b}$$

where $\alpha = 1 - 2\epsilon_{sf}$. The spin flip ratio is then

$$\mathcal{Q}(\lambda) \equiv \frac{1 + P_n(\lambda) \tanh(\chi\lambda P)}{1 + \alpha P_n(\lambda) \tanh(\chi\lambda P)} \tag{4.18}$$

A useful approximation to $\mathcal{Q}(\lambda)$, which works well for the cold neutron wavelengths provided to FnPB, follows by considering large values inside the arguments of the hyperbolic tangents for which

$$\mathcal{Q}(\lambda) \longrightarrow \frac{1 + P_n(\lambda)}{1 + \alpha P_n(\lambda)} \tag{4.19}$$

For a spin flipper efficiency approaching 1 and a beam polarization of 95% this number has a value of about 35-40 for a given wavelength. Experimental plots of $\mathcal{Q}(\lambda)$ are illustrated in figure 4.5 at four different magnetic field settings near resonance.

4.4.1 Tuning Prior to Data Production

The n^3He experiment cannot begin data production until spin flipper efficiency has been optimally set. In general, this will occur when the value of the guide field and the spin flipper RF voltage are both tuned to precise values.

Tuning the Guide Field: Let $\langle\mathcal{Q}\rangle$ be the average value of $\mathcal{Q}(\lambda)$ for all wavelengths (or time bins). An approximate formula for $\langle\mathcal{Q}\rangle$ as a function of the guide field B_o can be derived by considering variations of the neutron Larmor frequency $\omega_L = \gamma_n B_o$ near the resonance associated with equation (4.16). In that case the argument of the

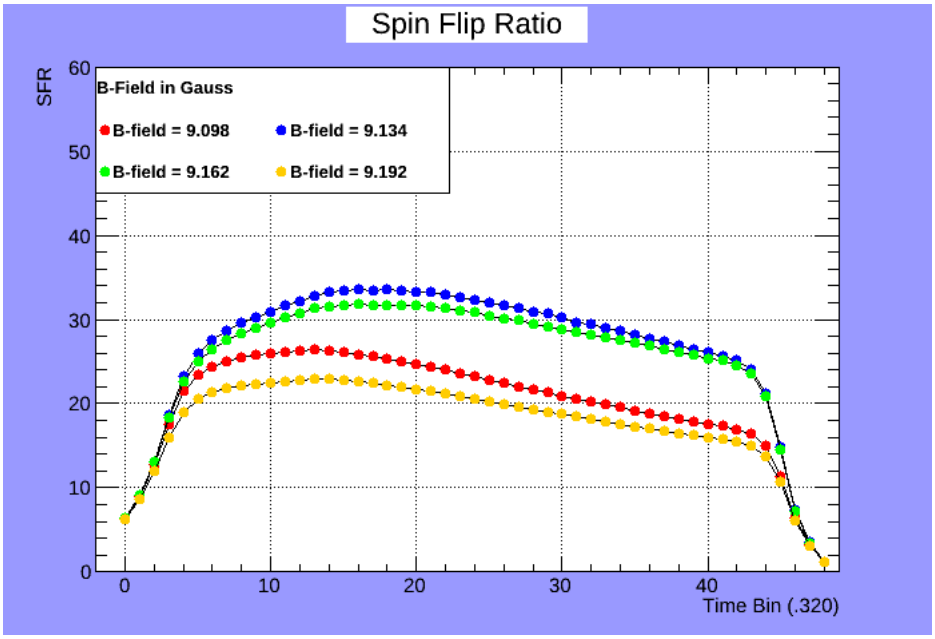

Figure 4.5: Plots of $\mathcal{Q}(\lambda)$ drawn from 49 times bins available on the DAQ computer.

sine function is approximately 1 and the spin flipper efficiency can be written

$$\epsilon_{sf}(\omega_L) \sim \frac{4\omega_F^2}{4\omega_F^2 + (\omega_L - \omega_{rf})^2} \tag{4.20}$$

Inserting $\epsilon_{sf}(\omega_L)$ into (4.19) results in the formula

$$\langle \mathcal{Q}(B_o) \rangle = \frac{4\omega_F^2 + (\gamma_n B_o - \omega_{rf})^2}{4y_n\omega_F^2 + (\gamma_n B_o - \omega_{rf})^2} \tag{4.21}$$

where

$$y_n = \frac{1 - \langle P_n \rangle}{1 + \langle P_n \rangle} \tag{4.22}$$

determines both the width and the height of the resonance peak. A value of ω_{rf} is available from equation (3.73). Using a constant $\langle P_n \rangle \sim 0.95$ over all wavelengths and an effective $\omega_F = 3,312$ rads/sec will generate the green curve of figure 4.6 in good agreement with plotted (brown) points from initial polarimetry on 01-28-2015. From equation (3.68), this corresponds to an average wavelength $\lambda \sim 4.75$Å. The extension

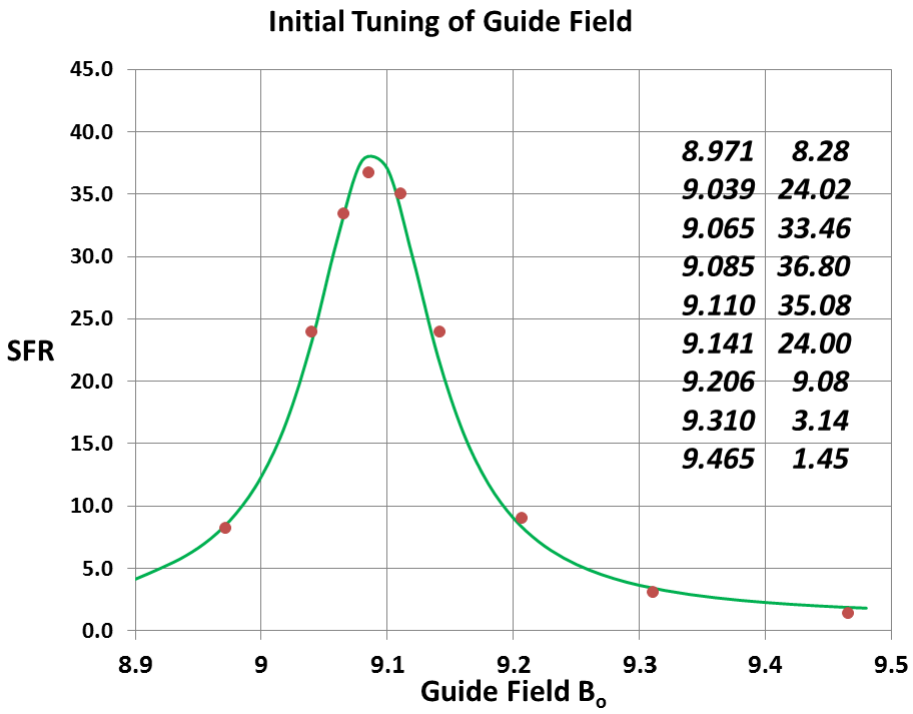

Figure 4.6: Plot of $\langle \mathcal{Q} \rangle$ versus B_o.

of this approximation to cover each wavelength individually is more difficult but would presumably eliminate the need to insert a value for ω_F by hand.

Tuning the RF Voltage: The guide field is set when $\omega_L \to \omega_{rf}$ and the term multiplying the sine function in equation (4.16) is very close to 1. However, the argument of the sine can still vary with RF field provided by the spin flipper since ω_F is proportional to this field. In this case, the spin flipper efficiency can be written

$$\epsilon_{sf} \sim \sin^2(\omega_F t) \tag{4.23}$$

Inserting this equation into (4.19) and taking averages shows that the inverse of $\langle \mathcal{Q} \rangle$ will be given by

$$\langle \mathcal{Q} \rangle^{-1} = 1 - \frac{2\langle P_n \rangle}{1 + \langle P_n \rangle} \sin^2 \omega_F t \tag{4.24}$$

For values of $\langle P_n \rangle$ close to 1 this equation can also be written

$$\langle \mathcal{Q} \rangle^{-1} = \cos^2 \omega_F t + y_n \sin^2 \omega_F t \tag{4.25}$$

Maximizing the spin flip ratio will occur when the right side of this equation is minimized. This happens when

$$\omega_F t = m\pi/2 \qquad \text{for} \qquad m = 1, 3, 5.... \tag{4.26}$$

so that $\langle \mathcal{Q} \rangle$ is given by

$$\langle \mathcal{Q} \rangle = \frac{1 + \langle P_n \rangle}{1 - \langle P_n \rangle} \tag{4.27}$$

The value of ω_F is ultimately determined by the RF-voltage supplied to the spin flipper which determines its internal field B_{rf}. If this voltage supply is unlimited, then any number of RF-voltages will optimize the operational efficiency of the spin flipper. However, larger voltages also mean larger RF magnetic fields which increases the possibility of interference with other critical components of the experiment. For this reason alone, it is convenient to choose the lowest value of m. A plot showing the first complete oscillation is illustrated in figure 4.7 from 01-28-2015 polarimetry. An analysis of the data points indicate a very precise correlation to equation (4.25). The value of the minimum can be regarded as a measurement of the average beam polarization determined from the equation

$$\langle P_n \rangle = \frac{1 - \langle \mathcal{Q} \rangle^{-1}}{1 + \langle \mathcal{Q} \rangle^{-1}} \tag{4.28}$$

4.4.2 Tuning During Data Production

Two magnetometers installed near the spin flipper monitor the guide field B_o during data production and show that B_o can drift over time with sudden changes as large as 50 mG. These changes are less than one percent of the value of the guide field but have a measurable impact on the spin flipper efficiency since the Larmor frequency

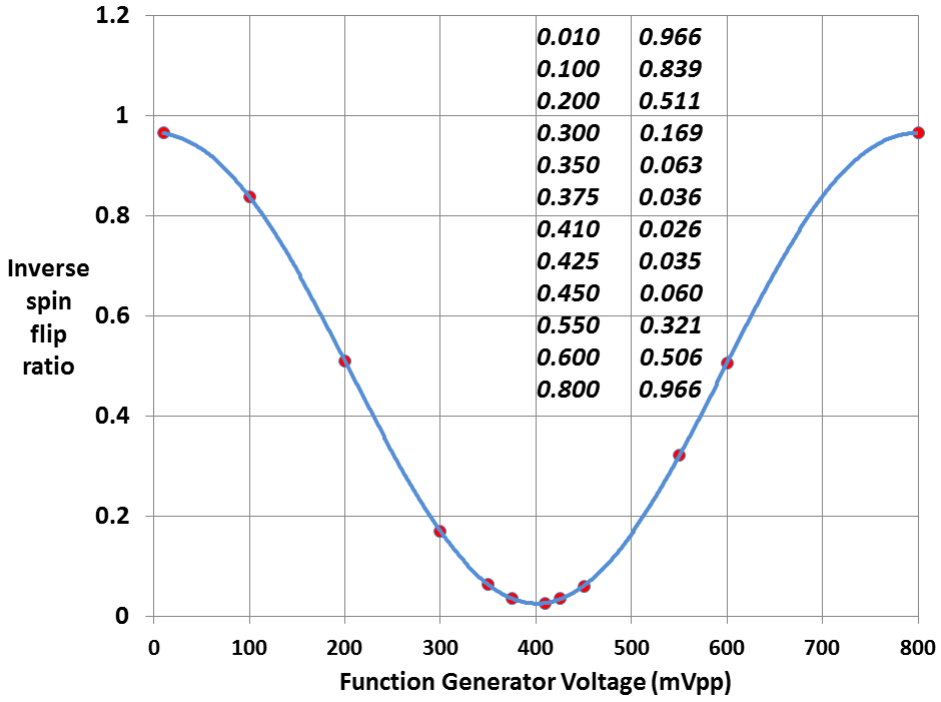

Figure 4.7: Plot of $\langle \mathcal{Q} \rangle^{-1}$ versus RF voltage on the AWG-3022B function generator. The minimum near 400 mV is indicative of maximum spin flipper efficiency. Maximum values less than 1 can be attributed to departures of the guide field from resonance.

ω_L of the neutrons changes with the guide field. The mechanism for guide field drifts can be attributed to components at the SNS external to the n^{3}He experiment. As an example, field measurements in the presence of the moving 30 ton overhead crane show contributions on the order of 10 mG. Regardless of the source however, it is clearly important during polarimetry measurements to ensure that ϵ_{sf} remains maxmimized. During data production a plot of $\langle \mathcal{Q}(B_o) \rangle$ covering a large range of possible guide field values like figure 4.6 is not necessary. Instead, it is more reasonable to make measurements using values of B_o slightly off-resonance. A least-squares fit to the curve as in figure 4.8 then determines a single optimal value for B_o which can be set by the guide field power supplies. The optimization curve for small variations of B_o

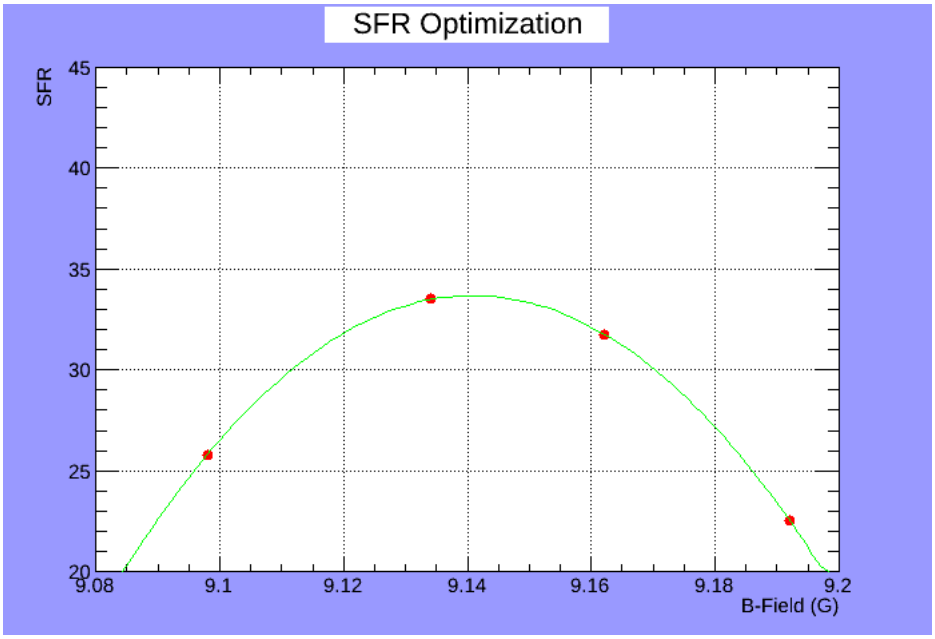

Figure 4.8: $\langle \mathcal{Q} \rangle$ plotted against small variations of the guide field. Compare with figure 4.6.

is approximately inverse-parabolic and can be modeled as

$$\langle \mathcal{Q} \rangle = \langle \mathcal{Q} \rangle_{max} - C \cdot (B - B_o)^2 \tag{4.29}$$

where B is the tunable field variable and C is a large constant having a value of approximately $500 - 1000\, G^{-2}$.

The RF magnetic field can also be tuned during data production. Unlike the guide field though the value of B_{rf} is not expected to drift over time making measurements unneccessary. Nevertheless, an optimization plot for several relatively small variations of voltage settings on the AWG-3022B is shown in figure 4.9: The curve exhibits a very wide maximum indicating a wide tolerance in the magnitude B_{rf} for effective spin flipper operation.

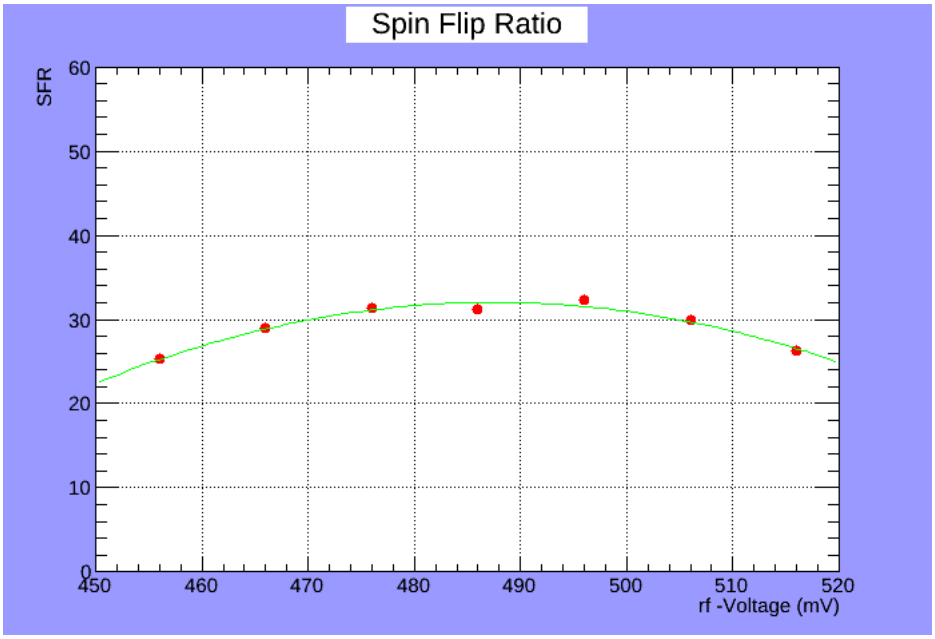

Figure 4.9: Plot of $\langle \mathcal{Q} \rangle$ versus RF signal amplitude applied to the spin flipper.

4.5 Neutron Beam Polarization

The polarization $P_n(\lambda)$ of the neutron beam [29] can be determined from independent measurements with a polarized cell and an unpolarized cell. The transmission through an unpolarized cell has already been determined to be

$$T_{unp} = T_o(\lambda) \cdot e^{-\chi\lambda} \tag{4.30}$$

The spin flipper can be on or off here since the transmission through the cell favors no direction of the incoming spins. Now suppose transmission measurements are made through a polarized cell with the spin flipper on and off. Refer to these transmissions as T_{on} and T_{off}, and define relative transmission coefficients R_1 and R_2 by

$$R_1 \equiv \frac{T_{on}}{T_{unp}} \qquad\qquad R_2 \equiv \frac{T_{off}}{T_{unp}} \tag{4.31}$$

For a polarized beam incident on a polarized cell, the total transmission through the cell is given by equation 4.12. If the polarization is reversed by the spin flipper having an efficiency ϵ_{sf}, then the values of R_1 and R_2 will be

$$R_1 = \cosh(\chi\lambda P) + P_n \sinh(\chi\lambda P) \tag{4.32a}$$

$$R_2 = \cosh(\chi\lambda P) + \alpha P_n \sinh(\chi\lambda P) \tag{4.32b}$$

where $\alpha = 1 - 2\epsilon_{sf}$. Solving for $\cosh(\chi\lambda P)$ in terms of R_1 and R_2 leads to

$$\cosh(\chi\lambda P) = \frac{R_2 - \alpha R_1}{1 - \alpha} \tag{4.33}$$

Now solve equation 4.32a for P_n

$$P_n = \frac{R_1 - \cosh(\chi\lambda P)}{\sinh \chi\lambda p} \tag{4.34}$$

and insert equation 4.33 to determine the formula by which the polarization of the neutron beam can be determined. One finds

$$\boxed{P_n(\lambda) = \frac{R_1 - R_2}{\sqrt{[R_2 - (1 - 2\epsilon_{sf})R_1]^2 - 4\epsilon_{sf}^2}}} \tag{4.35}$$

It is important to observe here that polarization values get smaller as the value of ϵ_{sf} is increased near the value of 1. An approximate formula can be determined in the form

$$P_n = -m\epsilon_{sf} + b \tag{4.36}$$

This means that the effect of assuming an ideal spin flipper efficiency in the calculation of beam polarization is to give a result which is somewhat smaller than it actually is. Based on the large value of the spin flipper efficiency anyway, it is appropriate to

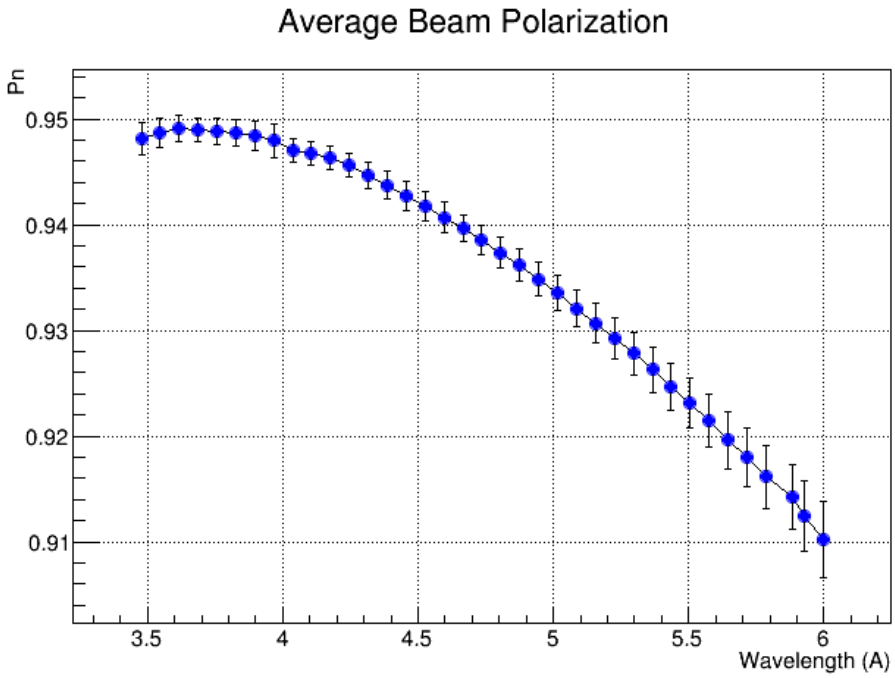

Figure 4.10: Average neutron beam polarization determined from 8 polarimetry measurements.

neglect small corrections to (4.35) and write

$$P_n(\lambda) = \frac{R_1 - R_2}{\sqrt{[R_2 + R_1]^2 - 4}} \tag{4.37}$$

The experimental average polarization curve is illustrated in figure 4.10 which is determined from eight independent measurements during the period February to November 2015. Only wavelengths in the range $3.48\,\text{Å} < \lambda < 5.99\,\text{Å}$ are used for the calculation and the data for the plot is summarized in Table A.4 of the Appendix. The small slope in the curve is attributed to the supermirror polarizer.

4.6 Spin Flipper Efficiency

A measurement of the spin flipper efficiency during neutron polarimetry requires the ability to implement a near one-hundred percent reversal of the ^{3}He nuclear magnetic

moments inside the analyzer cell. This can be achieved through the NMR technique of Adiabatic Fast Passage (AFP).

Adiabatic Fast Passage: A set of Helmholtz coils placed around the analyzer cell is shown in the right photograph of figure 4.4. A minimum diameter of the coils is needed to ensure that the magnetic field it produces is uniform over the entire volume occupied by the cell. During polarimetry, the magnetization $\boldsymbol{M}$ of the cell can be inverted by applying an RF pulse to the coils, perpendicular to the direction of the guide field, and executing a linear sweep across the Larmor frequency of the ^{3}He nuclei.

The mechanism by which the magnetic moments are flipped is best understood by inspection of the graphic in figure 4.11 showing the rotation $\theta(t)$ of an effective field $\boldsymbol{B}_{eff}$ viewed in the frame of the rotating ^{3}He spins and given by

$$\boldsymbol{B}_{eff} = (B_o - \omega(t)/\gamma)\,\hat{\boldsymbol{y}} + B_{afp}\,\hat{\boldsymbol{x}} \tag{4.38}$$

The magnetic moments $\boldsymbol{\mu}$ precess about this vector as its y-component changes sign thereby reversing the direction of $\boldsymbol{M}$. The linear sweep covers a frequency range of 20–60 kHz in 2 seconds. This time is appropriately chosen so that the time spent by the individual $\boldsymbol{\mu}$ near the Larmor frequency is short compared to their relaxation time. The efficiency of AFP flips documented in [26] is about 98% which should also apply here since both experiments use the same instrumentaton.

Calculation of Spin Flipper Efficiency: The experimental spin flipper efficiency $\epsilon_{sf}(\lambda)$ can be calculated based on transmission measurements of the polarized neutron beam through a polarized ^{3}He cell having spins which can be flipped by AFP. If the spin flipper is initially off, the total transmission through the cell with polarizations

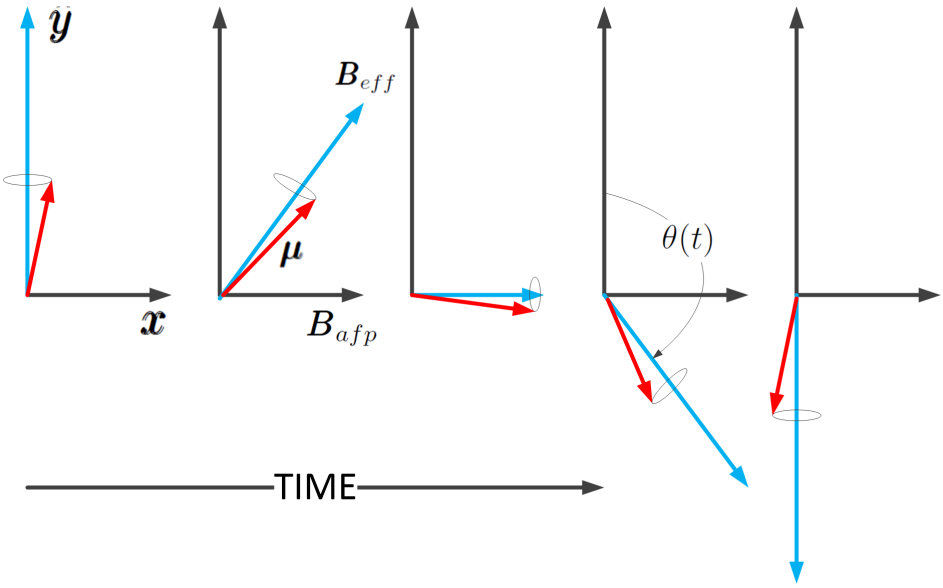

Figure 4.11: A magnetic moment $\boldsymbol{\mu}$ of a ^{3}He nuclei shown in red getting dragged across the x-z plane as it precesses about $\boldsymbol{B}_{eff}$ shown in blue.

P and $-P$ is

$$T = T_o(\lambda)e^{-\chi\lambda}\left[\cosh(\chi\lambda P) + P_n \sinh(\chi\lambda P)\right] \tag{4.39a}$$

$$T_{afp} = T_o(\lambda)e^{-\chi\lambda}\left[\cosh(\chi\lambda P) - P_n \sinh(\chi\lambda P)\right] \tag{4.39b}$$

which determines the polarization quantity

$$P_{off} = \frac{T - T_{afp}}{T + T_{afp}} = P_n \tanh(\chi\lambda P) \tag{4.40}$$

If the procedure is repeated with the spin flipper turned on, equations (4.39) are modified to read:

$$T = T_o(\lambda)e^{-\chi\lambda}\left[\cosh(\chi\lambda P) + \alpha P_n \sinh(\chi\lambda P)\right] \tag{4.41a}$$

$$T_{afp} = T_o(\lambda)e^{-\chi\lambda}\left[\cosh(\chi\lambda P) - \alpha P_n \sinh(\chi\lambda P)\right] \tag{4.41b}$$

and a new polarization quantity is

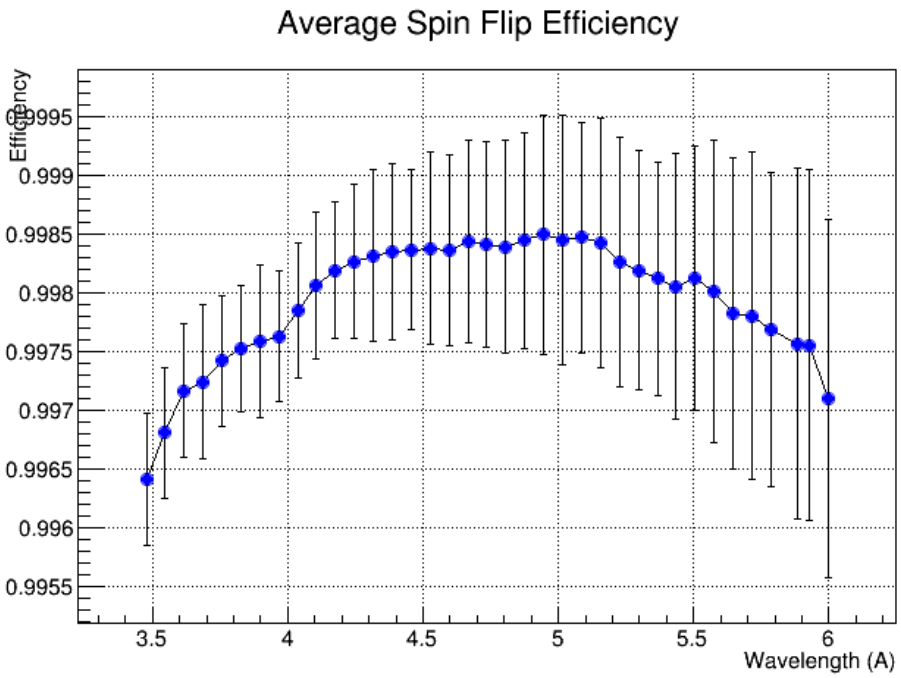

Figure 4.12: Plot of Average spin flipper efficiency determined from polarimetry measurements and AFP coils.

$$P_{on} = \frac{T - T_{afp}}{T + T_{afp}} = \alpha P_n \tanh(\chi \lambda P) \tag{4.42}$$

The two values P_{off} and P_{on} are determined from measurable quantities produced by the beam monitor, and they are easily shown to determine the spin flipper efficiency from

$$\epsilon_{sf} = \frac{1}{2}\left[1 - \frac{P_{on}}{P_{off}}\right] \tag{4.43}$$

This calculation initially assumes that the action of the AFP flip does not de-polarize the beam; But realistically, each AFP flip produces a small cell de-polarization on the order of a few percent. An easy way to get around this is to perform transmission measurements using an extra AFP flip back to the initial polarization of the cell. One can then average the initial transmission with the transmission following two AFP flips. A formula for the emerging beam polarization with the spin flipper on or off

will then modified slightly to read

$$P_{on/off} = \frac{\bar{T} - T_{afp}}{\bar{T} + T_{afp}} \tag{4.44}$$

4.7 Cell Polarization

The value of the cell polarization [25, 26] is not needed to perform measurements of beam polarization and spin flipper efficiency. Nevertheless, cell polarization was determined as an integral part of polarimetry—mainly because of its importance as a diagnostic tool but also because data required to determine cell polarization and beam polarization are identical.

Cell polarization can be determined by comparing independent transmissions of an unpolarized beam through a polarized cell and then through an unpolarized cell. For an unpolarized cell the transmission is given by

$$T_{unp}(\lambda) = T_o(\lambda)e^{-\chi\lambda} \tag{4.45}$$

and if the cell has a polarization P this formula has been shown to generalize to

$$T_{pol}(\lambda) = T_o(\lambda)e^{-\chi\lambda}\cosh\chi\lambda P = T_{unp}(\lambda)\cosh\chi\lambda P \tag{4.46}$$

Solving for the polarization yields

$$P = \frac{1}{\chi\lambda}\cosh^{-1}\left[\frac{T_{pol}(\lambda)}{T_{unp}(\lambda)}\right] \tag{4.47}$$

The n^3He experiment uses only polarized neutron beams, so the quantities T_{pol} and T_{unp} must be approximated using intermittent spin flipped neutrons which can be averaged over a data run. These averaged values can then be inserted into (4.47) to give a useful result. A plot of cell polarization is shown in figure 4.13. From a theoretical point of view, the polarization of the cell cannot be a function of the

neutron wavelengths in the beam. This is generally true from an inspection of the plot however a small 1-2% positive or negative slope is typically observed and attributed to systematic effects. Ultimately, the degree to which the cell can be polarized depends

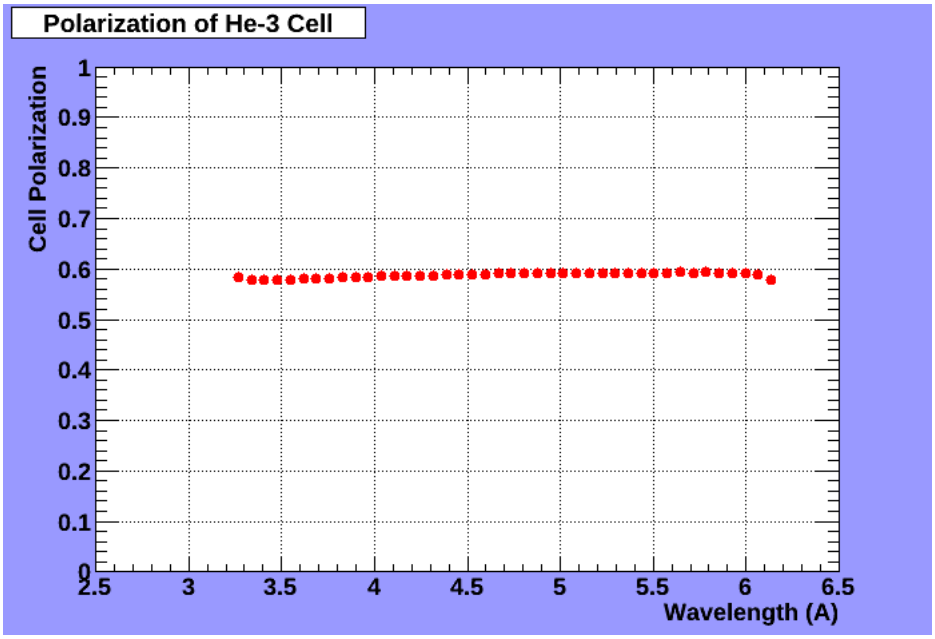

Figure 4.13: Plot from 5-20-2015 polarimetry indicating a cell polarization of about 60 percent over the wavelength range 3.5Å— 6.0Å.

on the quality of the infrared lasers and other equipment at the optical pumping station. Average values ranged from about 60-70% over the length of the experiment.

4.8 Polarimetry Measurements Off-Axis

Polarimetry measurements are typically performed by placing the analyzer cell at the centroid of the beam. However, the cross-sectional area of the cell is roughly 1/9 the size of the beam so it is possible to place the cell off-axis and perform polarimetry measurements which sample other parts of the beam. Off-axis measurements are important for two reasons: First, beam polarization is not constant over the cross-section of beam so that an off-axis measurement is expected to show a somewhat different polarization spectrum. Second, although the efficiency of the spin flipper is

expected to be constant over all parts of the beam, it is important to verify this with off-axis measurements.

The culmination of two off-axis measurements of beam polarization and spin flipper efficiency taken on 06-23-2015 are shown in figure 4.14. Plotted points in black were obtained by placing the cell 3.5 cm up from beam centroid. Likewise, plotted points in red were obtained by placing the cell 3.5 cm beam left. For reference, on-axis plotted points shown in blue were taken from polarimetry results of 5-20-2015.

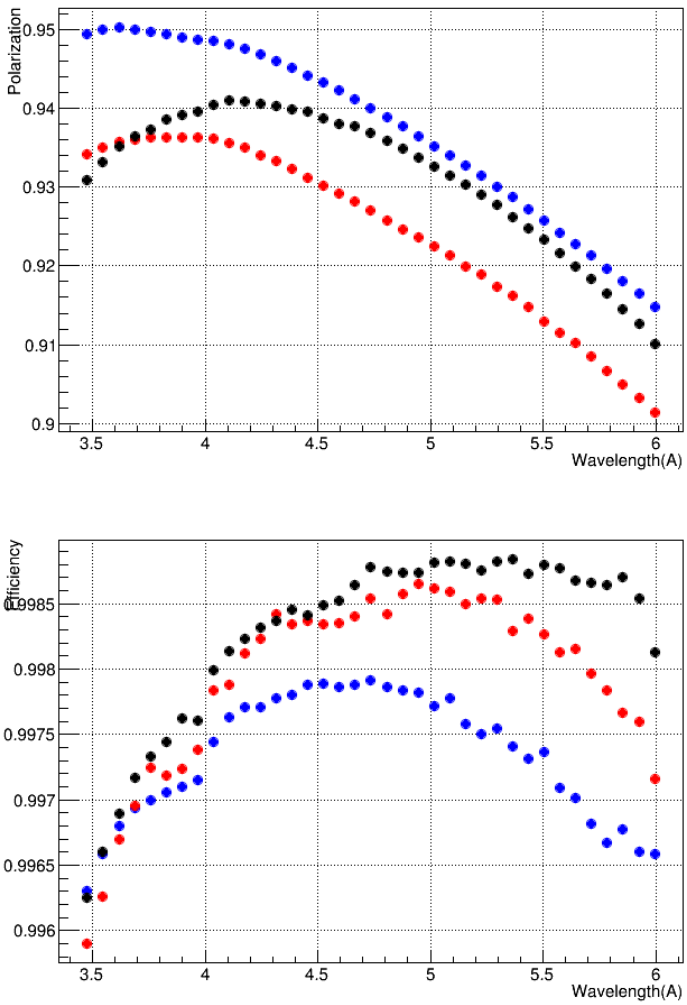

Figure 4.14: Off-axis measurements of beam polarization and spin flipper efficiency. Black: 3.5 cm beam-up. Red: 3.5 cm beam-left. Blue: Beam-Center.

A reduction of beam polarization over all wavelengths by about 1.5% is evident from the beam left data while a smaller change (with a change in shape for larger wavelengths) is indicated from the beam up data. In contrast, the spin flipper efficiency plots show only insignificant changes in the calculated efficiency using off-axis positioning of the analyzer. For example, a calculation of the percent change in ϵ_{sf} for each analyzer location averaged over each wavelength is

$$\Delta\epsilon_{sf}(Left) = 0.0638\,\% \qquad \Delta\epsilon_{sf}(Up) = 0.0932\,\% \tag{4.48}$$

Possible bias exists in the off-axis measurements since all polarimetry results for the n^{3}He experiment use the ion chamber as the beam monitor. Any of several signal wires near the front of the ion chamber can be used to extract signal voltages, and the single best choice for on-axis measurements is the central wire labeled (1,5) in the first wire plane. This same wire is used for beam left measurements but a shift upward by 3.5 cm required voltage readings from wire (2,7)* which is situated 3.8 cm above the central wire and 1.9 cm further into the ion chamber. Attempts at using wire (1,5) produce non-sensical results.

4.9 Comparison with NPDGamma Measurements

Beam polarization measurements at FnPB have also been reported by Musgrave [26] for the NPDGamma experiment. Both experiments receive neutrons from the same neutron guide and the same supermirror polarizer allowing for the possiblity of a credible comparison. However, many of the NPDGamma measurements were taken in the presence of para-hydrogen, aluminum, and chlorine targets which may not be useful for comparison. Instead, it is more practical to consider only the beam-center (BC) and beam-Left (BL) measurements in Table A.6 of Musgraves' paper which were taken in the absence of a target. The beam-center data are compared with the

*Ideally, one would like to use wire (1,7) for this measurement but this was a dead wire in the ion chamber and not used in the experiment.

n^3He beam average plot of figure 4.10 while the beam-left data are compared with the n^3He beam-left plot in figure 4.14. For convenience all four plots are shown in figure

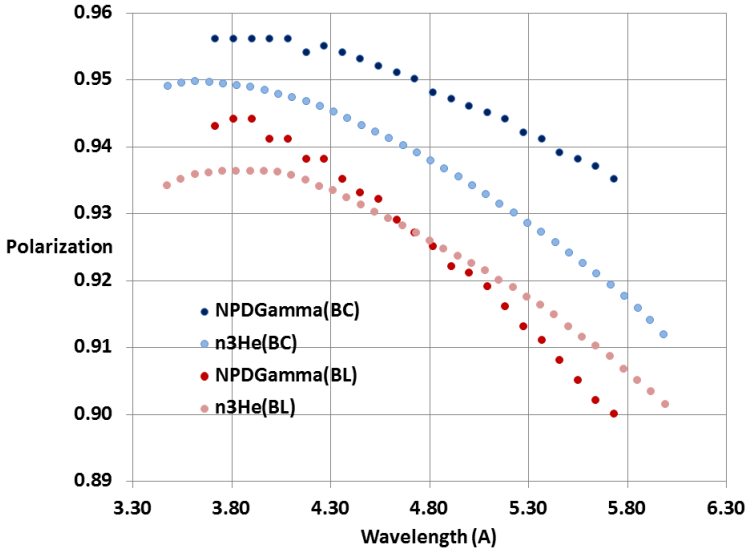

Figure 4.15: Beam polarization $P_n(\lambda)$ determined by n^3He and NPDGamma experiments at beam-center and beam-left.

4.15 for comparison. Since the measured wavelength spectrum of each experiment is different the individual points defining each curve cannot be directly compared.

There are several important factors which may contribute to the small $\sim$ 1% discrepancies revealed by both the beam-center and beam-left plots. While all polarimetry for the NPDGamma experiment utilized the M4 beam monitor to assess cell transmissions, measurements for n^3He experiment relied on the central wire (1,5) at the front of the ion chamber. Actual systematic effects caused by different equipment are speculative but could be due to differences in gas pressures and mixtures enclosed by each device. The NPDGamma polarimetry measurements were also performed close to 2 meters downstream from the n^3He measurements, although no attempt will be made to establish why a downstream measurement would render a different result. Finally, it can also be suggested that different spin flippers used for the two experiments might contribute to measured differences but this would not

be important for beam-center measurements where the efficiency of both devices are comparable.

Having outlined several possibilities, the most probable source of error can be traced to the fact that backgrounds in the two experiments were very different. For example, section 4.10 shows 120 Hz noise in the ion chamber not reported in the NPDGamma experiment. An effective method to probe the discrepancy might be a new set of polarimetry measurements using the M4 monitor and the n^{3}He spin flipper.

4.10 Signal Background

As previously indicated, the central wire in the first wire plane of the ion chamber is used for all polarimetry measurements—except those above beam center. All polarimetry calculations require the removal of the signal background recorded by this wire on the DAQ computer. The background is determined by closing the secondary shutter and performing a data run while the experiment is re-configured for polarimetry. The plot in figure 4.16 illustrates a typical background measured at

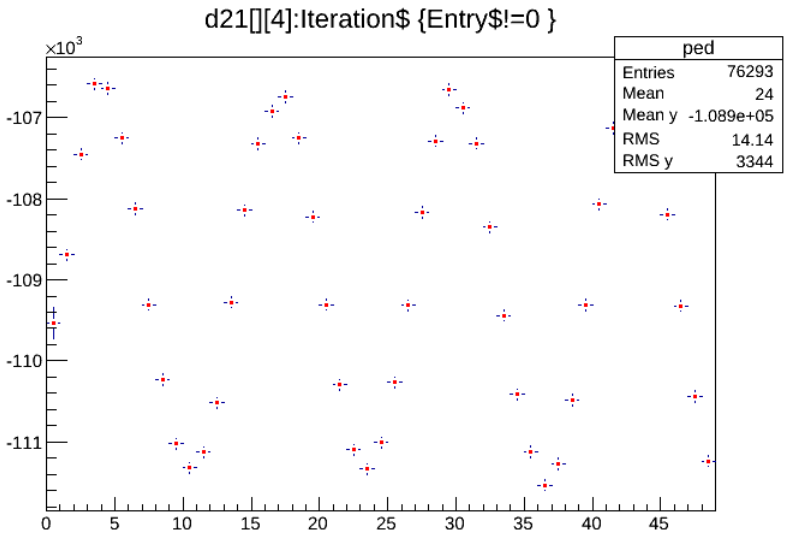

Figure 4.16: Background signal read by wire 21-4 versus wavelength during polarimetry on 11-30-2015.

each of the 49 time bins. In general, the signal is composed of a DC bias with 120 Hz noise superimposed—this is true for all wires in the ion chamber.

The average background amplitude can also be compared with the average signal received when the analyzer cell is in place and the shutter is open. Table 4.1 indicates that the presence of the cell and collimator severely limit the neutron flux to the point where the magnitude of the transmission of anti-parallel spins through the cell is only about 5 times the signal background.

Table 4.1: Table showing the signal background on wire (1,5) compared to signal received from parallel and anti-parallel neutron spins travelling through the analyzer cell during polarimetry.

Date	Background	Parallel spins	Anti-parallel spins
3-25-2015	-1.126E05	1.426E07	5.113E05
5-20-2015	-1.124E05	1.508E07	6.852E05
9-23-2015	-1.182E05	8.991E06	4.350E05
11-30-2015	-1.089E05	1.281E07	5.288E05

Another important statistic is to assess the variability of the background on wire (1,5) during polarimetry measurements performed over the course of the experiment. Table A.5 has been included showing the value of the signal averaged over eleven independent measurements of at each wavelength. The calculated values of the variance is a strong indicator that the background is relatively unchanging.

Chapter 5

Ion Chamber Profile and Simulation

A simulation of ion chamber yield is an important component of the n^{3}He experiment enabling the calculation of geometric factors and correlation coefficients necessary for the determination of the physics asymmetry A_p from the raw data. If A_p is to be measured to a precision of $\sim 10^{-8}$ with an uncertainty of a few percent, then a useful simulation should re-produce the actual measured yield in each of the 144 signal wires with approximately the same uncertainty. Before the simulation can be programmed however, it is necessary to have an understanding of how the interaction of equation (1.1) generates electrical current in the wires. In addition, it will be beneficial to have a full assessment of the yield profile recorded by the DAQ computer.

5.1 Yield from Ionization Tracks

The yield recorded on each of 144 signal wires in the target chamber results from ionization tracks left by the decay protons and tritons. Production of ions is a complicated function of the energy of the decay particles and can be characterized by

the stopping power, or loss of particle energy per unit path length

$$S(E) = -\frac{dE}{dx} \tag{5.1}$$

If the stopping power is known the mean range of the particle can be determined from

$$R = \int_0^{E_o} \frac{dE}{S(E)} \tag{5.2}$$

Range tables and stopping power tables for the proton in gaseous He is available from the National Institute of Standards and Technology (NIST) and is provided by the website nist.gov/pml/data/star/index.cfm. With corrections made for approximately 0.5 atmospheres of pressure in the ion chamber, ranges for both particles can be determined by inputing their initial decay energies leading to

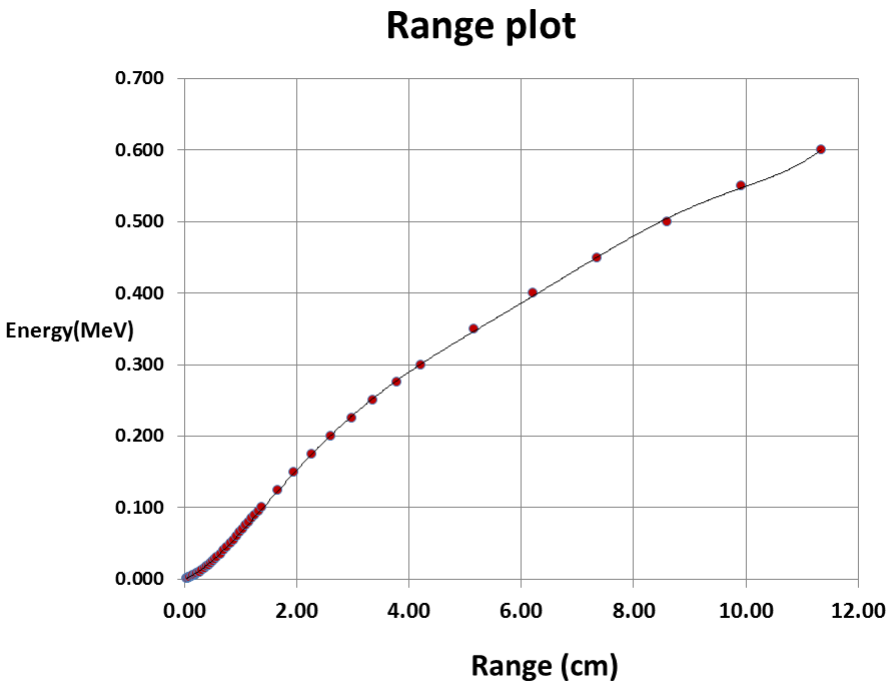

Figure 5.1: Plot of energy vs range for the proton at 1/2 atm.

$$R_p = 10.65\,\text{cm} \qquad R_T = 2.48\,\text{cm} \tag{5.3}$$

A plot of proton energy versus range constructed from the range tables is shown in figure 5.1. The plot is accurately approximated from a least-squares solution as a 6th order polynomial

$$\begin{aligned} E(r) = {} & 0.00000588 \cdot r^6 - 0.00020850 \cdot r^5 + 0.00280706 \cdot r^4 \\ & - 0.01759955 \cdot r^3 + 0.04719794 \cdot r^2 + 0.03291656 \cdot r \end{aligned} \tag{5.4}$$

This function will be useful for the development of the simulation since the quantity

$$E(r_2) - E(r_1) \tag{5.5}$$

is proportional to the ionization energy produced by either decay particle over the distance $\Delta r = r_2 - r_1$. A plot of stopping power versus range is available from the website but is also approximated by differentiating the polynomial in (5.4). With adjustments along horizontal axes, plots for both the proton and the triton are shown in figure 5.2.

The schematic in figure 5.3 shows the array of (blue) signal wires in the ion chamber interspersed between neighboring sets of (red) high voltage wires. Since the high voltage wires are kept at a large positive voltage, a negative ion produced between any neighboring set of four will be repelled by each one and ultimately be collected by the signal wire at the center. Four neighboring high voltage wires therefore delineate the corners of a 1.9×1.9 cm cell with a horizontal depth approximately equal to the length of the signal wire—about 20 cm. A simple labeling scheme for all 144 cells uses the coordinate pair (S,w) which begins at the bottom left of the diagram with the value (1,1). As an example, the cell (2,5) surrounds the central signal wire in second blue column from the left.

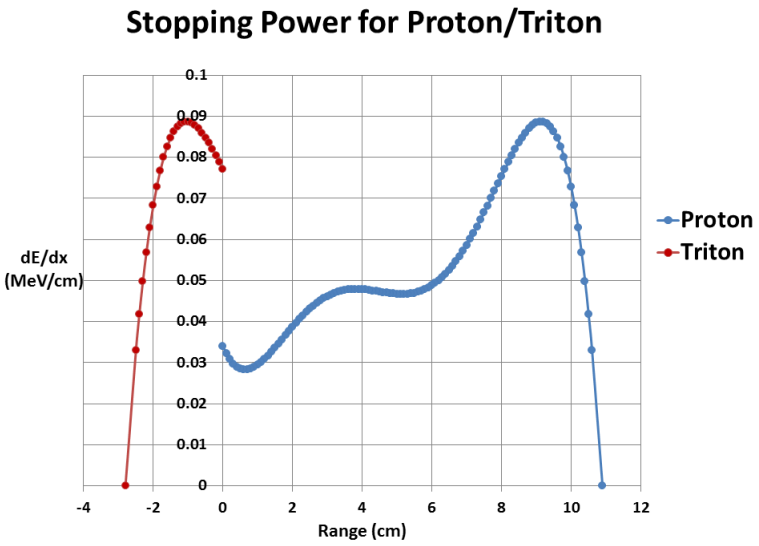

Figure 5.2: Plots of stopping power for the proton and triton moving off in opposite directions.

The collection of ions within the cells from ionization tracks provides a method by which a simulation of ion chamber yield can be constructed. The essential program is to employ a random number generator to simulate events in the ion chamber with a probability decreasing exponentially with distance z from the front of the chamber. Each event is the source of ionization tracks from opppositely directed protons and tritons which otherwise move off in a random direction. The total energy collected in each of the 144 cells can then be calculated by energy deposited from the particle tracks.

5.2 Ion Chamber Profile

5.2.1 Variability of Yield

The first several months of data production at the SNS used a proton beam power of approximately 845 kilowatts while DOE mandates lead to increased power up to 1.4 megawatts during the final months of production. The proportionality between

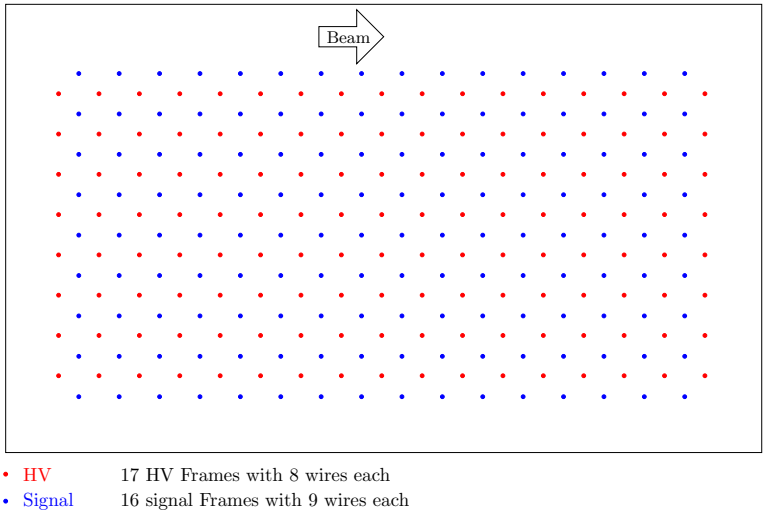

Figure 5.3: Graphic drawing showing wire grid pattern of the frame stack.

the SNS proton beam power and the FnPB neutron beam power implies that yields recorded in the ion chamber also varied over the same relative magnitude.

Even with large yield variations an important statistic is available in the form of a normalized yield defined by

$$N_{S,w}(\lambda) \equiv \frac{\langle I_{S,w}(\lambda)\rangle}{\langle \mathrm{M1}_{max}\rangle} \tag{5.6}$$

The quantity $\langle I_{S,w}(\lambda)\rangle$ is the signal at wavelength λ recorded on wire (S, w) averaged over a single data run (approximately $25,000$ pulses at 60 Hz) while $\langle \mathrm{M1}_{max}\rangle$ is the average maximum signal recorded on the M1 monitor for that data run. The variation of the normalized signal should be quite small and is illustrated in figure 5.4 for wire (1,5) at two separate time bins. These histograms were developed using 300 arbitrarily chosen 'good' data runs in the range 18600 - 38049. Averages and standard deviations are

$$N_{1,5}(\lambda_{12}) = 43.9460 \pm 0.3565 \qquad N_{1,5}(\lambda_{24}) = 55.5538 \pm 0.4709 \tag{5.7}$$

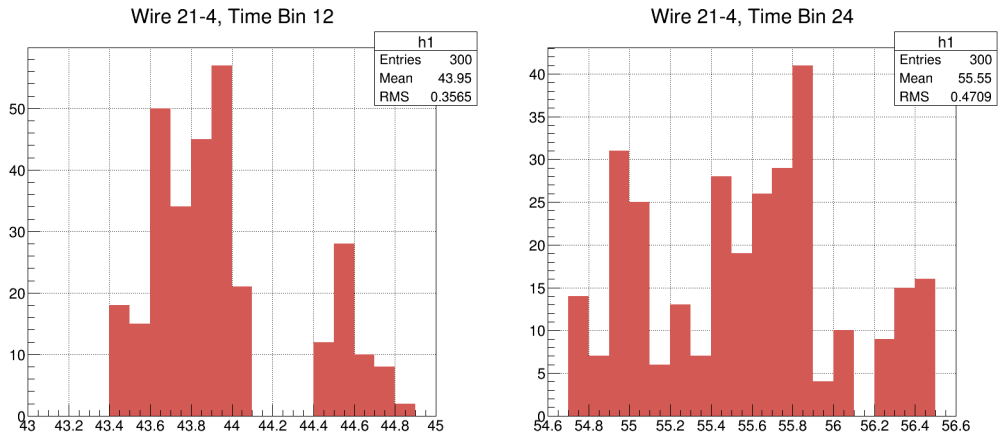

Figure 5.4: Histograms of the nomalized yield on wire (1,5) for two separate time bins using 300 arbitrarily chosen data runs.

This analysis a good indicator that normalized yields for each wire may show variability of less than one-percent for all data production.

5.2.2 Map of Ion Chamber Profile

For any given data run it is possible to develop an ion chamber profile of the average signal recorded on each wire. However, a more complete assessment is a mapping of the average signal recorded on each wire at each of the 49 time bins for which the signal is recorded—equivalent to 7056 data points. Such plots exhibit a sharp exponential decay of the yield with distance from the front of the ion chamber. Significant yield attenuation also occurs for the top two rows of wires and the bottom two rows of wires. Neither of these wire planes is exposed to the direct beam which extends only about 4 cm in either direction from the central wire plane.

A useful and quantitave way to develop a chamber profile is to graph the decay of the yield signal along each of the 9 horizontal wire planes. Figure 5.5 shows plots determined from two separate data runs which have been normalized so that the total yield in all wires adds to 144. The value of the data run numbers indicates that the data was collected at two times separated by several months—strong evidence of the

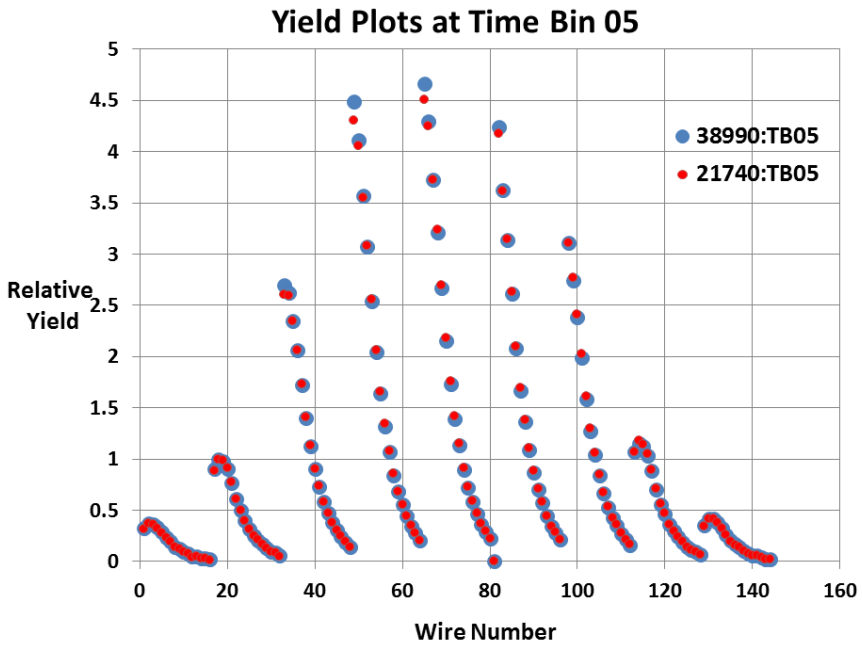

Figure 5.5: Mapping of yields along the nine horizontal wire planes.

repeatability of determining normalized yields. Each decay curve is composed of 16 data points equally spaced along the length of the ion chamber. Of particular interest is the signal maximum between the second and third wires for the top two and bottom two wire planes which may be indicative of the proton range in the ion chamber.

While the first few points near the front face of the ion chamber do not necessarily fall on a pure exponential decay curve, a precise exponential decay of the yield does result for the remaining 12 points and will take the form

$$\mathcal{Y}_w(S) = A_w e^{-\alpha_w S} \tag{5.8}$$

The two parameters A_w and α_w for each horizontal wire plane have been determined from a least-squares fit for three separate time bins all associated with data run 21740 and are summarized in table 5.1.

The correlation coefficients R^2 for each curve generally show a very good exponential fit. From this it can be inferred that the listed values of A_w and α_w are

Table 5.1: Values of A_w and α_w associated with three separate time bins for data run 21740

		TB 01			**TB 20**			**TB 48**	
	A_w	α_w	R^2	A_w	α_w	R^2	A_w	α_w	R^2
$w = 1$	1.057	.2577	.972	1.443	.3080	.984	2.824	.4650	.522
$w = 2$	2.603	.2436	.993	3.454	.2902	.996	5.601	.3912	.971
$w = 3$	5.381	.2315	.999	7.002	.2797	1.00	8.568	.3524	.988
$w = 4$	8.166	.2356	.999	10.68	.2851	.999	15.83	.3873	.998
$w = 5$	8.616	.2350	1.00	11.24	.2837	.999	16.78	.3846	.998
$w = 6$	8.435	.2365	.999	11.04	.2857	.999	16.53	.3891	.993
$w = 7$	6.332	.2331	.999	8.217	.2825	.999	10.20	.3572	.988
$w = 8$	2.878	.2377	.998	3.801	.2843	.998	5.124	.3622	.974
$w = 9$	1.298	.2690	.982	1.787	.3204	.985	4.927	.4896	.879

fundamental constants associated with the decay profile having only small variations between data runs.

The decay constants produced by the data provide important information about the ion chamber. Plots of the decay constants versus wire number for the three listed time bins are shown in figure 5.6 and show considerable increases for the outer wires $w = 1, 2, 8, 9$. The relative size of the increase is also dependent on the time bin chosen but nevertheless universal over all time bins. An immediate problem arises because each time bin is associated with a specific neutron wavelength and the decay rate of the signal should not vary with the y-coordinate. One way to explain this is to assume that a uniform background exists for all wires in the ion chamber. This background will be a larger portion of the signal for the outer wires since they produce smaller yields. Subtracting 0.6% of the total yield evenly spread over the wires slightly modifies the profile and leads to least-squares fits which produce a flat value of α_w over the 9 wire planes.

It is also beneficial to plot a least-squares determination of α_w over all 49 times bins for each wire plane w. The plots show good linearity except for the first few times bins and also the last few time bins. If backgrounds can be subtracted from

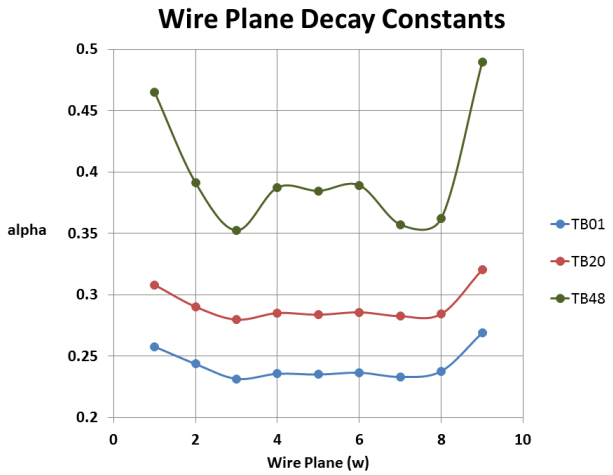

Figure 5.6: Plots of α_w versus wire number w.

intial yields this value will be the same for all wire planes in a given time bin so that a single linear function will suffice to determine $\alpha_w(T)$ for most of the time bins.

Graphs for the decay amplitude A_w versus wire plane can also be constructed from table 5.1 and these have been plotted in figure 5.7. Once again, values of the amplitude grow with with larger time bins, but this not unusual because the normalized yield of each time bin is the same. This requires a larger initial amplitude for a yield that decays more rapidly. Also evident from figure 5.7 is a general trend for larger amplitudes on higher wire numbers compared to their conjugates. This can be attributed to the fact that the top door of the four-jaw collimator is opened by a small extra distance $\Delta y \sim 2$ mm from the central wire plane compared to the lower door.

5.3 Monte Carlo Simulation

A quantitative account of the yield profile in the ion chamber allows for the development of a Monte Carlo simulation capable of matching the amplitudes $A_w(T)$ and decay constants $\alpha_w(T)$ for each of the 49 time bins to within a few percent. The

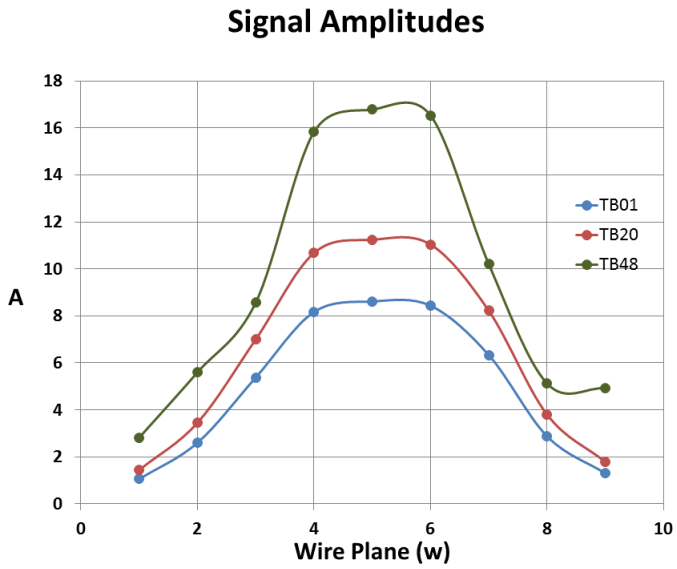

Figure 5.7: Values of A_w for three time bins associated with data run 21740.

essential problem of the simulation is to generate an appropriate distribution of decay events inside the ion chamber fully described by the set of coordinates

$$E1 \rightarrow (x_i,\ y_i,\ z_i,\ \theta_i, \phi_i,\ l_{proton})$$
$$E2 \rightarrow (x_i,\ y_i,\ z_i,\ \pi - \theta_i,\ \pi + \phi_i, l_{triton})$$

The three cartesian coordinates indicate the location of the event decay in the ion chamber, the two angles represent the direction of the decay proton, and the lengths l_{proton} and l_{triton} are ranges of the decay particles determined in equation (5.3). Each set can then be directed into a subprogram to calculate energy deposited to individual cells by the decay.

Simulation of the Neutron Beam: A preliminary requirement to the development of the simulation for the ion chamber, is a simulation of the neutron beam itself. The beam emerging from the neutron guide has cross-sectional dimensions 10 cm wide by 12 cm high having an initial density which is roughly flat. However,

beam spreading occurs in both x- and y- directions leading to variations in the beam density as it moves in the $+z$ direction. This can be described mathematically as a convolution of a 2D step function with a 2D Gaussian distribution characterized by variances σ_x and σ_y which are both functions of the distance **zi** travelled from the end of the guide. Computer code generating N coordinates **xi** and **yi** from the convolution is produced by the FOR statement:

```
[01]     for(i=0; i<N; i++){
[02]         x = 2.0*myran.doub() - 1.0;
[03]         y = 2.0*myran.doub() - 1.0;
[04]         xr = xzp*myran.doub() + xzm;
[05]         yr = yzp*myran.doub() + yzm;
[08]         ww = x*x + y*y;
[09]         ww = sqrt((-2.0*log(ww))/ww);
[10]         xi = sigmax*x*ww + xr;
[11]         yi = sigmay*y*ww + yr;
[12]         }
```

On lines 4 and 5 the variables (**xzp**, **xzm**, **yzp**, **yzm**) determine the width and height of the neutron guide which will prevail if the variances **sigmax** and **sigmay** are chosen to be zero. On the other hand, inserting non-zero values for the variances gives the shape of the beam downstream. Histograms in figure 5.8 are prepared showing the simulated x-distributed shape of the beam at three values of **sigmax**. The values **sigmax** = 1, 6 were chosen to simulate the shape of the beam at the position of the beam scans performed in September and October 2014. The histograms place events into 500 bins having bin sizes 1 mm wide. If n_i is the portion of the N events located in each bin then the coordinate average and the variance can be determined from

$$\bar{\mathbf{x}} = \frac{1}{N}\sum_{i=1}^{500} n_i \mathbf{x}_i \qquad\qquad \sigma_x^2 = \frac{1}{N}\sum_{i=1}^{500} n_i(\mathbf{x}_i - \bar{\mathbf{x}})^2 \tag{5.9}$$

With an initial beam width of $\Delta x = 10$ cm the central maximum at each variance is easily shown to occur near 8.55 cm which is the x-coordinate of the simulated beam centroid relative to the arbirarily chosen coordinate system.

Decay Events in the Ion Chamber: The transformation of a beam simulation to an ion chamber simulation can be accomplished with only minor adjustments to

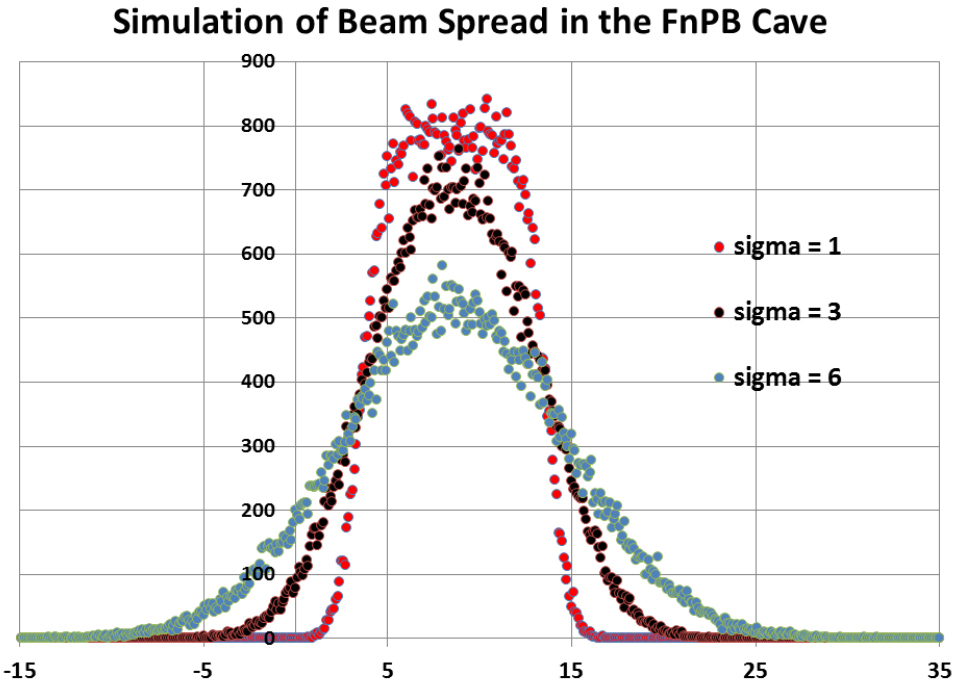

Figure 5.8: Histogram of beam density in x-direction at three values of σ_x.

the program. First, the beam variances σ_x and σ_y must be reset so that the random coordinate **zi** is zero at the entrance to the ion chamber. Computer code determines variances to be

```
[1]         sigmax = 1.2726 + zi*0.0093
[2]         sigmay = 1.7221 + zi*0.0126
```

The slope of these linear functions is simply the angle of beam spread measured in radians along each transverse direction whereas the two constants in front are an estimate of the variance at the front of the ion chamber which can be approximated from extrapolating 2014 beam scans results.

The second adjustment requires a re-shaping of the beam in the interior of the ion chamber. This shape is determined by the four-jaw collimator located just in front of the ion chamber which absorbs the entire beam outside a rectangle determined by the settings on the individual doors. The action of the collimator on the beam can be introduced into the simulation by rejecting random coordinates outside of an

appropriately chosen perimeter. Like the variances σ_x and σ_y, this perimeter must be designed as a slightly increasing function of **zi** to account for beam spreading after the collimator.

A final adjustment is to generate the event coordinate **zi** with a probability that decreases exponentially with the distance from the front of the ion chamber. If **zi** is a flat random variable in the interval $[0, 1]$ then the simple FOR statement

```
[01]      for(i=0; i<N; i++){
[03]         z = myran.doub();
[04]         zi = -log(1-z)/alpha;
[05]         }
```

will create an exponential distribution of N events with a decay constant 'alpha' from the random source.

Distributions of event coordinates produced in the ion chamber for $N = 100,000$ are displayed in figure 5.9. The position **zi** in the chamber is on the vertical axis while values of **xi** and **yi** for each **zi** are shown in red an green, respectively. The perimeter set by the collimator is easily determined by evaluating the **xi** and **yi** limits of the distribution at **zi** $= 0$. The transverse spreading of the beam in both transverse directions is barely visible as the value of **zi** increases.

The number of events (either red or green) in the illustration is actually much less than the orignal value of N. The length of the ion chamber enclosing the volume of ^{3}He is 33.83 cm. A small portion of events generated with **zi** > 33.83 will therefore not be useful. For those **zi** which are useful, further rejections by the program will be necessary to generate the transverse coordinates **xi** and **yi** inside the perimeter. As an example, for $N = 100,000$ and a decay constant **alpha** $= .140$, the exponential decay only uses 99062 values of **zi** form the pseudorandom number generator. When x- and y- coordinates outside the perimeter are rejected, this number drops further leaving only 43583 useable events. These numbers will change if the seed for the random number generator is changed.

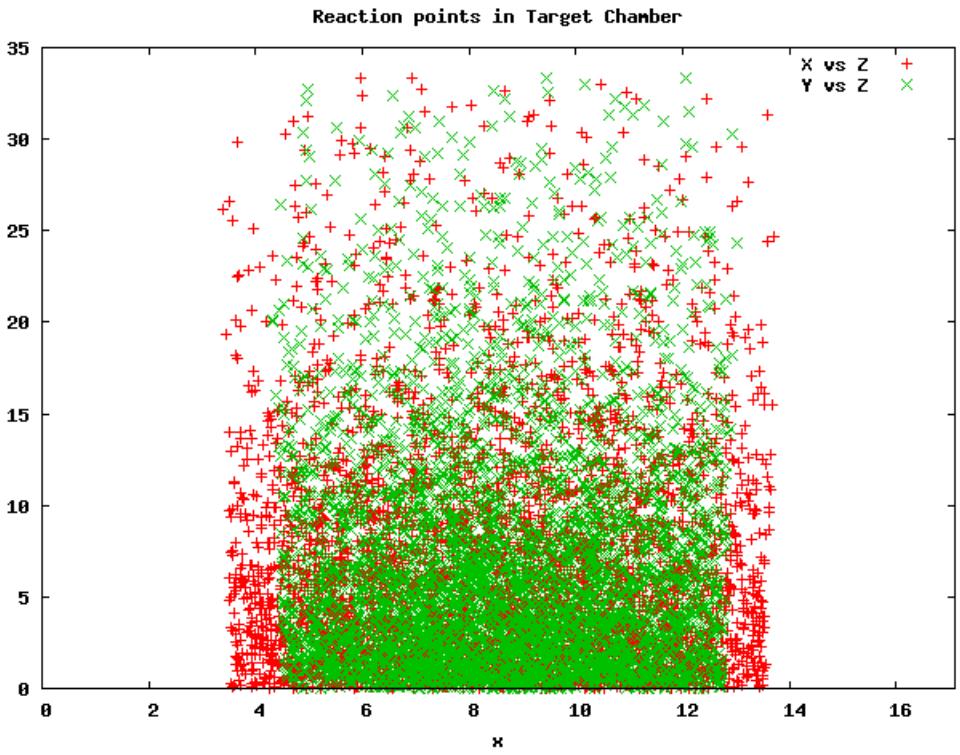

Figure 5.9: Profile of the neutron beam at the front and back of the ion chamber.

Calculation of Simulated Yield: A copy of the required source code for generating simulated ion chamber decay coordinates for the n^{3}He experiment is included in the appendix for reference. The code includes calls to subprograms which use each set of random coordinates to calculate energy deposits made by the proton and triton into the 144 cells. The two subprograms and their function are:

```
grid41 ----->  Energy deposit from proton decay track
grid42 ----->  Energy deposit from triton decay track
```

Each time these programs are called energy from the tracks is added into a 2D array. After a large number of calls, the program outputs the identification (S, w) for each cell along with the total energy deposited to the cell. All programs can be viewed at n3he.wikispaces.com.

5.4 Calculation of g-factors and Correlation Coefficients

The problem of determining the physics asymmetry along with its experimental error is assisted by computer simulations capable of determining accurate values for g-factors g_m and covariance matrix elements C_{ij}. The g-factors cannot be determined from actual experimental data. A computer simulation however can measure energies deposited to individual cells in the wire chamber by reaction proton and triton tracks along with polar angles associated with each track. For a simulation consisting of N trial interactions for a given wavelength, the g-factor for cell m is given by

$$g_m(\lambda) = \frac{\sum_{k=1}^{N} E_{mk}(\lambda) \sin\theta_{mk}}{\sum_{k=1}^{N} E_{mk}(\lambda)} \tag{5.10}$$

An average over all 49 wavelengths recorded by the DAQ is

$$\langle g_m \rangle = \frac{1}{49} \sum_{\lambda} g_m(\lambda) \tag{5.11}$$

The ion chamber for the n^{3}He experiment consists of 16 planes of 9 wires each. Techinically, there are 144 g-factors but g-factors associated with the central wire in each wire plane are approximately zero. For a yield distribution inside the ion chamber symmetric across the central wire plane, g-factors on either side are the same to within a sign, so an accurate simulation should only yield 64 g-factors. On the other hand, the asymmetry of the signal which is known to exist in the ion chamber might be large enough to require a full set of 128.

The purpose of the covariance matrix is to eliminate statistical redundancy caused by the random decay tracks in the ion chamber. Calculation of individual C_{ij} will require computation of a 64×64 matrix for individual sets of decay tracks—one from a spin-up neutron and another from a spin-down neutron. The size of the matrix dictates a large amount of computing power. The energy deposited into cells inside the ion chamber must first be divided according to whether the neutron spins are either up or down. Let

- $E^{+}_{j,k}$: Energy absorbed by the jth cell from the kth interaction involving a spin up neutron.

- $E^{-}_{j,k}$: Energy absorbed by the jth cell from the kth interaction involving a spin down neutron.

With these two definitions the physics asymmetry can be determined for a conjugate wire pair from the equation

$$A_{j,k} = \frac{1}{2}\left[\frac{E^{+}_{j,k} - E^{-}_{j,k}}{E^{+}_{j,k} + E^{-}_{j,k}}\right] - \frac{1}{2}\left[\frac{E^{+}_{j^*,k} - E^{-}_{j^*,k}}{E^{+}_{j^*,k} + E^{-}_{j^*,k}}\right] = \frac{1}{2}\left[Y_{j,k} - Y_{j^*,k}\right] \tag{5.12}$$

Since there are 144 wires in the ion chamber and the quantity $A_{j,k}$ is determined for each pair of wires, this implies a 72×72 covariance matrix having individual elements

$$C_{mn} = \frac{1}{g_m g_n N}\sum_{k=1}^{N}\left(A_{m,k} - \bar{A}_m\right)\left(A_{n,k} - \bar{A}_n\right) \tag{5.13}$$

The covariance matrix can be used to determine an appropriate weight factor for each wire pair. This entails finding the inverse of C_{mn} and writing

$$\mathcal{W}_m = \frac{\sum_n C^{-1}_{mn}}{\sum_{m,n} C_{mn}} \tag{5.14}$$

The final value for the physics asymmetry is then the weighted sum

$$\bar{A}_{_{phys}} = \frac{\sum_m \mathcal{W}_m A_m}{\sum_m \mathcal{W}_m} = \sum_m \mathcal{W}_m A_m \tag{5.15}$$

Chapter 6
Concluding Remarks

Neutron polarimetry measurements were planned and performed on a monthly basis to verify the stability of the neutron beam and the operational status of critical components of the experiment. Beam polarization has been measured to a precision at least as good as expected uncertainties in the measured DDH coupling constants of a few percent. In addition, the spin flipper showed only small deviations from 100% at a level less than about 0.4%.

The capabilities of the spin flipper have met all expectations. The double cosine-theta coil configuration was shown to be a very efficient design having the ability to flip both longitudinal and transversely polarized spins. This was an important factor in the success of the experiment since the initial plan to use longitudinal spin polarizations could not be realized.

The use of 18 AWG aluminum wire to wind the coils was a useful (and necessary) design feature. Although solid copper will achieve a higher conductivity, not only does copper have unfavorable activation properties when exposed to a neutron beam, but the increased tensile strength of the wire introduces difficulties when winding around the sharp corners of the double cosine-theta coil.

Despite the successes of the spin flipper, there exists two possible improvements for future spin flipper desgins of this type which deserve mention. First, it is recommended to construct both the inner cylinder and outer return coils using available 3D print technology. The use of PVC pipe for the n^{3}He spin flipper was un-neccessarily heavy and time consuming to build. Second, the spacing between the

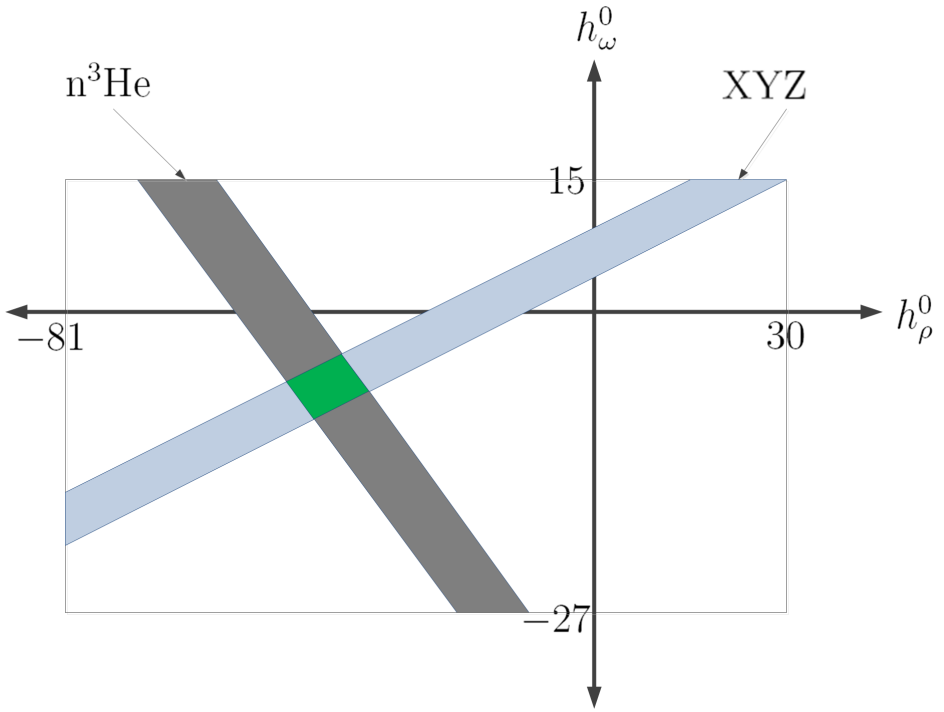

Figure 6.1: Schematic showing ranges of the isospin-0 coupling constants provided by the n^{3}He and 'hypothetical' XYZ experiment. A second experiment narrows the range of both coupling constants to within the green box. The rectangular perimeter indicates the reasonable ranges determined by the DDH model.

ends of the coils and the end-plates of the spin flippers' aluminum shell may have been larger than necessary. Decreasing this separation on both ends of the device would enhance the flow of faraday currents in the end-plates yielding a sharper boundary for the internal RF magnetic field—and therefore improved spin flipper efficiency.

The goal of the n^{3}He experiment is a measurement of the PV proton asymmetry. Equation (1.5) shows that if the values of A_p and h^1_π are known, then a succesful experiment will only extract a linear relationship between the couplings h^0_ρ and h^0_ω. If uncertainties in the value of A_p and h^1_π are also included, this will determine a range of values for h^0_ρ and h^0_ω shown by the grey band in figure 6.1. A reduced range of values is shown by the green box in the figure representing the intersection of the n^{3}He results with a second blue band provided by a another experiment XYZ.

Data analysis is underway for the both the PC and PV proton asymmetries. However, published results will only be available pending the completion of Monte Carlo simulations which can accurately predict g-factors and correlation coefficients necessary for the calculation of the asymmetries.

Bibliography

[1] A measurement of the Parity Violating Proton Asymmetry in the Capture of Polarized Cold Neutrons on ^{3}He. A Proposal submitted to the SNS FNPB PRAC. November 15, 2007. 2

[2] Detector Development for an Experiment to Measure the Parity Violating Proton Asymmetry in the Capture of Polarized Cold Neutrons on ^{3}He. J.D. Bowman, C.B. Crawford, M.T. Gericke et al. March 17, 2008. 2

[3] n^{3}He collaboration. Proposal update for the n^{3}He Experiment. A Measurement of the Parity Violating Proton Asymmetry in the Capture of Polarized Cold Neutrons on ^{3}He 2, 4

[4] Bertrand Desplanques, J.F. Donoghue, B.R. Holstein. Unified Treatment of the parity violating nuclear force. Annals of Physics 124(2):449-495, 1980. 2

[5] Herbert Anderson. Precise Measurement of the Gyromagnetic Ratio of He^3. Physical Review, Volume 76, Number 10, November 15th, 1949. 8

[6] Greene G.L. Ramsey, N.F et al. A New Measurement of the Magnetic Moment of the Neutron. Phys. Lett B, Vol 71B, 21 November, 1977. 8

[7] B.C Murphy. Neutronic Design Calculations on Moderators for the Spallation Neutron Source. Oak Ridge National Laboratory, Log No: 32, July 20, 1999. 10

[8] W. Lu, P.D. Ferguson, E.B. Iverson, F.X. Gallmeier, I. Popova. Moderator poison design and burn-up calculations at the SNS. Journal of Nuclear Materials 377(2008) 268-274. 10

[9] N. Fomin, G.L. Greene, R. Allen, V. Cianciolo, C. Crawford, T. Ito, P.R. Huffman, E.B. Iverson, R. Mahurin, W.M. Snow, Fundamental Neutron Physics Beamline at the Spallation Neutron Source at ORNL, August 4, 2014. 11

[10] R. Chad Gillis. ^{3}He Ionization Chambers as Neutron Beam Monitors for the NPDGamma Experiment. Masters Thesis, department of Physics and

Astronomy, University of Manitoba, Winnipeg, Manitoba, Canada. June 2006. 12

[11] Nuclear Instruments and Methods in Physics Research A 671(2012)137143. The implementation of a supermirror polarizer at the SNS fundamental neutron physics beam line. S. Balascuta. 13

[12] J.J. Sakurai, Modern Quantum Mechanics, Second Edition. Addison—Wesley, Copyright © 2011. 14, 39

[13] Resonant Frequency Neutron Spin Flipper, Double Cosine Theta Coil Winding. Unpublished paper written by Tomy, Graduate student of Chris Crawford. May 10, 2011. 16, 24

[14] n^3He wikispaces website: https://n3he.wikispaces.com 19

[15] Guide Magnetic Field. A presentation prepared by Septiminu Balascuta, Stefan Baessler, Jasmin Schaedler, Seppo Penttila, Ricardo Alacorn. October 16, 2010. 21

[16] Technical report on the mapping of the magnetic field for the NPDGamma experiment at FNPB at the Spallation Neutron Source, Oak Ridge National Laboratory. Jasmin Schaedler, Septiminu Balascuta, Stefan Baessler. Oak Ridge, 08/20/2010, updated February 2011. 21

[17] Installation and Alignment of the N3He Experiment. A Thesis Presented for the Master of Science Degree. Eric Lee Plemons, August 2015, University of Tennessee, Knoxville. 22

[18] P.-N. Seo et al. High-efficiency resonant rf spin rotator with broad phase space acceptance for pulsed polarized cold neutron beams. Physical Review, Special Topics—Accelerators and Beams, 11,084701 (2008) 24

[19] C.B. Hayes, Spin Flipper and Neutron Polarimetry for the n^{3}He Experiment. Comprehensive Exam Write-up, November 13, 2014. 24, 59

[20] F. Bloch, A. Siegert, Magnetic Resonance for non-rotating fields. Phys Rev 57:522-527, 1940. 40

[21] Model SR830 DSP Lock-in Amplifier. Stanford Research Systems, Sunnyvale, CA © 2011, Revision 2.5 45

[22] AWG3000 Series Quick Start User Manual. Copyright © Tektronix, inc. Beaverton, OR 49

[23] Crown D-75A Operation Manual © 2007 by Crown Audio® Inc. Ekhart, Indiana 49

[24] Model SR560 Low Noise Pre-amplifier User Manual. Stanford Research Systems, Sunnyvale, CA © 2011, Revision 2.9 50

[25] Matthew Musgrave, The NPDGamma Experiment and Polarimetry using a ^{3}He Spin Filter. Comprehensive Exam Write-up, July 18, 2011. 54, 57, 59, 76

[26] Matthew Martin Musgrave. Neutron Polarimetry with Polarized ^{3}He for the NPDGamma Experiment. Dissertation Presented for Doctor of Philosophy Degree, University of Tennessee, Knoxville. May 2014. 54, 57, 59, 61, 73, 76, 79

[27] Mostafa Jon Dadras. Polarimetry Studies for the NPDGamma Experiment at the SNS. Masters Thesis, University of Tennessee, Department of Physics and Astronomy. December 2009. 54

[28] T.E. Chupp and M.E. Wagshul. Polarized, high density, gaseous ^{3}He targets. Physical Review C, Volume 36 Number 6, Dec 1987 55

[29] G Greene, A K Thompson, M S Dewey. A method for the accurate determination of the polarization of a neutron beam using a polarized ^{3}He spin filter.

Nuclear Instruments and Methods in Physcis Research, Section A: Accelerators, Spectrometers, Detectors and associated equipment, 356(2-3):177-180, March 1995. 70

[30] TDS3000B Digital Phosphor Oscilloscopes 071-0957-03 User Manual. Copyright © Tektronix, Beaverton, OR

[31] C++ Language Tutorial Copyright © cplusplus.com 2008, Juan Soulié

[32] Thinking in C++, 2nd edition, Volume 2 © 1999, Bruce Eckel, President, MindView Inc.

[33] ROOT User's Guide. http://root.cern.ch/root/doc/RootDoc.html

Appendix

Table A.1: Data summary for blue plot in figure 3.10. Field measurements inside the spin flipper.

Distance(cm)	Voltage(V)
1	0.002
2	0.004
3	0.004
4	0.065
5	0.216
6	0.217
7	0.217
8	0.216
9	0.216
10	0.216
11	0.216
12	0.216
13	0.216
14	0.216
15	0.216

Table A.2: Data summary for red plot in figure 3.10. Field measurements inside the spin flipper.

Distance(cm)	Voltage(V)
1	0.002
2	0.004
3	0.006
4	0.051
5	0.217
6	0.216
7	0.216
8	0.216
9	0.216
10	0.214
11	0.214
12	0.216
13	0.216
14	0.216
15	0.216

Table A.3: Data summary for figure 4.12 showing beam average spin flipper efficiency for individual wavelengths with standard deviation.

Item	λ	$\langle\epsilon_{sf}(\lambda)\rangle$	SD
1	3.47715	0.996419	5.643E-04
2	3.54708	0.996812	5.556E-04
3	3.61702	0.997170	5.700E-04
4	3.68696	0.997242	6.573E-04
5	3.75689	0.997423	5.586E-04
6	3.82683	0.997527	5.420E-04
7	3.89677	0.997591	6.492E-04
8	3.96671	0.997632	5.553E-04
9	4.03664	0.997854	5.714E-04
10	4.10658	0.998065	6.212E-04
11	4.17652	0.998194	5.802E-04
12	4.24645	0.998268	6.544E-04
13	4.31639	0.998321	7.301E-04
14	4.38633	0.998349	7.489E-04
15	4.45627	0.998369	6.785E-04
16	4.5262	0.998381	8.210E-04
17	4.59614	0.998364	8.105E-04
18	4.66608	0.998440	8.597E-04
19	4.73601	0.998415	8.747E-04
20	4.80595	0.998396	9.032E-04
21	4.87589	0.998452	9.187E-04
22	4.94582	0.998497	1.015E-03
23	5.01576	0.998452	1.061E-03
24	5.0857	0.998473	9.803E-04
25	5.15564	0.998427	1.059E-03
26	5.22557	0.998266	1.061E-03
27	5.29551	0.998195	1.022E-03
28	5.36545	0.998122	9.991E-04
29	5.43538	0.998058	1.135E-03
30	5.50532	0.998129	1.124E-03
31	5.57526	0.998019	1.285E-03
32	5.6452	0.997829	1.320E-03
33	5.71513	0.997806	1.395E-03
34	5.78507	0.997691	1.341E-03
35	5.85501	0.997569	1.493E-03
36	5.92494	0.997557	1.491E-03
37	5.99488	0.997102	1.522E-03

Table A.4: Data summary for figure 4.10 showing beam average polarization for individual wavelengths with standard deviation.

Item	λ	$\langle P_n(\lambda) \rangle$	SD
1	3.47715	0.948897	1.556E-03
2	3.54708	0.949412	1.376E-03
3	3.61702	0.949681	1.261E-03
4	3.68696	0.949498	1.154E-03
5	3.75689	0.949271	1.203E-03
6	3.82683	0.949055	1.191E-03
7	3.89677	0.948787	1.368E-03
8	3.96671	0.948341	1.608E-03
9	4.03664	0.947710	1.113E-03
10	4.10658	0.947320	1.129E-03
11	4.17652	0.946733	1.138E-03
12	4.24645	0.945929	1.175E-03
13	4.31639	0.945062	1.277E-03
14	4.38633	0.944121	1.327E-03
15	4.45627	0.943109	1.409E-03
16	4.5262	0.942177	1.414E-03
17	4.59614	0.941172	1.451E-03
18	4.66608	0.940108	1.292E-03
19	4.73601	0.938981	1.376E-03
20	4.80595	0.937790	1.451E-03
21	4.87589	0.936642	1.540E-03
22	4.94582	0.935401	1.599E-03
23	5.01576	0.934078	1.684E-03
24	5.0857	0.932717	1.789E-03
25	5.15564	0.931348	1.896E-03
26	5.22557	0.930008	1.954E-03
27	5.29551	0.928521	2.037E-03
28	5.36545	0.927112	2.202E-03
29	5.43538	0.925580	2.234E-03
30	5.50532	0.924067	2.365E-03
31	5.57526	0.922494	2.475E-03
32	5.6452	0.920868	2.686E-03
33	5.71513	0.919234	2.797E-03
34	5.78507	0.917579	2.974E-03
35	5.85501	0.915804	3.083E-03
36	5.92494	0.913970	3.311E-03
37	5.99488	0.911836	3.585E-03

Table A.5: Data summary indicating average background signal and standard deviation measured by wire (1,5) over individual wavelengths. For comparison all background entries are divided by 1.281×10^7 which is typical of a transmission measurement when neutron spins are parallel to the polarized analyzer cell.

Item	λ	$\langle BG(\lambda) \rangle$	SD
1	3.47715	-8.106E-03	9.816E-04
2	3.54708	-8.121E-03	9.860E-04
3	3.61702	-8.140E-03	9.958E-04
4	3.68696	-8.161E-03	1.005E-03
5	3.75689	-8.170E-03	1.014E-03
6	3.82683	-8.168E-03	1.017E-03
7	3.89677	-8.163E-03	1.018E-03
8	3.96671	-8.142E-03	1.015E-03
9	4.03664	-8.121E-03	1.012E-03
10	4.10658	-8.105E-03	1.005E-03
11	4.17652	-8.091E-03	9.987E-04
12	4.24645	-8.083E-03	9.945E-04
13	4.31639	-8.091E-03	9.909E-04
14	4.38633	-8.109E-03	9.915E-04
15	4.45627	-8.126E-03	9.966E-04
16	4.5262	-8.149E-03	9.990E-04
17	4.59614	-8.166E-03	1.004E-03
18	4.66608	-8.175E-03	1.007E-03
19	4.73601	-8.175E-03	1.011E-03
20	4.80595	-8.162E-03	1.015E-03
21	4.87589	-8.145E-03	1.014E-03
22	4.94582	-8.122E-03	1.013E-03
23	5.01576	-8.099E-03	1.007E-03
24	5.0857	-8.084E-03	1.005E-03
25	5.15564	-8.082E-03	1.003E-03
26	5.22557	-8.092E-03	9.998E-04
27	5.29551	-8.108E-03	9.975E-04
28	5.36545	-8.132E-03	9.969E-04
29	5.43538	-8.158E-03	9.990E-04
30	5.50532	-8.178E-03	9.971E-04
31	5.57526	-8.190E-03	9.980E-04
32	5.6452	-8.195E-03	1.001E-03
33	5.71513	-8.185E-03	9.967E-04
34	5.78507	-8.167E-03	9.968E-04
35	5.85501	-8.139E-03	9.869E-04
36	5.92494	-8.113E-03	9.873E-04
37	5.99488	-8.096E-03	9.819E-04

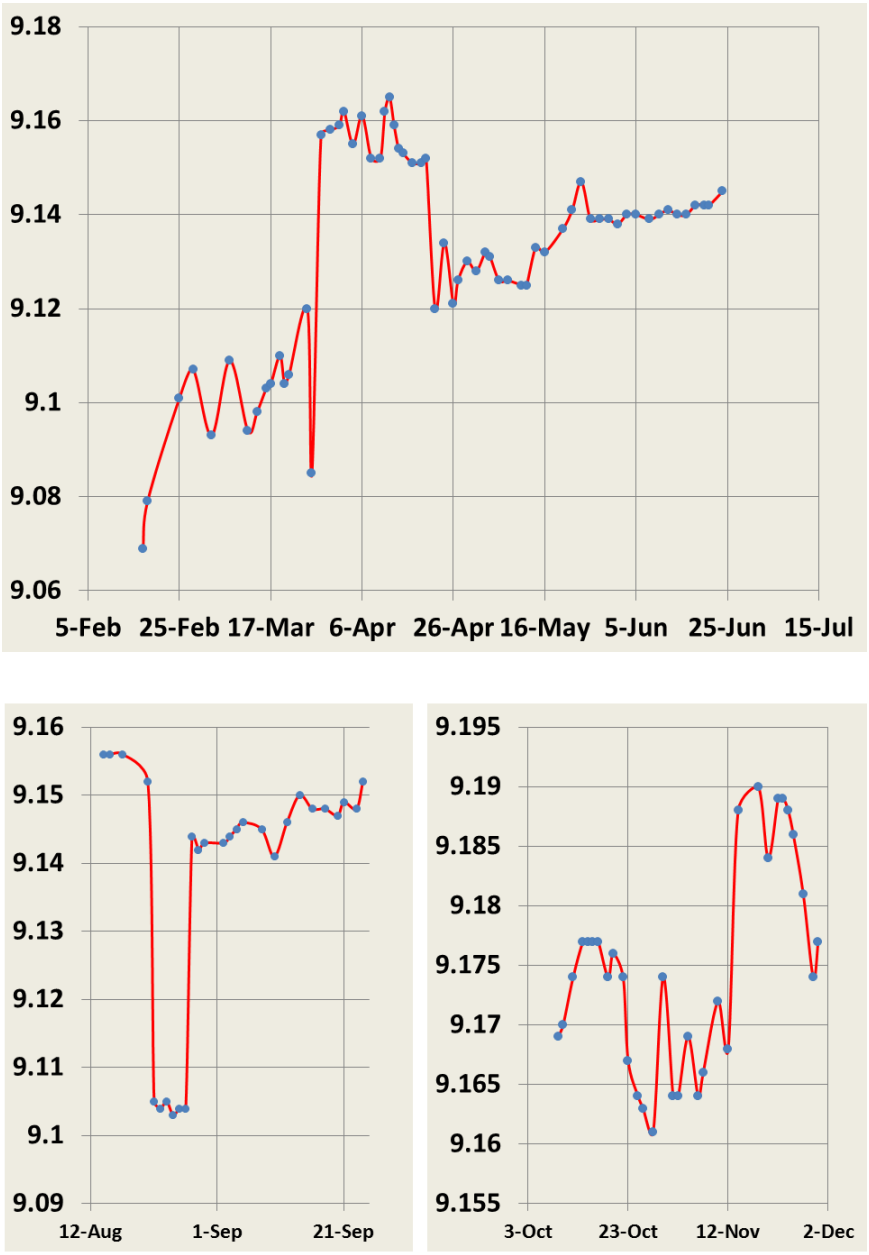

Figure A.1: Plots showing the y-component of the magnetic holding field BY1 read by a magnetometer covering most of 2015. Plots indicate a slight upward trend in the field throughout the course of the experiment in addition to sudden changes of up to 50 mG. Two large breaks in data production are caused by SNS summer shut down (6/24 - 8/14) and failed mercury target (9/24-10/9). Magnetic field data is logged by the DAQ computer every 12 seconds so plots are a made from samples compiled approximately once every 2-3 days.

```
[01] for (k=0; k < intensity; k++)
[02] {
[03]    z = myran.doub();
[04]    zi = -log(1-z)/alpha;
[05]      if(zi < 33.83)
[06] {
[07] theta = pi*myran.doub();
[08] phi = 2*pi*myran.doub();
[09]
[10] sigmax = 1.2726 + zi*0.0093;
[11] sigmay = 1.7221 + zi*0.01257;
[12]
[13] xzm = 3.55*(1 - 0.00262*sp*zi);
[14] xzp = 10*(1+ 0.00186*sp*zi);
[15] yzm = 4.55*(1- 0.00277*sp*zi);
[16] yzp = 8.2*(1 + 0.003073*sp*zi);
[17]
[18] xo = myran.doub();
[19] yo = myran.doub();
[20] xr = xzp*myran.doub() + xzm;
[21] yr = yzp*myran.doub() + yzm;
[22] x = 2.0*xo - 1.0;
[23] y = 2.0*yo - 1.0;
[24] ww = x*x + y*y;
[25] ww = sqrt((-2.0*log(ww))/ww);
[26] xi = sigmax*x*ww + xr;
[27] yi = sigmay*y*ww + yr;
[28]
[29] if(yi >= yzm && yi <= yzp + yzm && xi >= xzm && xi <= xzp + xzm)
[30] {
[31] l= lproton;
[32] grid41(xi, yi, zi, theta, phi, l, lproton);
[33] l= ltriton;
[34] grid42(xi, yi, zi, pi - theta, pi + phi, l, ltriton);
[35] }
[36] }
[37] }
```

Figure A.2: Lines of code generate events in the ion chamber which decay exponentially with coordinate zi along the length of the ion chamber.

Vita

Christopher Bradshaw Hayes was born in Knoxville, Tennessee on January 28th, 1964 to Carla and David Hayes. He lived most of his childhood in Amherst, Massachussetts and received a Bachelor of Arts from UMass, Amherst in 1987. He worked in Indianapolis as an engineer in the field of electrical interconnections for many years but eventually returned to Knoxville to attend the University of Tennessee. There he studied experimental nuclear physics and received his Ph.D. in 2016.